PREPARATION OF GRAPHENE AND GRAPHENE-ANALOGUE TWO-DIMENSIONAL NANOMATERIALS AND THEIR APPLICATIONS IN ELECTRONICS

NIU LIYONG

Ph.D

The Hong Kong Polytechnic University

2016

The Hong Kong Polytechnic University

Institute of Textiles and Clothing

PREPARATION OF GRAPHENE AND GRAPHENE-ANALOGUE TWO-DIMENSIONAL NANOMATERIALS AND THEIR APPLICATIONS IN ELECTRONICS

NIU LIYONG

A Thesis Submitted in Partial Fulfillment of the Requirements for the Degree of Doctor of Philosophy

November 2015

CERTIFICATE OF ORIGINALITY

I hereby declare that this thesis is my own work and that, to the best of my knowledge and belief, it reproduces no material previously published or written, nor material that has been accepted for the award of any other degree or diploma, except where due acknowledgement has been made in the text.

_____*(Signed)*

_____*Liyong NIU*_____*(Name of student)*

ABSTRACT

Two-dimensional (2D) nanomaterials have regained worldwide attention over the past decade since the discovery of graphene in 2004. Tremendous efforts have been devoted to the synthesis and applications of 2D nanomaterials due to their extraordinary and diverse properties in electronics, photonics, catalysis, etc. upon the exfoliation from their bulk counterparts. Regarding the production of 2D nanomaterials, one of the great challenges we have to deal with is how to produce high-quality 2D nanomaterials in a reliable and scale-up way. Although various synthetic strategies have been developed including mechanical exfoliation, chemical vapor deposition (CVD), chemical exfoliation, liquid-phase exfoliation and so on, they all exhibit some sort of disadvantages. Moreover, numerous promising applications, such as energy storage and conversion, electronic devices, catalysis and the like, have been demonstrated due to their diverse properties. Among these applications, we're quite concerned about the photovoltaic (PV) devices, which can convert the solar energy for human beings to use. Currently there are some issues that gradually restrict the rapid development of PV technology. For example, the widely used ITO electrode is becoming a problem due to the scarce reserve, rigid nature and vulnerability to bending test.

In this context, this thesis introduces two approaches to produce 2D nanomaterials and investigate their applications in electronics. One is the liquid-based exfoliation method named salt-assisted direct exfoliation, in which the presence of inorganic salt can facilitate the exfoliation of bulk-layered materials in liquid media. This method can produce high-quality, aqueous-dispersible, single- and few-layered 2D nanomaterials without using any oxidants or long time sonication. The as-produced 2D nanosheets including graphene and TMDs can be easily fabricated into thin films via solution processable manners and be applied into photovoltaic devices either as the transparent electrodes or the buffer layers. Another method is CVD that can produce electronic grade graphene sheets with high carrier mobility, which are applied to field-effect transistors.

Firstly, this thesis details the background and challenges we are confronted with and then puts forward the research objectives and significance. Secondly, a comprehensive literature review is presented including the preparation approaches developed till now to produce 2D nanomaterials, 2D nanomaterials-based composites and their applications in PV aspects. Then the general methodologies involved are introduced. In chapter 4, a salt-assisted direct exfoliation method is first developed and as-produced graphene nanosheets are characterized. Conductive and transparent graphene thin films with various thicknesses are fabricated by vacuum filtration method. Chapter 5 introduces the graphene hybrid thin films with enhanced conductivity by the combination with 1D silver nanowires. This hybrid films based on as-produced graphene nanosheets can be employed as the electrode in perovskite solar cells. Chapter 6 extends the salt-assisted exfoliation method to prepare 2D graphene-analogue transition metal dichalcogenide nanomaterials. Single- and few-layered 2D nanosheets are obtained and can readily disperse in aqueous solutions. And MoS_2 nanosheets are solution processed into thin films and integrated into organic solar cells as a hole transport layer. Chapter 7 develops a CVD method to synthesize high-quality monolayer graphene and investigates the electrical properties of graphene FET devices with functionalization of polymer brushes and subsequent immobilization of biomolecules. Finally, chapter 8 concludes this thesis and provides future perspectives.

LIST OF PUBLICATIONS

Related Journal Publications

1. **Liyong Niu**, Mingjian Li, Xiaoming Tao, Zhuang Xie, Xuechang Zhou, Arun PA Raju, Robert J Young, Zijian Zheng, "Salt-assisted Direct Exfoliation of Graphene into High-quality, Large-size, Few-layer Graphene Sheets", *Nanoscale* 2013, 5, 7202-7208.
2. **Liyong Niu**, Kan Li, Hongyu Zhen, Ying-San Chui, Wenjun Zhang, Feng Yan and Zijian Zheng, "Salt-assisted High-throughput Synthesis of Single- and Few-layer Transition Metal Dichalcogenides and Their Application in Organic Solar Cells", *Small* 2014, 10, 4651-4657.
3. **Liyong Niu**, Jonathan N. Coleman, Hua Zhang, Hyeonsuk Shin, Manish Chhowalla and Zijian Zheng, "Production of Two-dimensional Nanomaterials via Liquid-based Direct Exfoliation", *Small*, 2015, 12, 272-293.
4. Tingting Gao, Sze-Wing Ng, Xuqing Liu, **Liyong Niu**, Zhuang Xie, Ruisheng Guo, Chaojian Chen, Xuechang Zhou, Jun Ma, Wei Jin, Ying-San Chui, Wenjun Zhang, Feng Zhou and Zijian Zheng, "Transferable, Transparent, and Functional Polymer@graphene 2D Objects", *NPG Asian Mater.* 2014, 6, e130.

Other journal publications

1. Kan Li, Hongyu Zhen, **Liyong Niu**, Xu Fang, Yaokang Zhang, Ruisheng Guo, You Yu, Feng Yan, Haifeng Li and Zijian Zheng, "Full-solution Processed Flexible Organic Solar Cells Using Low-cost Printable Copper Electrode" *Adv. Mater.* 2014, 26, 7271-7278.
2. Jinhua Li, **Liyong Niu**, Zijian Zheng and Feng Yan, "Photosensitive Graphene Transistors" *Adv. Mater.* 2014, 26, 5239-5273.
3. Ruisheng Guo, You Yu, Jifang Zeng, Xuqing Liu, Xuechang Zhou, **Liyong Niu**, Tingting Gao, Kan Li, Yong Yang, Feng Zhou and Zijian Zheng, "Biomimicking Topographic Elastomeric Petals (E-Petals) for Omnidirectional Stretchable and Printable Electronics", *Adv. Sci.* 2015, 2.

4. Caizhi Liao, Meng Zhang, **Liyong Niu**, Zijian Zheng and Feng Yan, "Highly selective and sensitive glucose sensors based on organic electrochemical transistors with graphene-modified gate electrodes", *J. Mater. Chem. B* 2013, 1, 3820-3829.
5. Caizhi Liao, Meng Zhang, **Liyong Niu**, Zijian Zheng and Feng Yan, "Organic electrochemical transistors with graphene-modified gate electrodes for highly sensitive and selective dopamine sensors", *J. Mater. Chem. B* 2013, 2, 191-200.

Conference Presentations

1. Liyong Niu, Zijian Zheng, "Salt-assisted Direct Exfoliation of Two-dimensional Materials into High-quality, Few-layer Sheets", ***Graphene 2014***, May 06-09, 2014, Toulouse, France.
2. Liyong Niu, Zijian Zheng, "Production of Few-layer Transition Metal Dichalcogenides and Their Application in Organic Solar Cells", ***International Meeting on Information Display (IMID) 2014***, August 26-29, 2014, Exco, Daegu, South Korea.

ACKNOWLEDGEMENTS

First of all, I would like to express the great gratitude to my chief supervisor, Prof. Zijian Zheng for the guidance throughout my 4-year PhD period. His enthusiasm and kindness, rigorous and honest approach to research, wisdom and rich knowledge of science have left a deep impression on me. I've learned a lot from him, not only the scientific knowledge, but also the writing and communicating skills, the way to work and think independently and effectively.

My special thanks go to Prof. Xiaoming Tao and Prof. Feng Yan, who are my co-supervisors. They have provided enormous convenience and help to support my research project. Their generous guidance and helpful discussion indeed benefits me a lot.

Also, I would like to give my sincere thanks to all the members in Prof. Zheng's group and colleagues from other groups in the Hong Kong Polytechnic University: Dr. Xuechang Zhou, Dr. Zhilu, Liu, Dr. Kan Li, Dr. Zhuang Xie, Dr. Xuqing Liu, Dr. Xiaoling Wei, Dr. Ruisheng Guo, Dr. Tingting Gao, Dr. You Yu, Dr. Hongyu Zhen, Dr. Libin Liu, Dr. Dongrui Wang, Dr. Yu Yang, Dr. Dongdong Chen, Dr. Ruitao Zhou, Dr. Zhike Liu, Dr. Yiyi She, Chaojian Chen, Lina Chen, Yaokang Zhang, Qiyao Huang, Miya Ng, Casey Yan, Peng Li, Xi Lu, Shuaichen Wang.

I'm also very grateful to Prof. Shuit-Tong Lee, Prof. Wenjun Zhang, Dr. Jian-an Huang and Dr. Ying-San Chui at The City University of Hong Kong and Prof. Robert J. Young, Arun P. A. Raju at the University of Manchester for offering Raman measurement and invaluable discussions. I would like to present my hearty thanks to Prof. Hyeon-suk Shin in the department of chemistry and the department of energy engineering, Ulsan National Institute of Science and Technology, who allows me to study in the world-class lab as an exchange student. Thanks the group members for helping me to adapt the Korean life and do me favors in the research: Dr. Jieun Yang, Dr. A-Rang Jang, Gwangwoo Kim, Seong-In Yoon, Dongwoo Kang, Hoonju Lee, and Kyoungyeol Ma.

I also gratefully acknowledge the financial support from The Hong Kong Polytechnic University (Project A-PJ49; A-PK92; A-SA79), GRF of Hong Kong (PolyU 153041/14P; PolyU 5030/12P) and Innovation and Technology Commission of Hong Kong SAR Government (ITP/007/10TP; ITS/380/14; ITP/067/14TP) and the “C. C. Lee Scholarship”.

Finally I would like to express my gratefulness to my family for their endless support and love.

TABLE OF CONTENTS

LIST OF TABLES AND FIGURES

Figure 2.4. Schematic illustration of Liquid-based direct exfoliation of bulk-layered crystals.

Figure 2.5. Concentration of graphene dispersions produced by various solvents plotted versus solvent surface tension. b) Raman spectra of bulk graphite and graphene flakes. c) and d) TEM images of monolayer graphene and folded graphene sheets. Reproduced with permission.

Figure 2.6. Concentration of graphene dispersions obtained by various types of surfactants. Reproduced with permission.

Figure 2.7. a) Schematic illustration of electrochemical exfoliation of graphite in acid solution. b) Photos of graphite flakes before and after exfoliation. c) Exfoliated graphene floated on top of water. d) Dispersed graphene sheets in DMF. e) Proposed mechanism for electrochemical exfoliation.

Figure 2.8. Schematic of electrochemical lithiation process for the production of 2D nanosheets from bulk-layered crystals.

Figure 2.9. a) Set-up of high shear mixer in graphene dispersion with close-up view of rotor and stator. b) Diagram of rotor speed, N versus diameter, D. The red line represents a minimum shear rate $\gamma \approx 10^4\ s^{-1}$. c) Concentration of 2D nanosheets dispersed in NMP following the certain scaling behavior.

Figure 2.10. Schemes of as-fabricated OSCs with transparent graphene electrodes prepared by multiple CVD graphene transfer a) and rGO b). c) A semitransparent perovskite solar cell and the corresponding PCEs as a function of transmittance.

Figure 2.11. a) Scheme of as-fabricated OSCs with GO as HTLs and corresponding J-V curves. b) Scheme and energy band diagram of as-fabricated OSCs with rGO as ETL. c) Scheme of as-fabricated inverted-OSCs with MoS_2 as HTL.

single layer b), bilayer c), and trilayer d) graphene sheets, the scale bars are 5 nm.

Figure 4.3. a) XPS survey, b) XPS narrow scan, and c) TGA analysis of graphene sheets, heated from room temperature to 1000 ^{o}C at 5 ^{o}C/min under nitrogen flow. d) Raman spectra of graphite and representative flakes of the as-made graphene from NaCl-assisted exfoliation of graphite in EtOH, e) XRD spectra of as-made graphene and graphite.

Figure 4.4. AFM topographic images of a) graphene sheets and b) a typical graphene sheet of ~3.5 nm thick with edge size ca. 30 μm, scale bars: 10 μm, c) size distribution and d) thickness distribution of as-made graphene sheets. e) SEM image of pristine graphite. f) AFM image of graphene sheet after annealing at 500 ^{o}C in argon atmosphere for 1 h, scale bar 2 μm.

Figure 4.5. a) UV-Vis spectra and b) digital image of the graphene aqueous solution prepared from $CuCl_2$-assisted direct exfoliation of graphite in various organic solvents. c) AFM topographic image of graphene, scale bar: 10 μm. d) Cross-sectional profile analysis of the marked red line in c). e) TEM image of graphene sheets. Inset is the electron diffraction pattern. (f-h) HRTEM images of f) single-layer, g) bi-layer and h) multi-layer graphene. The scale bars are 5 nm.

Figure 4.6. a) Optical micrographs, b) AFM topographic images, and c) cross-sectional profiles of the as-made graphene prepared by $CuCl_2$-assisted direct exfoliation of graphite in ethanol after annealing at 500 ^{o}C in argon atmosphere for 1 h. The scale bars are 20 μm and 5 μm for a) and b), respectively.

Figure 4.7. a) Concentrations of as-produced graphene aqueous solution dependent on various boiling time. b) AFM image of graphene sheets prepared w/o salts, scale bar: 2 μm. c) The corresponding image of graphene solution in a) prepared by NaCl (left) or $CuCl_2$ (right) assisted exfoliation of graphite in NMP.

Figure 4.8. a) Proposed exfoliation process upon boiling and water evaporation. b) TEM images of the intermediate mixture using $CuCl_2$. c) HR-TEM image of

the intermediate mixture. d) EDX spectrum corresponding to the black particles in b). e) XRD spectra of intermediate product by using $CuCl_2$ after boiling for different time.

Figure 4.9. a) UV-vis transmittance of graphene thin films of various thicknesses. b) Transmittance of graphene films plotted as a function of sheet resistance, inset: digital image of the graphene thin film with 45 nm thickness on the glass substrate. c) The thickness of graphene films versus their roughness. The graphene was prepared by salt-assisted exfoliation method using NaCl and EtOH. d) AFM topographic image of the 45 nm thick graphene film, roughness (R_q)=30 nm. e) AFM topography image of the scratched edge of the 45 nm graphene film. f) The height profile of the marked line in e). The scale bars are 10 μm.

Figure 5.1. Scheme illustration of graphene/Ag NW hybrid films.

Figure 5.2. a) SEM image of Ag NWs. b) AFM image of Ag NWs. c) SEM image of graphene thin films. d) SEM image of G/Ag NW hybrid thin films.

Figure 5.3. The optical transmittance spectra of Ag NW films a) and G/Ag NW hybrid thin films b). c) The sheet resistance of various thin films. d) The bending test of G1/Ag NW film on PET substrate.

Figure 5.4. a) The schematic structure of perovskite solar cells. b) AFM image of TiO_2. c) SEM image of perovskite layer. d) AFM image of perovskite layer. e) XRD spectrum of perovskite layer. f) J-V curves of as-fabricated perovskite solar cells.

Figure 6.1. UV-vis spectra (a, c, e, and g) and digital images (b, d, f, and h) of aqueous solutions of TMD 2D materials prepared by NaCl-assisted exfoliation in various organic solvents.

Figure 6.2. UV-vis spectra (a, c, e, and g) and digital images (b, d, f and h) of aqueous solutions of TMD 2D materials prepared by $CuCl_2$-assisted exfoliation in various organic solvents.

Figure 6.3. Time dependence (boiling time) measurement of the yields of 2D TMDs synthesized with and without (w/o) inorganic salts.

Figure 6.4. XRD spectra of bulk TMDs and their corresponding exfoliated 2D sheets prepared by salt-assisted liquid exfoliation using NaCl and $CuCl_2$.

Figure 6.5. Raman spectra of bulk TMDs and their corresponding exfoliated 2D sheets prepared by NaCl-assisted exfoliation in NMP using 514 nm excitation laser, a) MoS_2, b) $MoSe_2$, c) WS_2 and d) WSe_2.

Figure 6.6. Typical AFM topographic images of exfoliated TMD 2D sheets: a) MoS_2, b) $MoSe_2$, c) WS_2 and d) WSe_2 and their corresponding thickness distributions, scale bars: 2 μm.

Figure 6.7. TEM images of few-layered TMDs sheets prepared by NaCl-assisted exfoliation: a) MoS_2, b) $MoSe_2$, c) WS_2, and d) WSe_2. Insets are the SAED patterns. b), d), f) and h) are the corresponding HRTEM images.

Figure 6.8. TEM images of few-layered TMD 2D sheets prepared by $CuCl_2$-assisted exfoliation: a) MoS_2, b) $MoSe_2$, c) WS_2, and d) WSe_2. Insets are the SAED patterns. b), d), f) and h) are their corresponding HRTEM images.

Figure 6.9. EDX analysis (in TEM) of as-produced TMD 2D sheets. Spectra and analysis shown from top to bottom are for MoS_2, $MoSe_2$, WS_2, WSe_2, respectively.

Figure 6.10. a) Structure of OSCs using HTL made of few-layer MoS_2 2D sheets. b) J-V curves of as-made OSCs under solar simulator. MoS_2 HTLs were prepared by film transfer and drop casting methods. c) Typical J-V characteristics of OSCs with MoS_2 HTL prepared by drop casting and

PEDOT:PSS under illumination and dark condition. d) The transmittance of different HTLs on ITO glasses.

Figure 6.11. The J-V curve of OSCs fabricated by single time drop casting.

Figure 6.12. AFM topographic images of MoS_2 thin films prepared by a, c) film transfer, and b, d) drop casting of few-layer MoS_2 2D sheets. Scale bars: 5 μm.

Figure 7.1. Schematic illustration of polymer brushes functionalized graphene FET.

Figure 7.2. a) Optical image of patterned graphene with channel length ~9.2 μm and channel width ~3.8 μm. B) AFM image of monolayer graphene with a thickness of 0.82 nm c). d) Raman spectrum of graphene sheet. E) Transfer characteristic of graphene FET under 0.01 V bias voltage V_{ds}. F) Output characteristics with various gate voltages from 20 V to -20 V.

Figure 7.3. The height histogram of various graphene films including pristine graphene (G), initiator@G (i@G) and polymer brushes@G characterized by AFM.

Figure 7.4. ATR-FITR spectra of three types of polymer brushes@G with various growth time: a) PMMA@G, b) PGMA@G, c) POEGMA@G. d) Inset is the enlarged spectra of graphene and initiator@G.

Figure 7.5. UV-Vis spectra of polymer brushes functionalized graphene, in which polymer brushes are grown for different time.

Figure 7.6. a) Transfer characteristics of patterned graphene (pG) FET under the bias of V_{ds} (0.05 V). b) The corresponding transfer characteristics of polymer brushes functionalized graphene FET: PMMA@pG, PGMA@pG and POEGMA@pG. c) The corresponding AFM topographic images of polymer brushes@pG with a thickness of 26nm, 19.1 nm and 17.0 nm for PMMA@pG, PGMA@pG and POEGMA@pG, respectively.

Figure 7.7. a) Transfer characteristics of FET devices based on graphene (G, without pattern) and polymer brushes@G under the bias of V_{ds} (0.01V). b) Raman spectra of graphene and polymer brushes@G. Insets are the Raman spectra with magnified G peaks. c) The corresponding AFM topographic images of polymer brushes@G.

Figure 7.8. a) Illustration of molecular reaction for DNA binding and hybridization. b) Immobilization of DNA molecules on PGMA@G FET device. c) The transfer characteristics of polymer functionalized graphene FET and biomolecules-immobilized graphene FET.

LIST OF ABBREVIATIONS

2D Two-dimensional

ACN Acetonitrile

AFM Atomic Force Microscope

BN Boron Nitride

CNTs Carbon Nanotubes

CTAB Cetyltrimethylammonium

CVD Chemical Vapor Deposition

DMF N,N-dimethylformamide

EDX Energy-dispersive X-ray Spectroscopy

ETL Electron Transport Layers

FET Field Effect Transistors

FF Fill Factor

FTIR Fourier Transform infrared Spectroscopy

FTO Fluorine-doped Tin Oxide

GO Graphene Oxide

GQDs Graphene Quantum Dots

HOMO Highest Occupied Molecular Orbit

HOPG Highly Oriented Pyrolytic Graphite

HTL Hole Transport Layers

ILs Ionic Liquids

ITO Indium Tin Oxide

J_{sc} Short Circuit Current

LB Langmuir-Blodgett

LBE Liquid-based Direct Exfoliation

LBL Layer-by-layer

Li-TFSI Li-bis(trifluoro-methanesulfonyl)imide

LUMO Lowest Unoccupied Molecular Orbit

MOF Metal-organic Frameworks

NMP N-methyl-2-pyrrolidone

NPs Nanoparticles

NWs Nanowires

ODCB Ortho-dichlorobenzene

OPV Organic Photovoltaic

OSCs Organic Solar Cells

P3HT Poly(3-hexylthiophene)

PAH Polycyclic Aromatic Hydrocarbons

PCA Pyrenecarboxylic Acid

PCBM [6,6]-Phenyl-C61-Butyric Acid Methyl Ester

PCE Power Conversion Efficiency

PDI Perylenedicarboximide

PBASE Pyrene Butanoic Acid Succidymidyl Ester

PEDOT:PSS Poly(3,4-ethylenedioxythiophene):Poly(styrene sulfonate)

PEG Poly(ethylene glycol)

PI Polyimide

PMMA Poly(methyl methacrylate)

rGO reduced Graphene Oxide

SC Sodium Cholate

SEM Scanning Electron Microscopy

SDBS Sodium dodecylbenzene

SDC Sodium Deoxycholate

tBP 4-tert-butylpyridine

TBT Tetrabutyl titanate

TCNQ Tetracyanoquinodimethane

TEM Transmission Electron Microscopy

TGA Thermo-gravimetric Analysis

TMDs Transition Metal Dichalcogenides

V_{oc} Open Circuit Voltage

XPS X-ray Photoelectron Spectroscopy

CHAPTER 1 INTRODUCTION

1.1 Background and Challenge

The past decade has witnessed the rise of graphene since its mechanical exfoliation from graphite in 2004[1]. Graphene is single-atom thick with carbon atoms hexagonally arranged into a honeycomb lattice and regarded as the basic building blocks for graphitic materials of all other dimensionalities. It can be wrapped up into 0D fullerenes, rolled into 1D nanotubes or stacked into 3D graphite.[2] The worldwide attention from both the academia and industry has been paid to such a unique two-dimensional (2D) nanomaterial. In the light of its extraordinary properties such as high mechanical strength, large specific surface area, high electrical and thermal conductivity as well as high optical transparency, a huge of applications have been demonstrated from the electronic devices, biosensors, robust composites or textiles, to catalysis, photonics, energy storage and conversion, to name but a few. Graphene's emergence has ignited researchers' enthusiasm to explore other ultrathin 2D graphene-analogue nanomaterials. To date, plenty of such 2D nanomaterials have been reported which can be categorized into several groups as follows.[3] One group is the hexagonally featured boron nitride (h-BN) nanosheets and graphene; another is transition metal dichalcogenides (TMDs) and metal halides, e.g. MoS_2, WS_2 and PbI_2;[4] the third group is layered metal oxides (e.g. MnO_2 and MoO_3) and layered double hydroxides such as $Mg_6Al_2(OH)_{16}$;[5] moreover, an emerging, large family of 2D early transition metal carbides or carbonitrides, labled as MXenes is discovered.[6] Because of their unique structural features and diverse physical and chemical properties, endless efforts are being devoted to exploring more applications.

To fulfill such applications, one crucial challenging issue stands in front of us: how to produce these 2D nanomaterials with high quality and large quantity in a commercially viable way? This is actually of paramount importance for the industry to decide if they will ultimately use these new materials for large-scale applications. Up till now, quite a few different methods have been developed for

the production of layered 2D nanomaterials, including bottom-up synthesis by chemical vapor deposition (CVD) and epitaxial growth, and top-down exfoliation approaches by micromechanical cleavage, chemical exfoliation and liquid-based ultrasonic exfoliation. Bottom-up CVD synthesis is regarded as an important way to synthesize 2D nanomaterials, in which the precursors react on the transition metal substrates at high temperature to form single- or few-layered 2D nanosheets. This method can produce graphene and some other TMDs with high quality; however, it requires harsh growth conditions such as high temperature and high vacuum, and is size-limited. Top-down micromechanical cleavage can only produce samples for fundamental study because of its extremely low throughput. Chemical exfoliation, which particularly refers to the synthesis of graphene oxide (GO) via chemical oxidation of graphite to form graphite oxide and subsequent thermal or chemical reduction into reduced graphene oxide (rGO), is low-cost, highly scalable and solution-processable. Nevertheless, the oxygen-containing defects of rGO cannot be fully eliminated, which significantly limits the applications in electronic and optical devices. Although liquid-phase exfoliation shows advantages in making versatile 2D nanomaterials, however long time sonication and low yield become its bottleneck. More methods beyond the aforementioned are developed, showing various advantages and disadvantages.

To address those challenges in the preparation of 2D nanomaterials, this study will develop a modified liquid-phase exfoliation method, namely “salt-assisted liquid-phase exfoliation method”, which can produce single- and few-layered graphene and graphene-analogue TMD 2D nanosheets. The presence of inorganic salts can effectively improve the efficiency and yield of ultrasonic exfoliation. Moreover, it is environmental-friendly in the sense that no hazardous and oxidative chemical are employed in the synthesis process. Meanwhile it is high quality with little defects deriving from the edges instead of the basal plane. Importantly, it is convenient to form composites or hybrids by simply mixing the dispersion of desirable materials as well as low-cost and compatible with solution-processed manners.

With 2D nanomaterials in hand, another concerned issue is the application. Among those applications, the one we are fascinated is the electronic aspect especially a photovoltaic device, which can harvest energy directly from sunlight. The fast-growing demand for energy and recognition of mad-made global climate change underscore the urgency of developing clean and renewable energy resources to replace the fossil fuels. Photovoltaic technology provides a viable way to deal with the energy crisis. Organic photovoltaic (OPV) devices and newly emerged perovskite solar cells offer processing advantages that enable the low-cost, solution-processable, large-area production as well as the light weight and compatibility with flexible substrates. In the fabrication of solar cell devices, one important component is the transparent electrode through which the light is coupled into. Conventionally, indium tin oxide (ITO) is widely used, however, its increasing price, scarcity of reserves and brittle nature severely hampered the applications. Therefore, many researchers have been focusing on the exploring promising candidates with low cost, high transparency and good flexibility. Graphene seems to meet such requirements as the alternative electrode materials to ITO. Another important application is biosensing. Polymer brushes functionalized graphene can provide functional sites to immobilize biomolecules.

In addition, not limited to use as the electrode, graphene can also play an important role in other components of solar cells, such as the buffer layer, and the acceptor. Beyond graphene, the semiconductor property of 2D graphene-analogue TMD nanomaterials is worthy of studying in the photovoltaic devices.

1.2 Research Objectives

This study is focused on the synthesis and application of 2D nanomaterials including graphene and TMD nanosheets. The applications mainly contain, but not limited to, the photovoltaic devices. The detailed research objectives are as follows:

1. To prepare solution-processable graphene nanosheets through the salt-assisted exfoliation of graphite.
2. To fabricate photovoltaic devices by using as-prepared graphene thin films as the electrode

3. To prepare and characterize TMD 2D nanosheets using our established salt-assisted exfoliation method.
4. To study the performance of organic solar cells (OSCs) by integrating TMD 2D nanosheets into the device.
5. To investigate the electrical performance of polymer brushes functionalized graphene.

1.3 Research Significance and Values

A universal consensus has been arrived at that graphene will be one of the most promising candidates for the next-generation electronic material and a competitive alternative to substitute ITO. The successful synthesis of solution processable graphene, the study of its properties and exploration in photovoltaic devices will have significant impact in the electronic and optoelectronic fields. Beyond graphene, TMD nanosheets represent a special class in the ultrathin 2D nanomaterials,[7] exhibiting fascinating and diverse properties. The facile and reliable synthesis of such materials is of equal importance to graphene for the exploration of their properties and applications. Scientifically, the research will lead to new knowledge and perspectives in the synthesis and fabrication of 2D nanomaterials, thin films and various devices.

1.4 Outline of the Thesis

The report is organized as follows:

Chapter 1 introduces the research background, the status quo of 2D nanomaterial synthesis, current challenges and the importance in photovoltaic applications. Further it states the research objectives as well as the significance and values of this research.

Chapter 2 first presents the properties of graphene and TMD 2D nanosheets, and then gives a comprehensive literature review in terms of the various synthetic methods developed and the applications of 2D nanomaterials in photovoltaic devices.

Chapter 3 details the research methodology including the material fabrication and characterization techniques, and the device fabrication and measurement.

In chapter 4, salt-assisted direct exfoliation method is first demonstrated to prepare graphene nanosheets. Graphene thin films are fabricated by solution-processable manners.

In chapter 5, hybrid thin films based on as-produced graphene nanosheets and 1D silver nanowires are integrated into perovskite solar cells as the transparent electrodes.

In chapter 6, TMD 2D nanomaterials are prepared by salt-assisted exfoliation method and the application in OSCs is demonstrated.

In chapter 7, the electrical performance of monolayer CVD graphene functionalized with polymer brushes is investigated. And the immobilization of biomolecules is demonstrated.

Chapter 8 summarizes the conclusions and puts forward some future perspectives.

CHAPTER 2 LITERATURE REVIEW

In this chapter, a comprehensive literature review is presented, which focuses on various aspects including the properties of 2D nanomaterials, e.g. graphene and TMDs, the synthetic methods developed to date, 2D nanomaterials-based composites and some applications in photovoltaic devices.

2.1 Properties of Graphene and 2D TMDs

Upon the exfoliation from their bulk counterparts, 2D nanomaterials can acquire quite unique and execellent peroperties. Take the most studied 2D nanomaterial, graphene, for example. It possesses high intrinsic mobility (2×10^5 cm^2 V^{-1} s^{-1}), large theoretical surface area (2630 m^2 g^{-1}), high thermal conductivity (~5000 W m^{-1} K^{-1})[8] and Young's modulus (~1.0 TPa),[9] excellent optical transmittance (97.7%)[10] and good electrical conductivity (Figure 2.1).[11-14] Such unique and outstanding properties of graphene have been demonstrated to be important for a wide range of applications. It has been used in flexible electronics, such as touch screen displays, electronic papers and organic light emitting diodes, which requires low sheet resistance and high transmittance. The excellent mechanical stability and chemical durability make it superior to rigid and expensive indium tin oxide (ITO). Furthermore, it could be fabricated into field effect transistors (FET) with logic functions[15] or high frequency[16] by opening the bandgap of graphene via nanostructuring[17, 18] or chemical functionalization[19]. In photonics, graphene is applicable for photodetectors[20] and optical modulator[21] due to its wide spectral range from ultraviolet to infrared and ultrafast response. In addition, graphene has become a promising candidate in the search for new materials to build highly efficient and renewable energy generation and storage devices, such as lithium-ion (Li-ion) batteries, OSCs, dye-sensitized solar cells, supercapacitors and etc.

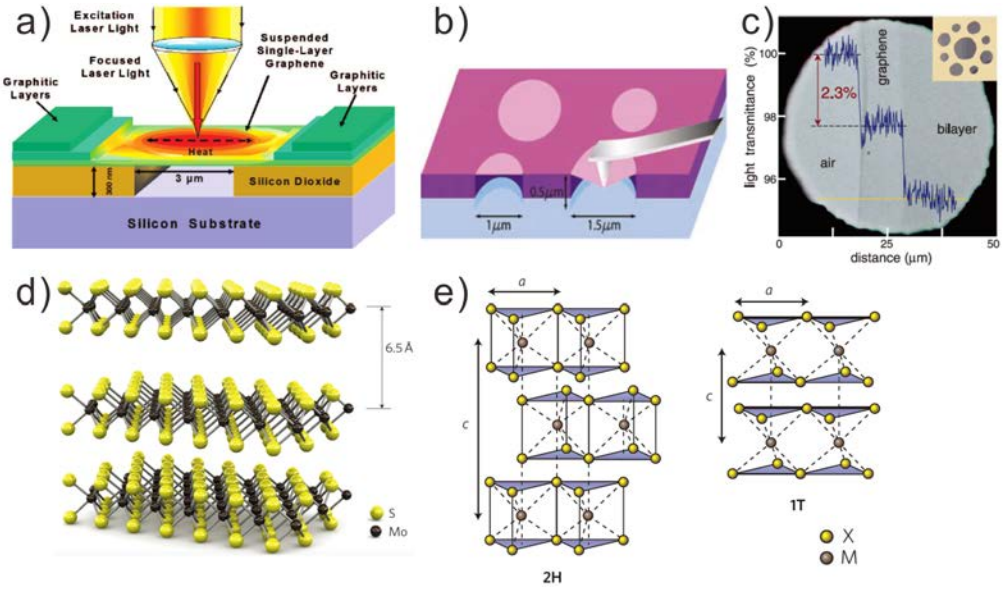

Figure 2.1. a) Schematics of the excitation laser light focused on a suspended graphene layer.[8] b) Nanoindentation on suspended graphene membrane.[9] c) Photograph of a 50-μm aperture partially covered by graphene and its bilayer.[10] d) 3D representation of the structure of MoS_2, single layer ~6.5 Å thick.[22] e) Schematics of the structural polytpyes: 2H and 1T phases.[23]

The applications intensively studied for graphene are more than the aforementioned, and 2D nanomaterials beyond graphene with excellent performances are coming into the light. This is true of TMDs. They are a class of materials over 40 compounds with the common formula MX_2, where M stands for an transition metal element from group IV to X (e.g. Ti, V, Mo and so on), X is a chalcogen (e.g. S, Se or Te). Table 2.1 summarizes the representative layered TMDs with various electronic characteristics. In each layer that consists of X-M-X form, the in-plane atoms are strongly bonded in a covalent way, however, the adjacent layers are weakly held together by van der Waals force, which allows the exfoliation of bulk crystals into single- and few-layer 2D nanomaterials. Upon the exfoliation, TMDs shows layer-dependent properties, especially in several semconducting materials (such as MoX_2 and WX_2) where a transition occurs from indirect bandgap in the bulk to direct bandgap in the monolayer. Also note that monolayer TMDs exhibit only two polymorphs: trigonal prismatic (hexagonal symmetry) and octahedral phases (tetragonal symmetry). Figure 2.1d and e shows 3D structure and the 2H and 1T phase of MoS_2 and the digits indicates the number of layers per repeat unit. Based on the direct bandgap, 2D

TMDs can find a host of applications in elelctronics (e.g. digital transistors), optoelectronics (e.g. photovoltaics and photodetection) and sensing.

Table 2.1. Electronic characteristics of various layered TMDs.[24, 25]

Group	M	X	Properties
4	Ti, Hf, Zr	S, Se, Te	Semiconducting (E_g = 0.2~2eV), diamagnetic.
5	V, Nb, Ta	S, Se, Te	Narrow band metals (ρ ~10^{-4} Ω.cm) or semimetals, superconducting.
6	Mo, W	S, Se, Te	Sulfides and selenides are Semiconducting (E_g ~1eV), Tellurides are semimetallic (ρ ~10^{-3} Ω.cm).
7	Tc, Re	S, Se, Te	Small-gap semiconductors.
10	Pd, Pt	S, Se, Te	Sulfides and selenides are semiconducting (E_g = 0.4eV) and diamagnetic, Tellurides are semimetallic and paramagnetic

2.2 Synthesis of 2D Nanomaterials

In light of the attractive properties of graphene and 2D TMDs in mechanics, optics, physics and electronics, it is doomed to trigger a new research upsurge. And it has been proved so by the fact that intense interest and many efforts have been devoted to the fundamentally theoretical and experimental studies. Even though great breakthrough and progress have been made, the widespread implementation of graphene and 2D TMDs in semiconductor industry and other fields has yet to occur. This is primarily due to the difficulties to reliably produce high-quality 2D nanomaterials, particularly in large scale. Accordingly, among those research interests in 2D nanomaterials, one key issue is to explore effective ways to produce high-quality, large-scale 2D nanosheets. Up till now, quite a few methods have been developed for the production of single- and few-layer 2D nanomaterials, which can be categorized into two types: bottom-up synthesis by chemical vapor deposition (CVD) and epitaxial growth and top-down exfoliation approaches including mechanical exfoliation, chemical exfoliation and liquid-based direct exfoliation.

2.2.1 Epitaxial Growth of Graphene

Among bottom-up approaches, epitaxial growth of graphene via the sublimation of silicon from the surface of silicon carbide is a method to obtain relatively high-quality graphene. This thermal deposition process usually requires high temperature (>1000 ^{o}C) as well as ultrahigh vacuum conditions, both of which are key to the formation of monolayer and few-layered graphene on SiC surface.[26, 27] After the sublimation of Si and subsequent graphitization of the excess carbon left behind, graphene can form nearly perfect structure on both silicon-rich face (0001) and carbon-rich face of the hexagonal phase SiC (4H-SiC or 6H-SiC). More recently, graphene growth on cubic phase silicon carbide has been demonstrated.[28] Graphene grows in a single orientation on a Si-rich face, exhibiting a regular Bernal stacking and rather poor uniformity due to the surface pits. On the contrary, graphene shows rotational stacking and higher conductivity on a C-rich face.

The advantage of this method lies in that high quality graphene can be directly synthesized on the insulating substrate, which is suitable for the wafer-based applications. For example, various kinds of electronic components or devices can be constructed atop without involving the transfer process. However, this method also has its limitation. Unlike metal used in CVD method that will be introduced below, SiC is hard to be removed, which renders the transfer process to other substrate difficult to be accomplished, although some attempts for the transfer of epitaxial graphene onto arbitrary substrate have been demonstrated, such as using the thermal release tape. [29, 30]

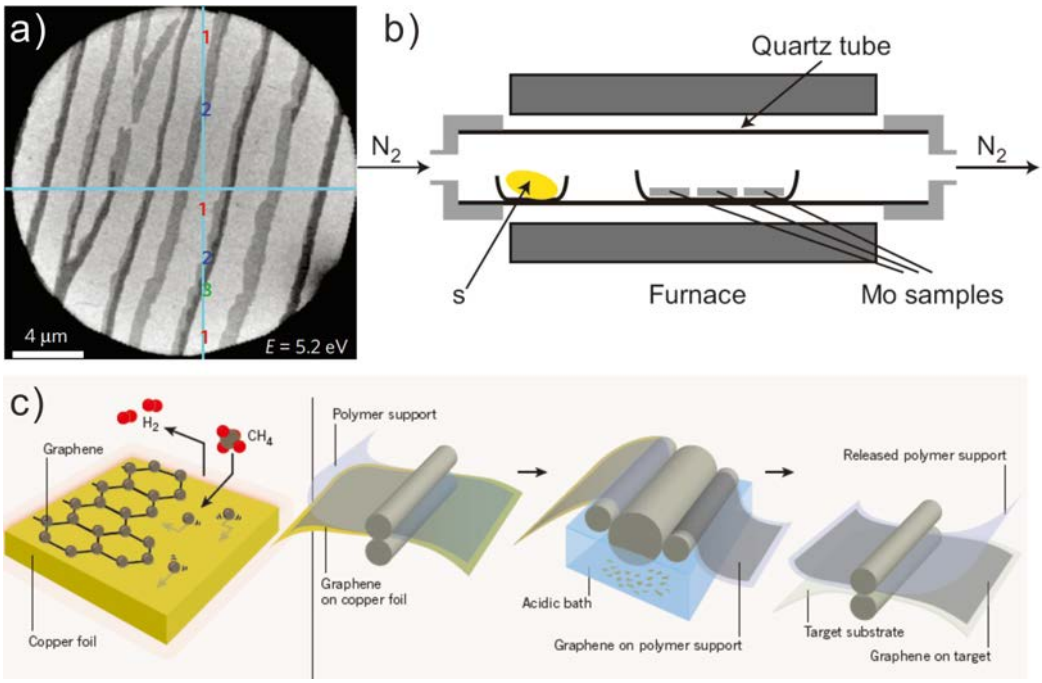

Figure 2.2. a) Close-up low energy electron microscopy image of graphene with monolayer coverage on the terrace and bilayer/trilayer growth at the step edges.[26] b) Schematic illustration of single- to few-layered MoS2 by sulfurization of Mo thin film.[31] c) The formation of graphene films by CVD of carbon atoms onto a copper surface and subsequent roll-to-roll transfer to target substrate.[32]

2.2.2 CVD-Grown 2D Nanomaterials

The CVD technique is actually not very new, which has been attempted by Blakely and his group to study the thermodynamics of growth "monolayer graphite and bilayer graphite" on Ni (111) crystals in 1970s. In the CVD growth of graphene, carbon sources such as CH_4 gas, methanol, or poly(methyl methacrylate) (PMMA) can be catalyzed by metals to deposit carbon atoms on metal surfaces and form large area graphene with the quality subject to the reaction temperature (usually 800~1000 ^oC) and vacuum degree.[33-36] The graphene can be transferred to the arbitrary substrate after removal of the metal substrate using chemical etching agent. There are various suitable metal substrates, such as Co, Pt, Ru, Ni and so on,[37-40] among which Cu and Ni are mostly used. Compared to nickel-based CVD growth, copper can lead to lager higher percentage of single layer graphene with larger grain size after annealing process.

Many efforts have been paid to the development of CVD method, because it on one hand can readily control the growth thickness of graphene sheets and on the other hand can produce large size graphene ranging from tens of microns up to 30 inches.[41] Moreover CVD method can facilitate the substitutional doping process via introducing heteroatoms such as nitrogen and boron, which will favor the functionalization or fine tune of graphene transistors. Add to that CVD-grown graphene could be patterned by microfabrication techniques and is thus suitable for miniaturized devices and high-density electric circuits.

CVD methods for growing ultrathin TMDs have been demonstrated. Take MoS_2 for an example, various solid precursors are selected to prepare atomically thin films of MoS_2: substrates dip-coated in ammonium thiomolybdates [$(NH4)_2MoS_4$] and heated in sulfur vapor via a two-step thermolysis;[42] gas-phase reaction of sulfur powder and MoO_3 powder and co-deposited on nearby substrates;[43-45] sulfurization of Mo metal thin films.[31] More recently, CVD syntheses of other 2D TMDs have been reported, such as $MoSe_2$,[46] WS_2,[47, 48] WSe_2.[49, 50]

However, there are also some inevitable drawbacks of this CVD method. For practical applications, CVD-grown thin films have to be transferred to the target substrate. In order to protect the intactness of 2D thin films from breaking into small fragments due to water surface tension during the transfer process, a layer of protective polymer, such as PMMA needs to be coated onto surface prior to etching away metal substrate. Subsequently, PMMA is got rid of by dissolving in acetone. As evidenced by experiments, additional detriments are induced with respect to the quality and continuity of 2D thin films, such as PMMA residues, cracks and contaminations, which will exert undesirable impact on the physical and electronic properties.

2.2.3 Micromechanical Exfoliation

Mechanical exfoliation method of layered compounds has been used for some time to produce thin samples. Because Layered materials comprise of strong in-

plane chemical bonds but weak out-of-plane interaction, namely van der Waals force, complete top-down exfoliation of these bulk layered materials to yield thin nanosheets at nanometer or even atomic thickness is possible. In 1999, Ruoff's group[51] attempted the exfoliation of graphite pillars by manipulating an atomic force microscope (AFM) tip, in which graphite pillars were patterned into highly oriented pyrolytic graphite (HOPG) by plasma etching (Figure 2.2a). The thinnest slabs were observed at that time more than 200 nm thick, which is equivalent of ~600 layers. Subsequently, Kim et al. modified the method by using the mounted graphite on the cantilever as the tip of AFM in order to transfer thin graphite samples onto a SiO_2/Si substrate.[52] Graphite crystallites with a thicknesses of 10 nm to 100 nm and a lateral size of ~2 μm were successfully extracted from bulk counterparts (Figure 2.2b). But these methods don't give birth to the monolayer graphene sheet until 2004 when it is first discovered by Geim and Novoselov,[1] who were therefore awarded the 2010 Nobel Prize in physics. They developed quite a simple way to realize the successful exfoliation of graphite into single-layer graphene, i.e. Scotch tape or peeling-off method. After repeated peeling of small mesas of highly oriented pyrolytic graphite, the tape is ultimately pressed down against a substrate to deposit a sample (Figure 2.2c). The flakes present on the tape might be much thicker than one layer, but van der Waals attraction to the substrate can facilitate the delamination of a single sheet when the tape is lifted away.

Such a method, not limited to graphite, is also suitable for exfoliation of other layered materials. Various 2D nanomaterials are successfully peeled from their parent bulk crystals by using adhesive tapes, such as BN, and TMDs[52-55] and optically identified by light interference.[56, 57] Although micromechanical cleavage can produce defect-free samples, which is suitable for the fundamental study, its low throughput restricts the application, hardly meeting the requirements of large-scale production and applications.

2.2.4 Chemical Exfoliation

Taking into account the drawbacks of mechanical exfoliation method, such as the low yield and unlikelihood of industrial scalability, the challenge of developing

other alternative routes to produce 2D nanomaterials (particularly refers to graphene synthesis) has become the focus of many researches. Beyond the scalability, this process should on one hand produce high-quality graphene nanosheets without compromising high mobility, on the other hand provide controllable manners over the sheet thickness with respect to building devices with uniform performance, ease of integration into peripheral systems as well as compatibility with various substrates.

Among the follow-up strategies, graphite oxide, the oxidized form of graphite derived from the chemical oxidation of graphite, is regarded as a more important and frequently used method. The preparation of graphite has evolved for centuries and during this period two alternative routes developed by Staudenmaier in 1898[58] and Hummers in 1958[59] are more accepted. However, due to more time-consuming and hazardous of previous methods, Hummer's method remains a more widely used approach to produce graphite oxide by using graphite and an anhydrous mixture of concentrated sulfuric acid, sodium nitrate and potassium permanganate. Graphite oxide can be easily exfoliated to produce single-layer graphene oxide (GO) through ultrasonication[60] or mechanical stirring of graphite oxide aqueous solution for long time[61]. Graphene oxide, an important graphene derivative, comprises of plenty of oxygen-containing functional groups on its edges and basal plane such as carboxyl, epoxy and hydroxyl, the presence of which results in a larger interlayer spacing (6-12 Å) than graphite (3.4 Å) and offer active sites for graphene functionalization via covalent or noncovalent manners, such as integrating biorecognition molecules to fabricate biosensors,[62] modified as buffer layer in polymer solar cells[63] and so on. Graphene can be obtained by thermal, chemical or photo reduction of graphene oxide to restore its π-conjugated structure, i.e. reduced graphene oxide (rGO).[64-68] Graphene production in such a way is low-cost and highly scalable up to a ton scale, nevertheless, the large amount of residue defects caused by incomplete reduction process significant limits the applications in electronics and optical devices.[13, 65, 69] Compared to the mechanically exfoliated pristine graphene, rGO is of lower quality because the conductivity and charge carrier mobility are jeopardized.

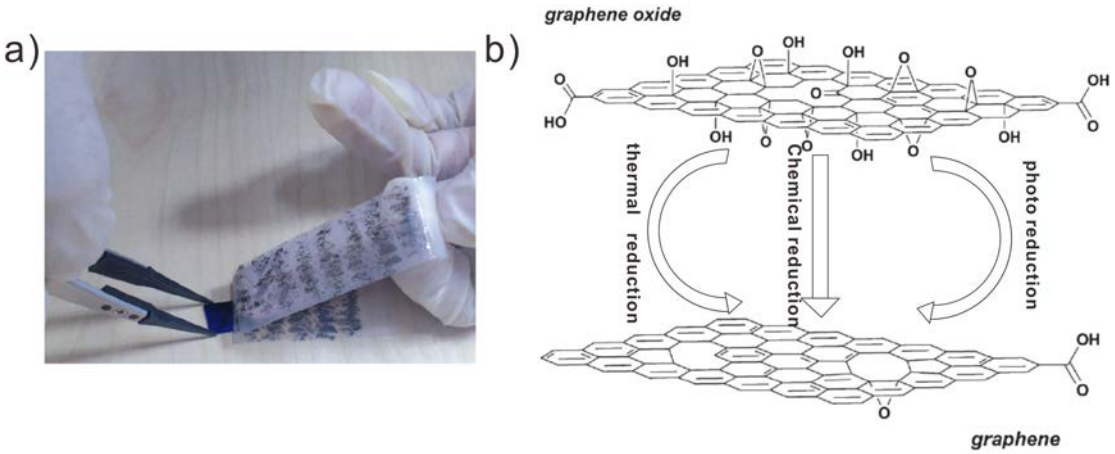

Figure 2.3. a) Micromechanical exfoliation of graphite by using the scotch tape. b) Production of graphene oxide by chemical exfoliation and subsequent reduction into rGO.

2.2.5 Liquid-based Direct Exfoliation

More recently, another top-down exfoliation strategy, i.e. liquid-based direct exfoliation (LBE), shows remarkable progress in making many kinds of 2D nanomaterials. LBE refers to a collection of methods that directly exfoliate bulk materials into 2D nanomaterials in the liquid media without the need for chemical oxidation of the bulk materials (Figure 2.4). It includes not only ultrasonic exfoliation in organic solvents, but also other approaches where the exfoliation process mainly happen by taking advantage of the liquid media, such as the liquid phase exfoliation by surfactants, ionic liquids, salts and etc., the electrochemical exfoliation in various liquid media and the shear exfoliation method. This LBE strategy is getting more and more attention because it represents an extraordinary versatile, potentially up-scalable and sustainable route for the production of a wide variety of (or virtually any) 2D nanomaterials. The as-made 2D nanomaterials show desirable materials properties and good solution dispersing ability, which significantly facilitate the formation of functional composites and hybrids by simple mixing and is convenient for casting into different thin films for device and coating applications.

Figure 2.4. Schematic illustration of Liquid-based direct exfoliation of bulk-layered crystals.

2.2.5.1 Direct Ultrasonic Exfoliation in Liquid

Direct ultrasonic exfoliation in liquid refers to a collection of methods, which produce 2D nanosheets by direct ultrasonication of their bulk materials in liquid media. There are two crucial parameters involved in this method. One is the commonly required ultrasonication (bath sonication or probe sonication). Layered materials can be successfully exfoliated upon exposure to the ultrasonic waves. Such waves can generate shear forces or cavitation bubbles,[70] which will afford high energy upon collapse of bubbles or voids in liquids to break up the layered structure and produce single- or few-layered nanosheets. The liquid media, such as the organic solvent or the aqueous solutions of stabilizers, ionic liquids, and salts, also plays important roles in the reduction of the potential energy barrier existed in the interlayers of the bulk materials and subsequent stabilization of nanosheets via interfacial interactions.

Organic-solvent based exfoliation involves the dispersion of bulk-layered materials in a selected organic solvent, ultrasonic exfoliation and subsequent purification process. A suitable solvent will reduce the potential energy between adjacent layers (energy minimization) to overcome the van der Waals attraction and the solvent-nanosheets interaction could balance the inter-sheet attractive forces to stabilize the dispersion of nanosheets.[71] Two independent groups reported the first successful direct exfoliation of natural graphite powders in organic solvents in 2008.[72, 73] After that many efforts have been devoted to more in-depth study in the interaction between organic solvents and solid flakes, pursuit of proper solvents for the effective exfoliation, and improvement of the stability of concentrated dispersion of graphene sheets. Coleman's group performed a library survey of organic solvents used in the liquid exfoliation of graphite. They found the best solvents for producing large quantities of graphene sheets should have a surface tension around 40 mJ m^{-2} (equal to a surface energy of 70 mJ m^{-2}), such as N-methyl-2-pyrrolidone (NMP ~40 mJ m^{-2}), and N,N-dimethylformamide (DMF ~37.1 mJ m^{-2}), which matches the surface energy of graphene (68 mJ m^{-2}) (Figure 2.5).[73] The absence of D band of large graphene flakes in Raman measurement confirmed the ultrasonic process did not introduce any structural defects, while its appearance in small graphene flakes was mainly due to the edge defects. Transmission electron microscopy (TEM) measurement shows that the exfoliated graphene sheets are single and few layers, with a dispersion concentration of 0.01 mg mL^{-1} and a lateral size of ~500 nm to 3 μm. In order to further improve the graphene yield, alternative organic solvents have been attempted. For example, ortho-dichlorobenzene (ODCB) increased the concentration to ~0.03 mg mL^{-1} via π-π stacking interaction with graphene,[74] while perfluorinated aromatic molecules such as C_6F_5CN could give a stable concentration of 0.1 mg mL^{-1} through the matching surface energy and donor-acceptor interactions.[75] Apart from searching for more suitable solvents, other factors such as ultrasonication time and power are also investigated to increase the yield. Khan et al. reported the improved graphene concentrations up to 1.2 mg mL^{-1} with ~4 wt% monolayers by simple low-power ultrasonication in NMP for very long time, up to 460 h.[76]

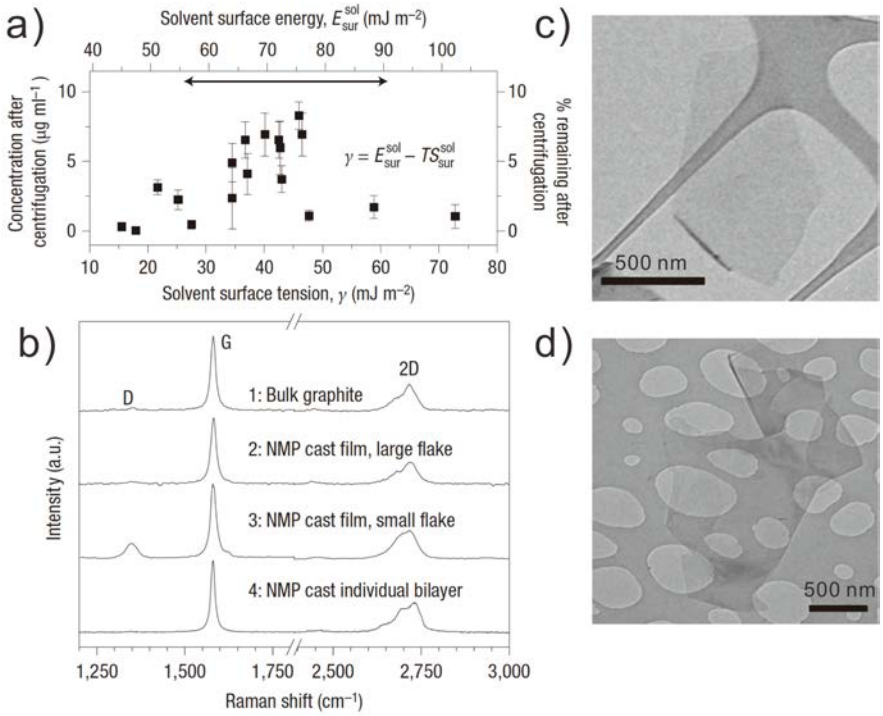

Figure 2.5. Concentration of graphene dispersions produced by various solvents plotted versus solvent surface tension. b) Raman spectra of bulk graphite and graphene flakes. c) and d) TEM images of monolayer graphene and folded graphene sheets. Reproduced with permission.[73]

Unfortunately, some disadvantages also exist for the dispersions of graphene in aforementioned solvents, especially for good solvents such as NMP and DMF. Their high boiling point and toxicity would hinder applications where solvent residues may greatly deteriorate the device performance. To address this issue, low boiling point solvents including isopropanol (82 ^{o}C),[77] chloroform (61 ^{o}C),[78] acetonitrile (ACN, 81.6 ^{o}C)[79] have been reported, giving a concentration of 0.5~1 mg mL^{-1}.

Other than graphite, more bulk-layered materials could be processed in such a solvent-based exfoliation to yield good quality, high concentration and stable dispersions of 2D nanosheets, such as MoS_2, WS_2 and BN.[80-84]

Although direct exfoliation in organic solvents is simple and straightforward, the use of organic solvent is less environmentally friendly. To address this issue, stabilizer-based exfoliation is developed to produce 2D nanomaterials in the

aqueous solutions under the assistance of stabilizers including surfactants, polymers and pyrene derivatives. The use of stabilizer can effectively tune the surface tension of the aqueous solution so as to allow efficient exfoliation. A variety of ionic surfactants are brought into the spotlight, which includes anionic surfactants, such as sodium dodecylbenzene sulfonate (SDBS),[85] sodium cholate (SC),[86] and sodium deoxycholate (SDC) bile salt[87] and cationic surfactants, such as cetyltrimethylammonium bromide (CTAB).[88] The presence of ionic surfactants can facilitate the exfoliation and stabilize as-obtained 2D nanomaterials via the electrostatic repulsion between each other. This can be ascribed to the special structure of ionic surfactants, where the hydrophobic tail groups can absorb non-polar objects via various interactions such as van der Waals interactions and hydrophobic interactions; while the hydrophilic head groups are prone to dissociate to endow the flakes charged. Well-dispersed 2D nanomaterials not limited to graphene but also TMDs, BN and MnO_2 can be readily obtained.[89]

Non-ionic surfactants tend to stabilize the graphene dispersion better than ionic ones, probably due to the more efficient steric repulsion than electrostatic repulsion. The hydrophobic tail absorbs on exfoliated sheets while the long hydrophilic part spreads into water. Once the graphene sheets approach close to each other, the protruding head groups will interact to induce osmotic repulsion. Guardia and coworkers who prepared graphene aqueous dispersion in a wide range of non-ionic surfactants in comparison with several ionic ones via direct bath sonication in water found that the concentration of graphene dispersion obtained from non-ionic surfactant was much higher (Figure 2.6).[90] The outcome from Smith et al. demonstrated that the dispersion concentration scaled linearly with steric repulsive potential barrier.[91]

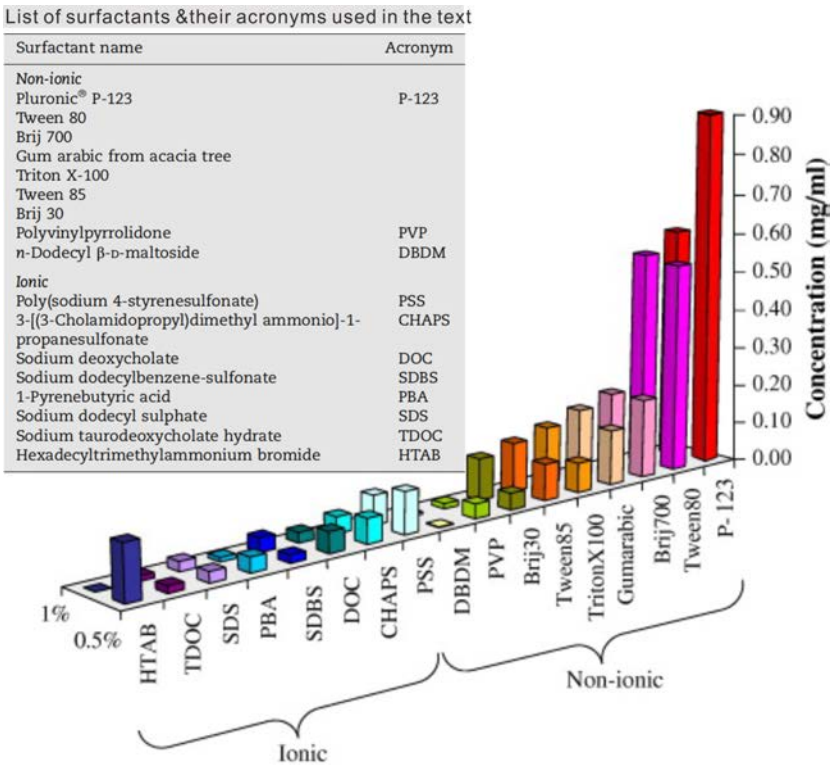

Figure 2.6. Concentration of graphene dispersions obtained by various types of surfactants. Reproduced with permission.[90]

Generally, larger concentrations of small molecular surfactants and polymers will lead to high dispersion concentration of graphene nanosheets. However, difficulties of removal of excessive stabilizer in dispersion may impose negative effects on the performance of films, composites and electronic devices. Therefore, search for alternative stabilizers that can stabilize large amount of graphene sheets at low concentrations is necessary. Polycyclic aromatic hydrocarbons (PAH) such as pyrene (Py) and its derivatives show great promise in this respect due to π-π interactions between the planar surfaces of stabilizer and graphene.[92-99] Ionic liquids (ILs), a type of semiorganic salts with a melting point below 100 ^{o}C, can also be used in the stabilization of graphene nanosheets via Coulombic interaction.[100-102]

Different from the abovementioned liquid media, which take effect via surface interaction with layered materials, Li^{+}-assisted exfoliation method shows another mechanism. This method involved the intercalation of Li^{+} by soaking MoS_2 powders in the hexane solution of BuLi for 48 h and subsequent reaction of the

dried intermediate product with water under ultrasonication. The released gaseous hydrogen can force the layers apart.[103-105] Note that this Li-assisted exfoliation has drawbacks owing to its sensitivity to ambient conditions; therefore more attention should be paid to the intercalation process, which is normally conducted in inert gas-filled glovebox.

2.2.5.2 Electrochemical Exfoliation

Unlike the direct ultrasonic exfoliation method that typically requires longer time, the electrochemical exfoliation of bulk-layered materials in a two-electrode system can be accomplished in minutes. The basic concept of electrochemical exfoliation is to intercalate ionic species into bulk-layered materials under an electrochemical bias, and to facilitate the subsequent ultrasonic exfoliation. The experimental setup for electrochemical exfoliation with anionic species involves using bulk-layered materials as anode and another material (such as Pt) as counter electrode (Figure 2.7). It is found that the electrolyte that contains anionic SO_4^{2-} was effective in the exfoliation of bulk-layered materials, such as H_2SO_4 aqueous solution[106, 107] and SO_4^{2-}-containing salt solution[108, 109]. The oxidation of water under bias voltage generated hydroxyl and oxygen radicals, which would induce oxidation and hydroxylation to edge sites and grain boundaries of graphite electrode. The defective sites could facilitate the intercalation of SO_4^{2-} into graphite interlayers. Subsequently, the expansion of interlayer spacing occurred due to the release of gaseous SO_2 or anion depolarization (Figure 2.7e). Moreover, other electrolyte containing either surfactant (e.g. poly(sodium-4-styrenesulfonate))[110] or ILs[111, 112] was proved to be effectively produce 2D nanomaterials.

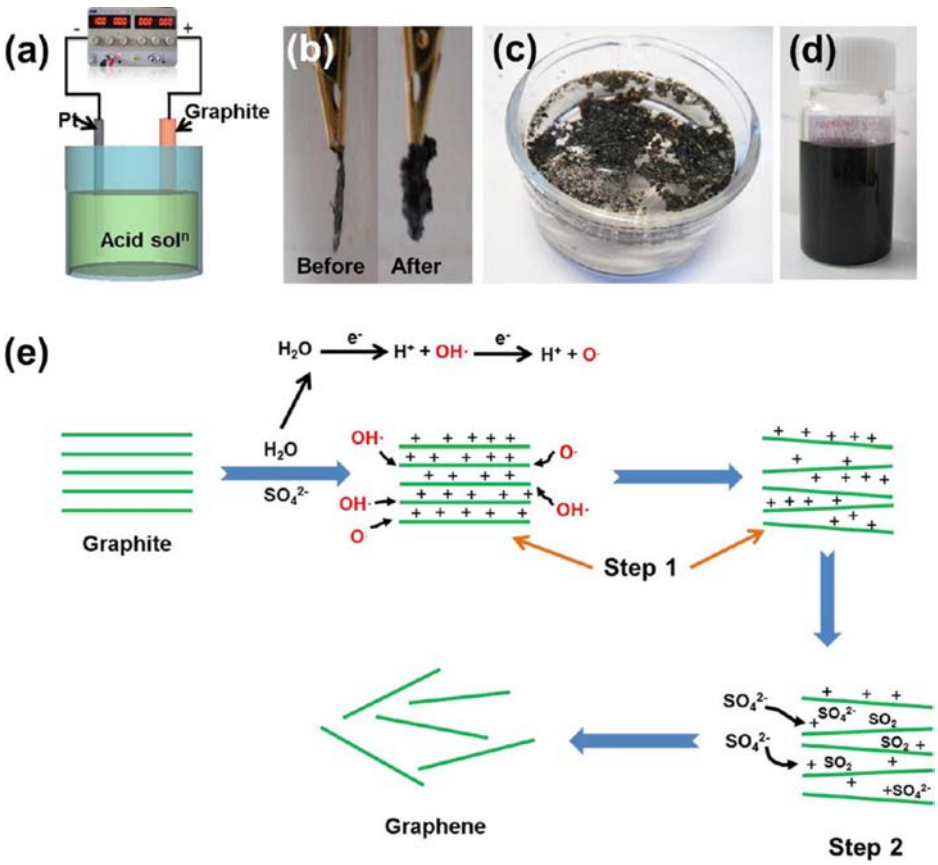

Figure 2.7. a) Schematic illustration of electrochemical exfoliation of graphite in acid solution. b) Photos of graphite flakes before and after exfoliation. c) Exfoliated graphene floated on top of water. d) Dispersed graphene sheets in DMF. e) Proposed mechanism for electrochemical exfoliation.[107]

Other than the anions that can help produce 2D nanomaterials in electrochemical exfoliation, cations such as Li^+ also plays an important role. Unlike direct Li-assisted exfoliation that requires high reaction temperature (e.g. 100 ^oC) and long reaction time up to several days, and lacks of the controllability over the degree of Li intercalation, Zeng et al. developed a simple and effective method to fabricate single-layered 2D nanomaterials with high yield through a controllable lithiation process (Figure 2.8). In this method, bulk-layered materials, such as MoS_2, WS_2, TiS_2, TaS_2, ZrS_2 and graphite, were incorporated into an electrochemical setup as cathode, and the Li foil served as anode to provide Li ions.[113, 114] The efficiency of Li^+ intercalation was remarkably improved under the electrochemical bias, compared to the previous pure ionic diffusion. This whole process was easily finished within 6 h at room temperature and the lithiation could be monitored and well controlled in a battery system. It avoids

either the incomplete Li insertion that produces low yield of single-layered 2D materials or the over insertion that can result in decomposition and formation of metal nanoparticles and LiS_2.[115] It is worth noting that this method would alter the electronic properties from semiconducting to metallic (e.g. MoS_2) and additional annealing at 300 ^oC was required to restore their intrinsic properties.[116]

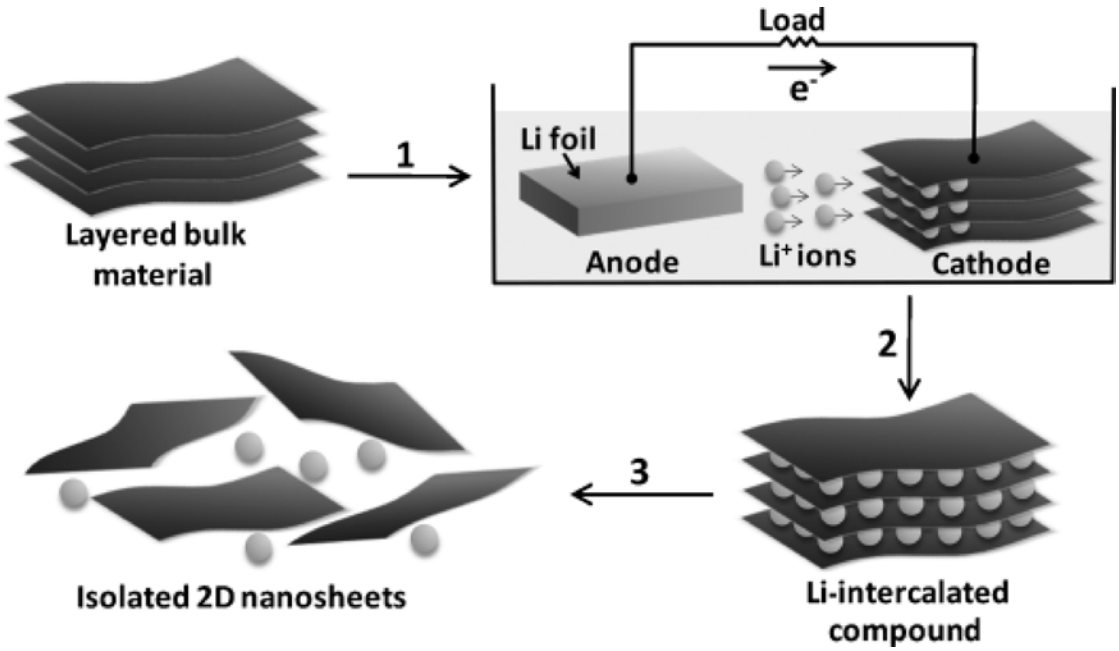

Figure 2.8. Schematic of electrochemical lithiation process for the production of 2D nanosheets from bulk-layered crystals.[113]

2.2.5.3 Shear Exfoliation

Previously, shear mixing is popular in the dispersion of aggregated nanoparticles that are weakly bound together in liquids. This method has been reported in papers and patents as part of the process for the exfoliation of graphite and other layered materials.[117-119] In all cases, these bulk-layered materials (e.g. graphite and TaS_2) were firstly treated with sulfuric acid, through which it could form intercalated intermediate products with weakened interlayer bonding, and then the shear force exfoliation was conducted. The synthesized flakes were usually thick, ranging from 10 nm to 100 nm. It is the intercalation process rather than shear force exfoliation that determines the exfoliation efficiency. This will restrict the potential of scaleup production as well.

This issue was recently addressed by Coleman's group via a high-shear method without the need for the pre-intercalation step. Paton et al. demonstrated that high-shear mixing of graphite in suitable stabilizing liquids led to large-scale production of defect-free graphene sheets.[120] In this method, the shear mixer consisting of rotor and stator (or rotating blades) was used to generate high shear rates in liquids, to which the layered powders were added. So long as the interaction between liquid media and layered material energetically allows the exfoliation and the liquid can stabilize as-produced nanosheets, the shear forces will cause delamination of nanosheets from the layered crystal. The exfoliation process could happen once the local shear rate exceeding 10^4 s^{-1} as unveiled in the simple model. The scalability of this shear exfoliation method was also carefully investigated, showing that it was closely related to such variables as the initial graphite concentration (C_i), mixing time (t), rotor diameter (D), liquid volume (V) and rotor speed (N). These parameters followed a certain scaling law (Figure 11c). This superlinear relationship between production rate and liquid volume made scaleup a reality. The exfoliation could be achieved in liquid volumes up to hundreds of liters with a production rate of 1.44 g h^{-1} for graphene, far higher than previously reported ultrasonication methods. Meanwhile, it gave defect-free nanosheets with dimensions similar to those produced by ultrasonication methods.

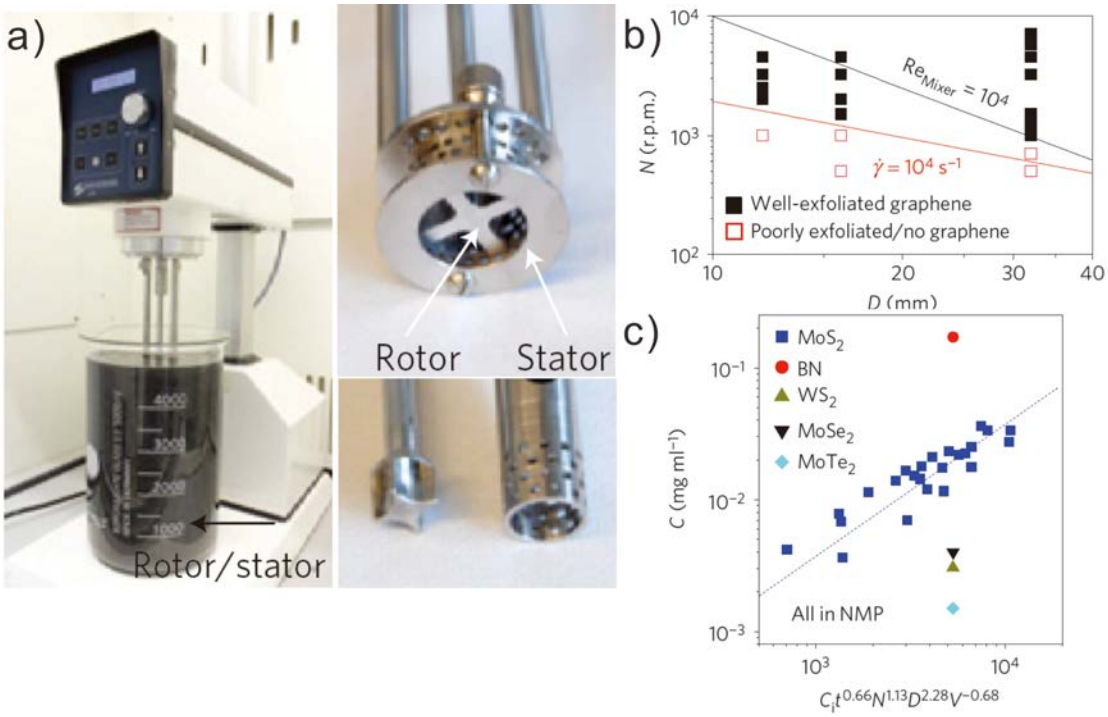

Figure 2.9. a) Set-up of high shear mixer in graphene dispersion with close-up view of rotor and stator. b) Diagram of rotor speed, N versus diameter, D. The red line represents a minimum shear rate $\gamma \approx 10^4\ s^{-1}$. c) Concentration of 2D nanosheets dispersed in NMP following the certain scaling behavior.[120]

2.3 2D Nanomaterials-based Composites

Due to the hydrophobic characteristic of pristine graphene, its solubility in water and most of the solvents without the assistance of dispersing reagents is not appreciable, which renders it a concern in the processing of graphene composites. In order to improve the solubility, functional groups have been introduced and anchored to the carbon backbone by chemical modification,[121, 122] covalent[123, 124] or noncovalent functionalization.[12, 125]

2.3.1 2D Nanomaterial-Inorganic Composites

As an ideal template, inorganic nanomaterials including metal nanoparticles (NPs), metal nanowires and semiconductor materials have been synthesized on the top of graphene surface. Those attempted NPs such as Au,[126-129] Pd,[130, 131] Ni,[132] and Cu,[133] and metal NWs[134-136] have been applied in different areas

such as the catalysis, electrochemical sensing[137, 138] and the surface-enhanced Raman scattering.[139] The graphene-metal NP composites can be mainly fabricated by chemical reduction.[138, 140] And other methods, such as photochemical synthesis,[127] microwave-assisted synthesis,[133] electroless metallization[141] and thermal evaporation,[142] are applied as the supplements or alternatives.

Regarding those semiconductor nanomaterials, such as TiO_2,[143-145] ZnO,[146-148] SnO_2,[149, 150] MnO_2,[151, 152] Co_3O_4,[153, 154] and chalcogenides CdSe,[155, 156] they show promising applications in electronics, optics and energy-based devices such as solar cells, batteries and supercapacitors. The fabrication methods for graphene-semiconductor composites include in-situ crystallization, solution mixing, microwave-assisted growth, electroless deposition and vapor deposition.

2.3.2 2D Nanomaterial-Polymer Composites

The combination of graphene and polymer to form graphene-polymer composites also shows promising properties and performances. And the performances depend on not only the quality of graphene filler and polymer matrix, but also the dispersity of the filler, the bonding and ratio between one another. Based on the interaction of graphene and polymers, the graphene-polymer composites can be classified into three types, graphene-filler polymer composites, layered graphene-polymer films and polymer-functionalized graphene sheets.[157, 158] Similar to the conventional polymer processing, the methods applied for the fabrication of graphene-polymer composites includes: solution mixing,[159, 160] melt blending[161] and in-situ polymerization[162, 163].

2.3.3 Other Composites

Other than the two types mentioned above, materials such as organic molecules,[164, 165] metal-organic frameworks (MOF),[166] biomaterials,[167, 168] and carbon nanotubes (CNTs)[169-171] have been incorporated into graphene to form composites. For example, N, N'-dioctyl-3, 4, 9, 10-perylenedicarboximide (PDI)-GO core-shell wires were formed through the π-π interaction, which was

used in solar cells.[164] MOF-5 growing on a template of benzoic acid-functionalized graphene shows a wire-like structure.[166]

2.4 Applications of 2D Nanomaterials in Electronics

Due to the excellent physical and chemical properties and as-established synthetic methods for both solid and solution process, graphene and 2D TMDs has exhibited great potentials and been regarded as the building blocks for a variety of applications, such as FETs,[172-178] supercapacitors,[152, 171, 179, 180] memory devices,[181-185] photocatalysis,[186-188] sensors,[62, 189-191] photovoltaic devices[83, 192-204] and the like.

Among those applications, photovoltaics devices that can harvest the sunlight and convert the solar energy into electricity are the foremost priority of our research. Organic photovoltaics (OPVs) typically consist of electrodes (anode and cathode), a mixture of n-type and p-type organic semiconductor, and buffer layers. For perovskite solar cells, the only difference is the active layer. Therefore its performance including open circuit voltage (V_{oc}), short circuit current (J_{sc}), fill factor (FF) and long-term stability is closely related to material properties of each layer. 2D nanomaterials owing to their excellent physical and chemical properties has been intensively investigated by incorporating into OPVs as various essential parts, such as transparent electrodes, hole transport layers (HTLs), electron transport layers (ETLs), n-type acceptors and packaging layers.

2.4.1 Transparent Electrodes

Traditionally, transparent conductive oxides, such as indium tin oxide (ITO) and fluorine-doped tin oxide (FTO), play a dominant role in OPVs because of their high transparency of 80~90% and low sheet resistance 10~30 Ω. However, there are some disadvantages including increasing price, scarce of reservation, rigidity and incompatibility with flexible substrates and instability towards the acid or base that have seriously impeded the future applications. As a result, many efforts have been devoted to seeking for new materials of low cost, flexible and compatible with large-scale manufacturing process to replace ITO for OPV applications. Currently, alternative electrodes including CNTs,[205-207] metal

grids,[208, 209] metallic nanowires,[210, 211] conductive polymers like poly(3,4-ethylenedioxythiophene):poly(styrene sulfonate) (PEDOT:PSS)[212, 213] and graphene films[214, 215] have been demonstrated. CNTs are relatively cheap and easily deposited into large-area, conductive thin films, but the tube-tube contact resistance is high, which limits the conductive pathways within the whole films.[216] Metal grids that usually involve the photolithography and subsequent metal evaporation process are restricted to prepare large area electrodes. Metallic nanowires can be prepared by solution process and exhibit performance comparable to ITO with respect to the transparency (>85%) and sheet resistance (<20 Ω).[210, 217] Nevertheless, it might be limited due to the rough surface that easily leads to a short circuit and poor adhesion to substrates that is not solid enough to withstand any friction. Though PEDOT:PSS after doping exhibits high conductivity and can serve as the electrode in OPV devices[218], its instability upon the exposure to the environment is a major problem for the practical applications. It appears that the conductive and chemically stable graphene has an edge over others. As a matter of fact, the sheet resistance of graphene, whatever the approach it is made from is higher, usually on the scale of kΩ sq^{-1}. Thus, doping or modification has to be conducted to lower down its sheet resistance so as to quality for the electrodes in OPVs.

Key points of graphene anode in OPVs lie in the conductivity, work function and surface property. Pristine CVD graphene has a much lower conductivity than that of ITO and its work function (~4.5 eV) mismatches the highest occupied molecular orbit (HOMO) of most donor organic semiconductors (~5.0 eV), which will result in the hole-injection barrier between graphene and donor materials. Therefore it is necessary to modify graphene by p-type doping so as to be suitable for the anode in OPVs. Several approaches could achieve p-type doping effect, such as the acid treatment,[219, 220] molecule coating[221] or metallic contact[222]. The work function of few-layer CVD graphene was improved from 4.2 to 4.7 eV by non-covalently binding with pyrene butanoic acid succidymidyl ester (PBASE) via π-π interaction.[223] The strong electron affinity of PBASE aromatic rings can withdraw electrons from graphene to induce p-type doping. The modified graphene was integrated as anode into OPVs with a structure of graphene/PEDOT:PSS/P3HT:PCBM/LiF/Al. Compared to the unmodified

graphene, the power conversion efficiency (PCE) of as-fabricated OPVs was increased from 0.21% to 1.71%. Park et al. reported the p-type doping of CVD graphene by using $AuCl_3$, which can not only improve the conductivity but also alter the work function and surface wettability.[224] Thus the PCE was significantly improved from 0.53% to 1.63%. Multilayer graphene with higher conductivity can be acquired by layer-by-layer (LBL) transfer method.[200] Four-layer graphene film after further doping by HCl and HNO_3 has a sheet resistance of ~80 Ω sq^{-1} and a transmittance of ~90% at 550 nm. Subsequently the evaporation of a thin layer of MoO_3 (2 nm) on graphene surface allows the effectively spreading of PEDOT:PSS and also improve work function from 4.36 eV to 5.47 eV. The work function is favorable for the hole extraction and a PCE of 2.5% was obtained. Hsu et al. reported a LBL doping process of multilayer graphene via thermal evaporation of tetracyanoquinodimethane (TCNQ) molecules onto the surface of each layer. Three layers of graphene showed a sheet resistance of ~140 Ω sq^{-1} and a transmittance of ~90% and the OPV device exhibited a maximum PCE of 2.58%. More approaches were developed to deal with graphene's hydrophobic surface: thermal evaporation of PEDOT film,[225] insertion of a more wettable layer of PEDOT:poly(ethylene glycol) (PEG) between graphene and PEDOT:PSS,[226] mixing PEDOT:PSS with IPA,[227] or using another polythiophene derivative RG 1200.[228] Apart from building the device structure onto the rigid substrates, graphene electrode-based OPVs can also be constructed onto flexible substrates thanks to its excellent mechanical strength. Lee et al. transferred multilayer graphene on PET, doped with HNO_3 and $SOCl_2$ and obtained flexible OPVs with a PCE of 2.5%.[229] Liu et al fabricated the flexible OPVs on the polyimide (PI) substrate by using two-layer graphene doped with PEDOT:PSS and Au nanoparticles. The optimized OPVs showed a PCE of ~3.2% and excellent bending stability with 8% decrease of PCE even after 1000 cycles bending test.[230] Using the same doping treatment, they integrated single-layer graphene into semitransparent OPVs as top electrode. The electrode showed a sheet resistance <100 Ω sq^{-1} and a transmittance of ~90% and the device based on P3HT:PCBM (Poly(3-hexylthiophene):[6,6]-Phenyl-C61-butyric acid methyl ester) exhibited higher PCEs of ~3% when illuminated from graphene electrodes due to the high transparency (Figure 2.10a).[231] Very recently, You et al. reported the fabrication of semitransparent perovskite solar

cells with graphene electrodes. The device shows a maximum PCE of 12.02%.[232]

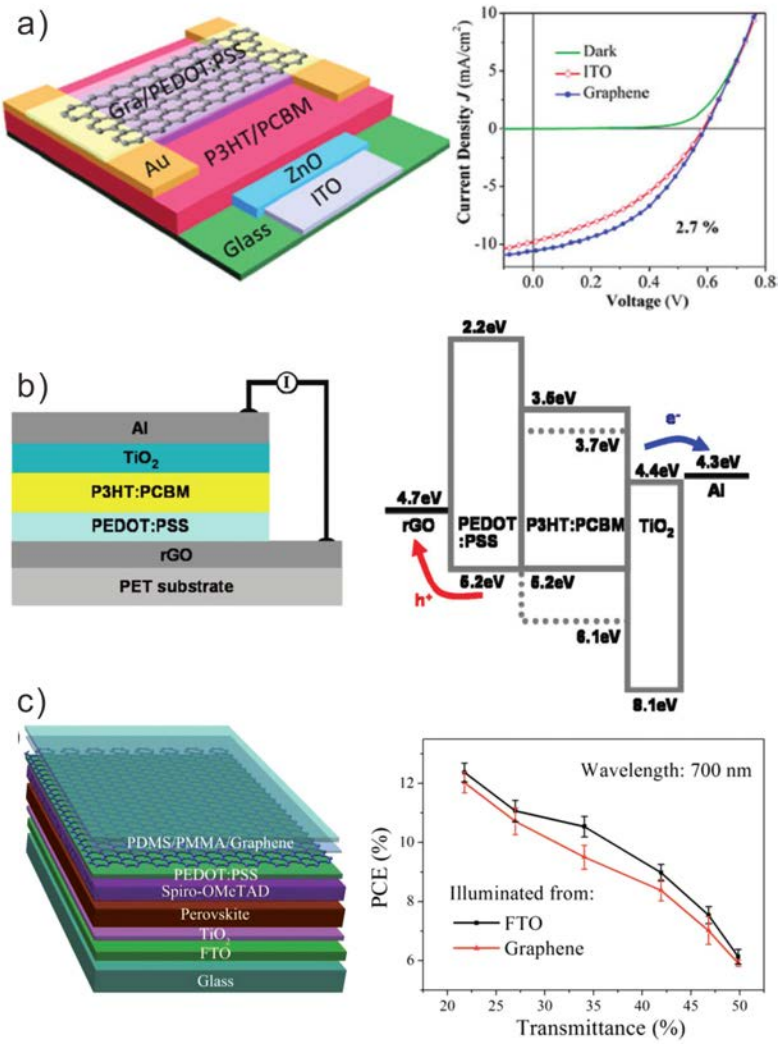

Figure 2.10. Schemes of as-fabricated OSCs with transparent graphene electrodes prepared by multiple CVD graphene transfer a)[231] and rGO b)[93] c) A semitransparent perovskite solar cell and the corresponding PCEs as a function of transmittance.[232]

Beyond CVD graphene, solution processable rGO has also been widely investigated for preparing the transparent electrode for OPVs owing to the low cost and facile fabrication process. Plenty of methods could be used to prepare the rGO thin films, such as spin-coating, dip-coating, vacuum filtration and Langmuir-Blodgett assembly (LB). Note that the pure rGO films still face the same issue: low conductivity. rGO thin films generally have a sheet resistance of hundreds of kΩ sq^{-1} at higher transmittance and the reported OPVs exhibited

quite a low PCE (<0.4%) (Figure 2.10b).[93, 192] Hence, chemical doping[233] or hybrid rGO films are necessitated to improve the conductivity.

For the graphene cathode in OPVs, not only the high conductivity is essential, but also an appropriate work function that can match the lowest unoccupied molecular orbit (LUMO) of n-type organic semiconductors to facilitate the collection of electrons is requisite. Pristine CVD graphene often shows a p-type doping effect due to the physical absorption of moisture and oxygen, therefore it is necessary to n-type dope graphene to lower down the work function.

N-type doping by the substitution of carbon with nitrogen or boron atoms is not an ideal manner, because it results in more defects and deteriorate the carrier mobilities of graphene.[234, 235] Alkali carbonate salts (e.g. Cs_2CO_3, and Li_2CO_3) could be another way to accomplish the n-type doping of graphene.[236] Through this way, Huang et al. found the efficiencies of OPVs increased with the decrease of work function of rGO-CNT cathodes.[237] Self-assembled monolayer polymers with dipole moment can also tune the work function.[238, 239] Polymer (WPF-6-oxy-F) doped graphene can decrease the work function from 4.58 eV to 4.52 eV and the inverted OPV structure graphene (WPF-6-oxy-F)/P3HT:PCBM/PEDOT:PSS/Al exhibited a maximum PCE of 1.23%. Moreover, the deposition of low work function metal on graphene surface is also studied. Zhang et al fabricated an inverted device with a structure of graphene/Al/TiO_2/P3HT:PCBM/MoO_3/Ag and the device showed a PCE of 1.59%.[240]

2.4.2 Buffer Layers

The buffer layers consist of two types: HTL and ETL. In OPVs, a HTL that should be p-type with a wide bandgap plays important roles as follows: 1) to minimize the energetic barrier and inhibit the reaction between the active layer and electrode; 2) to transport holes meanwhile blocking electrons; 3) to enable good morphology of active layer; 4) to serve as an optical spacer.[204, 241] For long time, solution processable PEDOT:PSS dominates among various HTLs to minimize the energy barrier between the active layer and ITO and shows

promising performance. However, its high acidic nature inevitably erodes the ITO electrodes and leads to instability of OPVs. Some other alternatives have been attempted including MoO_3,[242] NiO,[243] and V_2O_5,[244] while they are usually deposited via vacuum process, which is not suitable for solution processable OPVs.

GO or rGO was found to be suitable HTL by solution casting into thin films. Various groups[201, 245, 246] introduced GO as HTL to fabricate P3HT:PCBM based OPVs which exhibited PCEs of 3.5% and the devices based on high performance active layer ($PC_{71}BM$)[247-249] showed PCEs up to 7.5% (Figure 2.11a). rGO either prepared by using p-toluenesulfonyl hydrazide reductant or functionalized with sulfonic acid acted as HTL in OPVs showing PCEs of ~3.6% and 7%, respectively.[245, 250] Furthermore, GO composite hybridized with other materials such as PEDOT:PSS, CNT, and transition metal were studied as well to serve as the HTL.[251-253]

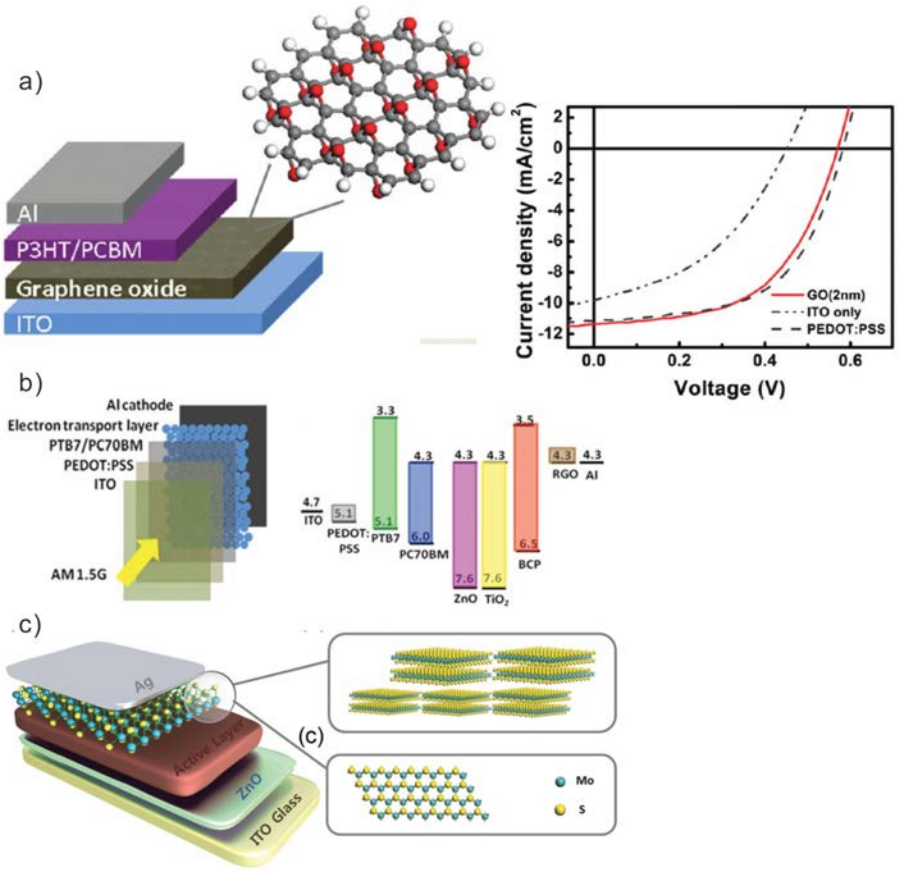

Figure 2.11. a) Scheme of as-fabricated OSCs with GO as HTLs and corresponding J-V curves.[246] b) Scheme and energy band diagram of as-

fabricated OSCs with rGO as ETL.[254] c) Scheme of as-fabricated inverted-OSCs with MoS_2 as HTL.[194]

For the ETL, GO has to be n-type doped via similar ways mentioned in Section 2.4.1. For example, Liu et al fabricated the OPVs by using GO as HTL and Cs_2CO_3-treated GO as ETL. The normal and inverted devices showed PCEs of 3.67% and 2.97%, respectively.[255] Other than the alkali salts doping, GO hybridized with other ETL oxides (e.g. ZnO, TiO_2) was synthesized for ETLs (Figure 2.11b).[254, 256] Moreover, 2D TMD nanomaterials including MoS_2 (Figure 2.11c),[83, 202, 203] NbS_2,[197] WS_2[257] and TaS_2[258] have been employed as buffer layers in OPVs.

2.4.3 Acceptors

The high electron mobility and large surface area have allowed graphene to be promising electron acceptors to replace conventionally used fullerene derivatives such as PCBM. In 2008, Liu et al. integrated the isocyanate functionalized GO acceptor and P3OT donor into OPVs, the best PCE of which is 1.4%.[259] Li et al. reported the OPV devices using functional graphene quantum dots (GQDs) as electron acceptor and P3HT as donor (Figure 2.12a).[260] In this device, the LUMO level of GQDs is estimated to be 4.2~4.4 eV, and this means that the open circuit voltage of P3HT/GQDs-based device should be around 0.8 V, which is consistent with measured results (0.77 V). Dai's group reported the synthesis of P3HT-grafted GO sheets via the esterification of CH_2OH-terminated P3HT and GO sheets and further demonstrated a bilayer photovoltaic device based on G-P3HT/C_{60}. The PCE was 200% increased up to 0.61% compared to that of P3HT/C_{60}.[261] Afterwards, they developed C_{60}-grafted graphene via a lithiation process to serve as the electron acceptor, which was blended with P3HT for fabrication of OPVs, yielding a PCE of ~1.22% (Figure 2.12b).[262] Upon incorporating 1-pyrenecarboxylic acid (PCA)-rGO electron transports layers into OPVs, the PCE was significantly improved to 2.85%.[263]

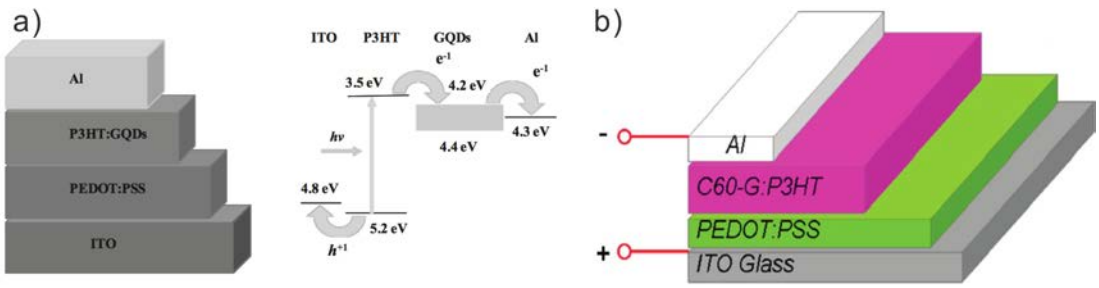

Figure 2.12. a) Scheme and energy band diagrams of photovoltaic devices with graphene quantum dots as acceptor.[260] b) Schematic illustration of photovoltaic devices with C60-G:P3HT as active layer.[262]

2.5 Conclusions and Summary of Research Gaps

Based on the literature review aforementioned, it is easy to understand the importance of 2D nanomaterials including graphene and TMD nanosheets. Their exciting and diverse properties in electronics, mechanics, and optoelectronics have attracted numerous researchers from not only the academia but also the industry and a huge of various applications has been put into practice. In terms of the preparation of 2D nanomaterials, this thesis has summarized various preparation strategies as well was their advantages and disadvantages. Although those methods show promising perspectives, the widespread implementation of graphene and 2D TMDs in semiconductor industry and other fields has not really achieved. The challenge still lies in finding a reliable way to produce 2D nanomaterials in high quality, large scale and solution-processed manners. Below are the research gaps including both the preparation and application aspects:

1. Developing a reliable method to produce high-quality and large-scale graphene nanosheets in solution-processed manners is still necessary. Since the currently developed approaches are far from satisfying the demands.
2. Graphene thin films prepared by pure graphene nanosheets suffer the higher sheet resistance. Therefore, it is quite important to figure out how to improve the conductivity, e.g. hybridization with other conductive materials
3. Beyond graphite, a plenty of other bulk-layered materials also requires a facile preparation strategy to produce 2D nanomaterials.

4. 2D nanomaterials have been intensively studied in photovoltaic applications. Graphene electrodes especially prepared from solution-processed ways bear promising prospects for large area device fabrication.
5. 2D TMDs show superior property in the substitution of conventionally used HTL PEDOT:PSS, because it is chemically stable and will not cause damage to the ITO electrode. Thus the incorporation of 2D TMD thin films into photovoltaics via solution processed manners requests further study.
6. Graphene has been functionalized by polymer brushes to offer sites for the immobilization of biomolecules. However, the electrical performance after the polymer brushes functionalization is rarely investigated.

CHAPTER 3 METHODOLOGY

In this chapter, the methodology involved for the thesis is generally introduced. First, methods used to prepare 2D nanomaterials will be elaborated. Then as proof-of-concept applications, photovoltaic devices and FET devices will be fabricated. Finally, various measurements in terms of material characterization and device performance study will be described.

3.1 Materials Preparation

3.1.1 Salt-assisted Direct Exfoliation

To overcome the drawbacks in the organic solvent-based exfoliation, such as long time sonication and low yield, we developed salt-assisted direct exfoliation method. Figure 3.1 illustrates the synthetic process, typically including four steps: (1) mixing of bulk-layered crystals with inorganic salts (NaCl or $CuCl_2$) in water; (2) boiling of the mixtures and slowly evaporating water, leading to the formation of intermediated product salt/bulk crystal composites; (3) ultrasonic exfoliation of salt/bulk crystal composites in organic solvents (N-methyl-2-pyrrolidone (NMP), or N,N-dimethylformamide (DMF)) and filtration; (4) re-dispersion into an aqueous solution, centrifugation, and extraction of the upper suspension to obtain the final 2D nanosheets in water.

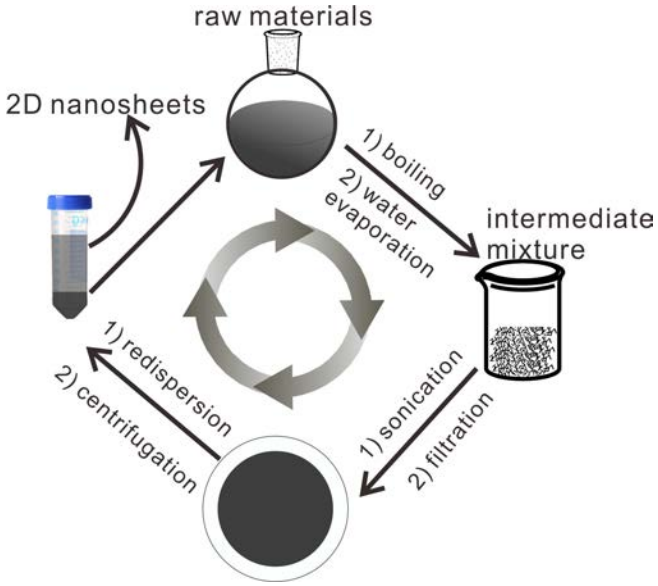

Figure 3.1. Schematic illustration of the salt-assisted exfoliation process of bulk-

layered crystals into few-layered 2D nanosheets.

3.1.2 CVD Growth of Monolayer Graphene

As introduced in Chapter 2, various approaches were developed to exfoliate bulk-layered materials into 2D nanosheets and every reported method has their own pros and cons. On balance, the choice of a proper method depends on the application designed. CVD method shows merits in the production of high-quality graphene sheets with controllable layer numbers and intact electronic structures. Therefore, in the light of the practical electronic applications, CVD method is a better choice.

Monolayer graphene film was grown on 25 μm thick Cu foils in tube furnace under high temperature (Figure 3.2b). First the air in the tube was evacuated by the vacuum pump to maintain a low pressure of 3×10^{-2} Torr. Then H_2 (10 sccm) was flowed and meanwhile the temperature was increased to 1050 ^{o}C. Cu foil would be annealed at 1050 ^{o}C for 30 min under this reducing atmosphere to remove any organic residues or oxides. Next, CH_4 (15 sccm) was introduced as the carbon feedstock to initiate the reaction for 15 min. After the reaction, CH_4 was turned off and the furnace was powered off and moved aside to allow the tube to cool down. Figure 3.2c illustrates the mechanism of graphene growth on Cu. Different from Ni, Cu has ultralow carbon solubility, and this results in a distinct growth process, i.e surface-catalyzed process instead of a segregation process. The hydrocarbon is catalytically decomposed on the Cu surface. After the deposition of the first layer graphene, Cu surface is fully covered and no catalyst is exposed to promote further decomposition of CH_4 and graphene growth. The reaction on Cu is self-limiting because growth for 1 h yields a similar structure to growth performed for 10 min.[264, 265]

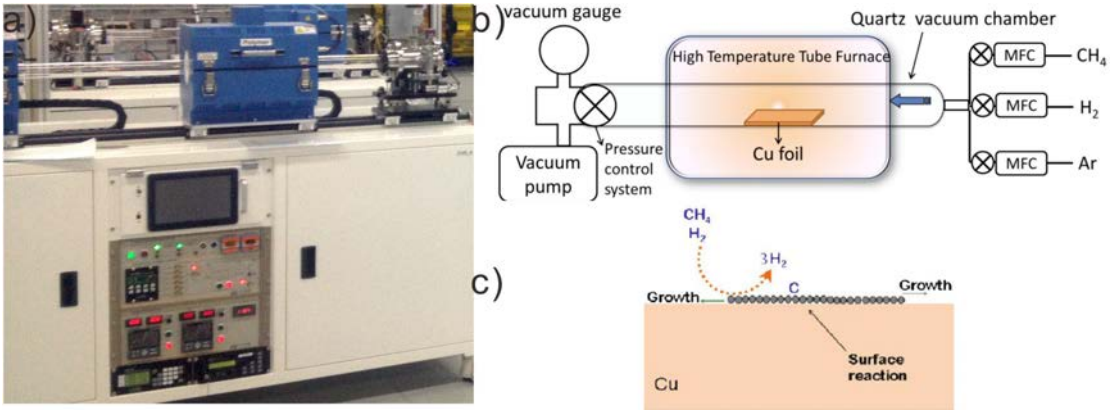

Figure 3.2. a) The equipment used for the CVD growth of graphene. b) The close-up setup for CVD growth of graphene. c) Schematic illustration of the mechanism of graphene formation.

3.2 Material Characterization

3.2.1 Optical Microscopy

The simplest function of optical microscope is designed to make fine details visible. By employing a group of lens and condensers, small objects or surface patterns can be magnified so that we can observe through the eyepiece or the CCD camera which allows the capture of digital images.

3.2.2 Transmission Electron Microscopy

TEM as an analytical tool allows the visualization and analysis of specimens in the realms of micrometer to nanometer. Compared to optical microscopy, TEM can reveal much more fine details because of using a focused beam of high-energy electrons, such as the detailed examination of crystal structure, the investigation of specimen orientations and chemical compositions. By illuminating the samples with a beam of electrons within a high vacuum, the electrons can interact with the specimen and be detected as they transmit through the sample. In our case, the sample can be simply prepared by d rop coating the nanosheets-containing solution onto the copper grid. After natural drying, the sample is ready for the measurement.

3.2.3 Scanning Electron Microscopy (SEM)

This electron microscope can produce images of the specimen by scanning it with a focused beam of electrons, which is generated from the electron source, accelerated down and passed through a combination of lenses and apertures. When the electrons hit the surface of the sample and penetrate into a depth of few microns, they interact with the sample, resulting in the emission of secondary electrons, backscattered electrons and characteristic X-rays (Figure 3.3). The most common imaging mode collects low-energy electrons (<50 eV), known as secondary electrons. They are ejected from the K-shell of the specimen atom (within a few nanometer from the sample surface) by inelastic scattering interactions with the beam electrons. The number of secondary electrons collected by the detector can directly reflect the surface topography of the sample. Backscattered electrons refer to high-energy electrons originating from the electron beam that are backscattered out of the specimen by elastic scattering interactions with specimen atoms. Owing to the discrepant backscatter ability between heavy elements (high atomic number) and light elements, backscattered electrons are responsible to detect the contrast of areas with different chemical compositions. Moreover, the characteristic X-rays can contribute to the elemental analysis of a sample by energy-dispersive X-ray spectroscopy (EDX). When the electron in the inner shell is excited and ejected from the shell, the vacancy created can be filled by the electron from the outer, and the energy difference between the inner and outer shells may be released in the form of an X-ray.

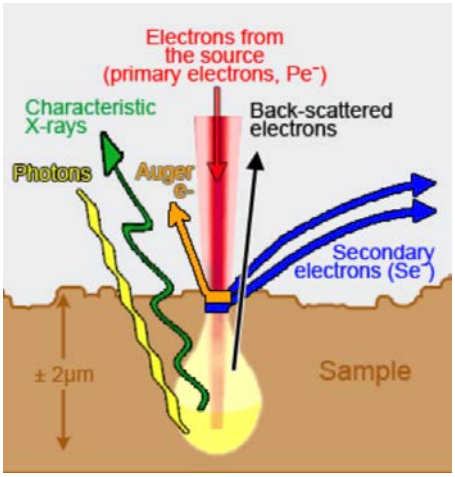

Figure 3.3. Interaction between sample and electrons in SEM measurement.

3.2.4 Atomic Force Microscopy (AFM)

An AFM uses a very sharp tip amounted on the end of a cantilever to scan over a sample surface based on the tip-surface interactions (Figure 3.4). As the tip approaches the surface, the attractive force between the tip and the surface causes the deflection of cantilever towards the surface. When the tip-surface distance is much closer, even making a contact, the increasing repulsive force will result in the cantilever to deflect away. Such a deflection of cantilever can be reflected by an optic sensor, which consists of an incident laser beam and a position-sensitive photo diode to track any change of the reflected beam. Therefore the topography of a sample can be imaged by scanning the cantilever over a region of interest. The imaging modes are classified as contact, non-contact and tapping modes based on the tip-surface interaction force. In contact mode, because the cantilever is in contact with the surface, strong repulsive force leads to the deflection as the cantilever scans across the topographical features. In non-contact mode, the cantilever oscillates just above the surface as it scans. The attractive force variation caused by the change of tip-surface distance results in the shift of the vibrating frequency, which can reflect the surface profile leaving the surface untouched. The tapping mode also scans above the surface, but with higher oscillation amplitude, which can avoid the tip trapping or any adhesion by the surface contaminant.

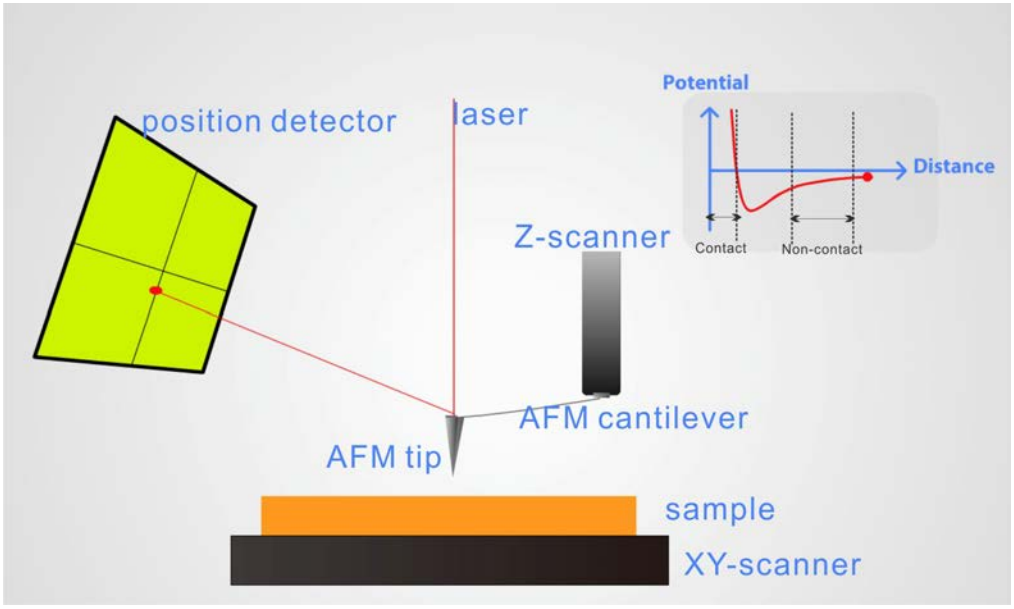

Figure 3.4. AFM working principle. Inset is the interaction of tip-sample as a function of distance.

3.2.5 X-ray Diffraction (XRD)

XRD is a powerful nondestructive technique that can rapidly characterize the crystalline materials. It provides information on structure, interatomic distance, bond angles, preferred crystal orientations and so on. X-rays are produced by bombarding a metal target (e.g. Cu) with a beam of electrons emitted from a hot filament (e.g. tungsten). The electrons in K-shell (1s) of the target atom will be ionized by the incident beam and X-rays are emitted as the resultant vacancies are filled by electrons dropping down from the 2p or 3p levels. This gives rise to Ka and Kb lines. The XRD peaks are produced by constructive interference of a monochromatic beam of x-rays scattered at specific angles from each set of lattice planes in a sample. Therefore, the XRD pattern is the fingerprint of periodic atomic arrangements in a given material.

3.2.6 Micro-Raman Spectroscopy

It is a spectroscopic technique used to measure the spectra of microscopic samples by observation of vibrational, rotational and other low-frequency modes in a system. Generally, a Raman spectrometer is integrated with a Raman microscope. Different exciting lasers can be used to excite the sample at different wavelength. The interaction between laser light and molecular vibrations, phonons and etc., results in the energy of laser photons being shifted up or down. This energy shift can give information of vibration modes and other low frequency transitions so as to identify the samples.

3.2.7 Fourier Transform Infrared Spectroscopy (FTIR)

As IR radiation passes through a sample, some of the radiation is absorbed while some of it is transmitted. The resulting spectrum represents a fingerprint of a sample with absorption peaks corresponding to the frequencies of vibrations between the atom bonds. Since each material has a unique combination of atoms, it has a unique IR spectrum, which can provide a positive identification of different kinds of materials. FTIR offers quantitative and qualitative analysis for organic and inorganic samples.

3.2.8 X-ray Photoelectron Spectroscopy (XPS)

It is a surface-sensitive quantitative spectroscopic technique that can be used to analyze the surface chemistry including the characterizations of the elemental composition at the parts per thousand level, chemical state, empirical formula and electronic state of the elements that exist within a material. Normally XPS requires high vacuum or ultra-high vacuum conditions (~10^{-8} or < 10^{-9} mbar), therefore the solid sample is favorable. During test, a beam of X-rays (200~2000 eV) is irradiated into a material and meanwhile the kinetic energy and number of electrons that escape from the very top surface (0~12 nm) of the material are measured. After analysis, XPS spectra can be acquired. Figure 3.5 shows the working principle of XPS.

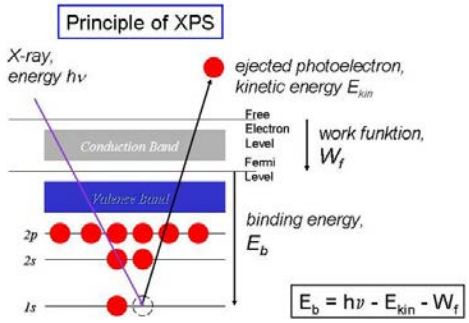

Figure 3.5. The working principle of XPS.

3.2.9 Thermo-gravimetric Analysis (TGA)

TGA is a thermal analysis method in which mass changes are measured as a function of increasing temperature or as a function of time with constant temperature. It is commonly used to determine the mass loss or gain of target specimen due to decomposition, oxidation, or loss of volatiles. By programming the furnace such as the heating rate and temperature, the mass change can be measured as a function of temperature so that we can interpret the composition of selected materials.

3.2.10 UV-Vis Spectroscopy

It refers to the absorption spectroscopy in the ultraviolet-visible spectral region by the measurement of the attenuation of a beam of light after it passing through

a sample. With two equal-intensity beams of light passing through two identical cuvettes respectively, one contains the solvent as the reference and the other contains the solvent with the dispersed compound. If the sample compound absorbs light, the transmittance can be reflected by detecting the transmitted light versus the wavelength. According to the Lambert-Beer law, $A = \alpha CL$, where A is the measured absorbance, L is the path length, C is the concentration of absorbing species and α is the known absorption coefficient, we can calculate the concentration of sample solution.

3.2.11 Four-point Probe

A four-point probe is a simple apparatus to measure the resistivity of any semiconductor materials. The setup consists of four equally spaced (1 mm) metal tips (e.g. tungsten) with finite radius (e.g. 0.5 mm). Each tip is supported by springs on the other end to minimize the sample damage during probing. By applying a current through the outer two probes and measuring the voltage across the inner two probes, it allows the determination of a sample resistivity. In our case, it is used to measure the sheet resistance of thin films.

3.3 Device Fabrication and Characterization

3.3.1 Photovoltaic Devices

Fabrication of OSCs: For a standard organic solar cell, it consists of such a structure anode/HTL/active layer/ETL/cathode (Figure 3.6a). In our case, ITO was used as the anode. First ITO glass was patterned to be bar-like with a width of 4 mm by screen printing UV-curing resist and subsequent etching in acidic solution (HCl/HNO_3 mixture). Then it was sequentially sonicated in ethanol, acetone, isopropanol and deionized water for 8 min and treated by oxygen plasma for 5 min. Then the HTL such as PEDOT:PSS aqueous solution was spin-coated at 3000 rpm for 30 s on the substrate followed by annealing at 200 ^{o}C for 30 min to form a ~40 nm thin film. The area beyond ITO pattern was erased to minimize the external effect on the effective area and meanwhile one end of PEDOT:PSS covered ITO part was also erased to expose ITO to serve as the bottom electrode. A blended P3HT and PCBM solution in chlorobenzene (P3HT 20 mg mL^{-1} and PCBM 16 mg mL^{-1}) was successively spin-coated at 700

rpm for 18 s and 1340 rpm for 7 s on PEDOT:PSS film and annealed at 145 ^{o}C for 5 min so as to remove the residual solvent and improve the crystallinity. This process was carried out in the high purity N_2-filled glovebox. Then the device was taken out of the glovebox to conduct the thermal deposition of top electrode, such as Al. Through the shadow mask, 100 nm Al (with 0.8 nm LiF or not) was deposited. The effective area of each device depends on the overlapped region between the top and bottom electrodes. A post-annealing process (135 ^{o}C) was also necessary, the purpose of which was to remove the oxygen in the active layer and make the contact between active layer and top electrode more compact. As to the encapsulation, it depends on the characterization atmosphere. If not performed in the glovebox, the device should be encapsulated, in our case, by glass cap and epoxy glue in the glovebox. After 2 h solidification, the device was ready for the characterization.

Fabrication of Perovskite Solar Cells: Figure 3.6b shows the device structure. First, FTO glass was pre-cleaned and treated by plasma for 5 min. Then a compact ETL such as TiO_2, and ZnO was deposited on the substrate. TiO_2 was prepared via a low-temperature processing method,[266] by spin-coating tetrabutyl titanate isopropanol solution (concentration 3 vol%) at 5000 rpm for 30 s and thermal annealing at 90 ^{o}C for 60 min in the ambient atmosphere. Then the perovskite layer was deposited by a two-step method. PbI_2 dissolved in DMF with a concentration of 460 mg mL^{-1} and MAI dissolved in isopropanol with a concentration of 10 mg mL^{-1} were sequentially spin-coated at 3000 rpm for 15 s and 30 s, respectively. After thermal annealing at 100 ^{o}C for 30 min, a HTL of 2,2',7,7'-tetrakis-(N,N-di-p-methoxypheny lamine)-9,9-spirobifluorene (spiro-OMeTAD) was spin-coated at 5000 rpm and then placed in desiccator (humidity <10%) overnight. The spiro-OMeTAD solution was prepared by adding 70 mg spiro-OMeTAD into 1 mL chlorobenzene with additives of 25 µL Li-bis(trifluoro-methanesulfonyl)imide (Li-TFSI) solution (520 mg mL^{-1}, dissolved in acetonitrile) and 36 µL 4-tert-butylpyridine (tBP). Finally, Ag electrode (100 nm) was deposited by thermal evaporation.

Device Characterization: Current-voltage characteristic curves were measured by keithley 2400 source meter under 1 sun illumination (AM 1.5 G condition,

equal to 100 mW cm^{-2} irradiance), which was fulfilled by a solar simulator (Newport 91160, 150 W). The intensity of the simulator was calibrated by a standard silicon solar cell.

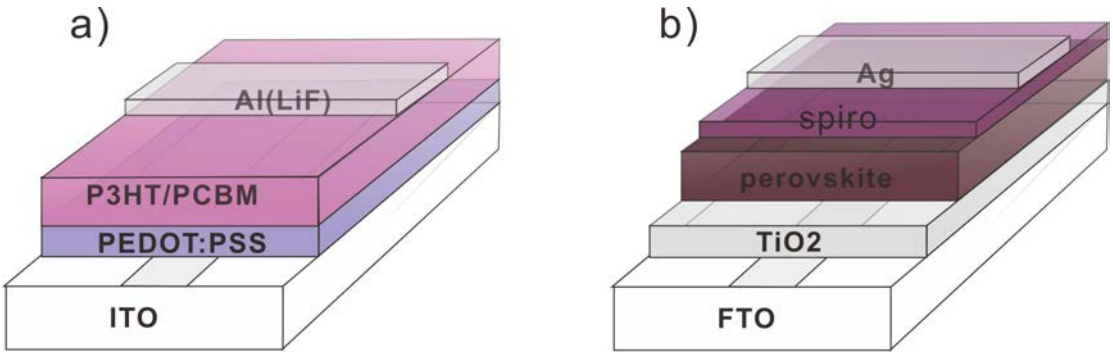

Figure 3.6. Schematic illustration of photovoltaic devices: a) OSCs, b) perovskite solar cells.

3.3.2 FET devices

Fabrication of Pre-patterned Electrode: Figure 3.7 shows the fabrication procedures for preparing the pre-patterned gold electrodes. 4-inch SiO_2/Si wafer was cleaned by piranha solution. Negative photoresist (AZ nLOF 2305) was spin-coated on the substrate at 3500 rpm for 30s and then baked at 110 ^oC for 2 min. Then the substrate was exposed to the UV light for seconds using the photo mask. After the post-bake at 120 ^oC for 2 min, the developer (AZ 300MIF) was used to remove the unexposed photoresist, and the metal (Au/Cr) was deposited by E-beam evaporation. Finally, the lift-off was conducted by using acetone so as to obtain the required patterned electrodes.

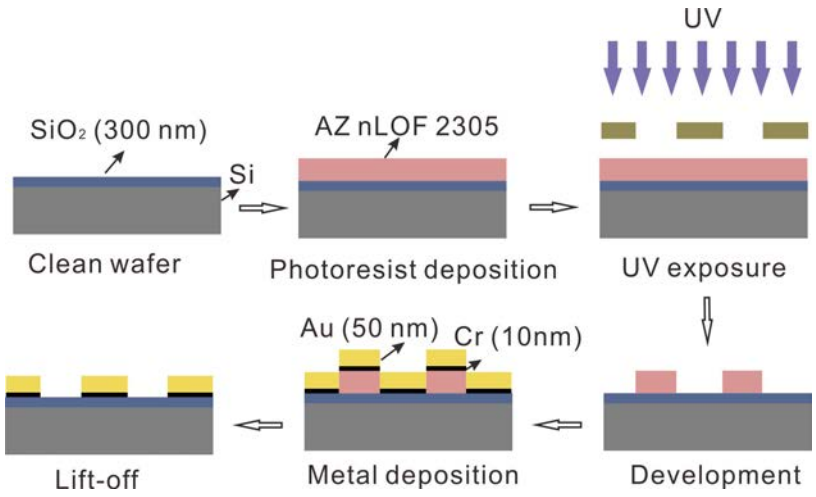

Figure 3.7. The fabrication procedures of pre-patterned electrode by photolithography.

Fabrication of Graphene FET: First, graphene was wet transferred onto the substrate with pre-patterned electrodes. Then a similar photolithography process was repeated by using positive photoresist (AZ5214E), which was spin-coated at 4000 rpm for 30s and baked at 105 ^{o}C for 90 s. After the alignment, UV-exposure and lift-off, O_2 plasma was applied to remove the unprotected graphene and the photoresist was got rid of by immersing into acetone. Graphene FET was prepared with specific channel length and width. Figure 3.8 shows the optical images of graphene films after photolithography, plasma treatment and removal of photoresist, respectively.

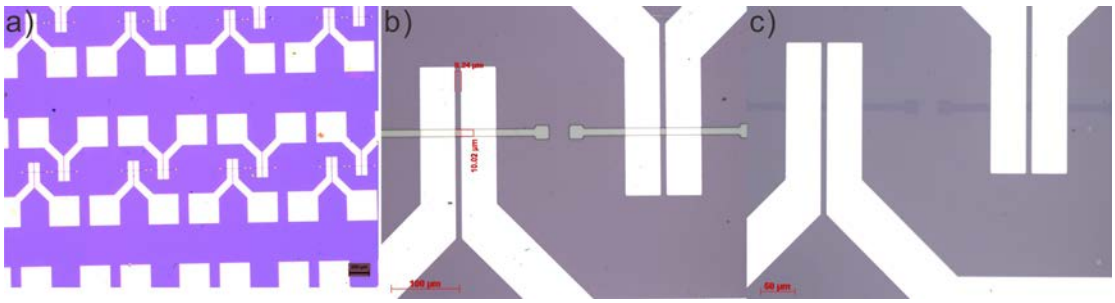

Figure 3.8. Optical images of graphene films after photolithography a), plasma treatment b) and removal of photoresist c), respectively.

Device Characterization: The bottom-gate graphene FET devices were measured by a keithley 4200 semiconductor characterization system under ambient or vacuum conditions.

CHAPTER 4 SALT-ASSISTED DIRECT EXFOLIATION OF GRAPHITE INTO SINGLE- AND FEW-LAYERED GRAPHENE

In this chapter, the salt-assisted direct exfoliation method is first proposed to demonstrate that graphite can be successfully exfoliated into single- and few-layered graphene nanosheets. Factors that can affect the production process, such as various salts, organic solvents and so on are carefully investigated. Graphene thin films are also prepared by solution-processable deposition techniques.

4.1 Introduction

Graphene, a two dimensional (2D) atomic layer of sp^2-hybridized carbon atoms and the newest member of the carbon family, has attracted enormous attention because of its unique electronic, optical, mechanical, and thermal properties.[2, 13, 181, 189, 267-281] One key priority of the research front is the development of synthetic approaches that allow cost-effective mass-production of large-size and high-quality graphene sheets. Early methods such as mechanical exfoliation and epitaxial growth produce high quality graphene but the throughputs are too low for any practical application.[282, 283] Chemical vapor deposition (CVD) is capable of producing large-area graphene sheets, which could provide a very low sheet resistance of 125 Ω/□ with 97.4% optical transmittance.[41] CVD, however, typically involves high temperature procedures and expensive equipment and substrates, which make the approach less cost-effective. The need to transfer graphene sheets from growing substrates of CVD to target substrates further hampers its economic viability for many applications.[284, 285] On the other hand, chemical exfoliation from graphite based on the synthesis of graphene oxide (GO) and subsequent thermal[13] or chemical[65] reduction into reduced graphene oxide (rGO) has attracted much attention due to the advantages of low cost and solution-processing compatibility. Nevertheless, rGO suffers inevitably from a large amount of oxygen-containing defects which degrade its performance dramatically.[76] Therefore, graphene thin films fabricated based on rGO give a relative higher sheet resistance, being 10^3~10^5 Ω/□ at 60~80% transparency.[286-

288], [193], [192] Recently, there have been reports of electrochemical processes being used to exfoliate graphite.[106, 111, 113, 289] In particular, Su et al. reported the direct electrochemical exfoliation of graphite into large-size few-layer graphene sheets (with edge lengths as large as 30 μm) in diluted sulfuric acid.[106] Wang et al. electrochemically expanded graphite with Li complex, and exfoliated the expanded graphite in a Li^+ organic solution to produce few-layer graphene sheets (edge lengths 0.5-3.0 μm).[289] However, the voltage applied (10 V) and sulfuric acid used in the former electrochemical process partially oxides the as-made graphene and further efforts have to be made to reduce or avoid the oxidation, whilst the latter process requires expensive organic compounds and long ultrasonication times (48 h) with high intensity ultrasound (~100 W/cm^2). More recently, several attempts have been made to directly exfoliate graphite into few-layer graphene sheets by (1) long time sonication of graphite in organic solvents,[73, 76, 282] ionic liquids,[101, 290] or water-surfactant solutions,[85, 86, 90, 291] and (2) sonication of graphite intercalation compounds (GICs).[292-295] The area of graphene flakes produced by methods (1) and (2), however, is typically less than 1 μm^2, which is too small for applications in many devices[264] or composites.[296, 297] For example, the fabrication of aerogels requires giant graphene sheets to construct the cell walls of the 3D framework.[298] Graphene thin films made from the liquid phase ultrasonic exfoliation method showed the sheet resistance 10^3 ~ 10^5 Ω/□ with transmittance 40% ~ 85%,[291] the performance of which is comparable to that of rGO films.

Herein, a new method, namely “salt-assisted direct exfoliation of graphite”, was reported. This method can directly exfoliate graphite powders into large-size, high-quality, and aqueous dispersible few-layer graphene sheets without the use of any oxidant, high energy source, or long time sonication. In this method, graphite powders are immersed in an inorganic salt containing aqueous solution, and salt ions are allowed to enter, precipitate or crystallize within the inner layer spaces of graphite as the solution becomes supersaturate upon water evaporation, which leads to a dramatic expansion of the layer spacings of graphite. The expanded graphite is then exfoliated into few-layer graphene sheets by low power ultrasonication in an orthogonal solvent of the salt. Importantly, because the process does not involve any high-energy activation or oxidizing reagent, the

as-made graphene contains very little oxygen. We demonstrate that 86% of the as-made graphene sheets are 1-5 layers and their sizes are typically 5-200 μm^2. Compared with literature works that exfoliate graphite without salts, the time required for exfoliation in our method is one hundred times shorter, and the resulted graphene size is ten to one hundred times larger. Most of the reagents can be readily separated and recycled for further synthesis. The as-made few-layereded graphene sheets can be fabricated into conductive thin films via a vacuum filtration method.

4.2 Experimental

4.2.1 Preparation of Graphene

Graphite (100 mg, 325 mesh, Alfa Aesar), (SDBS, 2 g, Sigma-Aldrich) and inorganic salts (NaCl or $CuCl_2$, 2 g, Sigma-Aldrich) were added into 100 mL deionized (DI) water. The mixture was stirred at 350 rpm for 48 h at 100 ^oC and then the water was removed by evaporation. The resulting residue was added into 100 mL organic solvent (N,N-Dimethylformamide (DMF), ethanol (EtOH), N-methyl-2-pyrrolidone (NMP), or toluene) and ultrasonicated for 2~3 h, followed by vacuum filtration and washing three times with 100 mL DI water to remove the excess salt and SDBS. The filtered residue was redispersed in DI water to form a 5 mg mL^{-1} aqueous solution, which was centrifuged at 3000 rpm for ~5 min. The upper solution was collected as the graphene solution for characterization.

4.2.2 Thermal Annealing

Graphene aqueous solution after centrifugation was cast onto a clean SiO_2/Si wafer. The sample was dried at 80 ^oC under vacuum for 12 h and then heated to 500 ^oC for 1 h in an argon atmosphere. Finally, the sample was cooled down to room temperature in the argon atmosphere.

4.2.3 Fabrication of Graphene Films

The as-prepared graphene aqueous solution was vacuum-filtrated through a cellulose ester membrane (Millipore, pore size of 0.025 μm, diameter of 47 mm).

The as-made graphene/membrane was pressed against an isopropanol-cleaned glass substrate. After annealing in an acetone vapor for 12 h, the membrane was removed by immersing in an acetone bath. The resultant graphene/glass was finally rinsed with methanol.[291]

4.2.4 Characterization

SEM was performed using a JEOL Model JSM-6490. TEM was performed using a JEM-2010 (JEOL) with an accelerating voltage of 120 kV. AFM (XE-100, Park Systems) was used to characterize the as-prepared graphene sheets. Absorption of the as-prepared graphene aqueous solution was measured by using a UV-Vis spectrometer with quartz cuvettes (Perkin-Elmer Lambda 18). Transmittance spectra of the as-prepared graphene thin films were collected by UV-Vis spectrometer. TGA was conducted on a TGA-Q5000 apparatus with a heating rate of 5 ^{o}C/min under N_2. XPS of samples were characterized by a PHI 1600 spectrometer. Raman spectra were collected using a Raman spectrometer (Renishaw microprobe RM 1000) with a 633 nm laser. X-ray diffraction (XRD) was carried out using a Buker D8-Advance X-ray powder diffractometer with Cu Kα radiation (λ = 1.5418 Å).

4.3 Results and Discussion

4.3.1 NaCl-assisted Exfoliation of Graphite in Ethanol

As proof of concept, we first analyzed the as-made graphene synthesized with NaCl and EtOH as the salt and organic solvent, respectively. Figure 1a shows the as-made graphene aqueous solution. The solution was very stable and no precipitation was observed even after storing the solution in the laboratory for 15 days (Figure 4.1a). According to the Lambert-Beer law ($A = \alpha CL$), where the absorption A of the solution equals to the product of the absorption coefficient α (1390 $mL \cdot mg^{-1} \cdot m^{-1}$ for aqueous graphene solutions[85, 90]), the cell length L, and the concentration C, the concentration of the as-made graphene solution can be determined by its UV-vis absorption (Figure 4.1b). Therefore, the concentration of the graphene solution is determined to be 0.11 mg mL^{-1}.

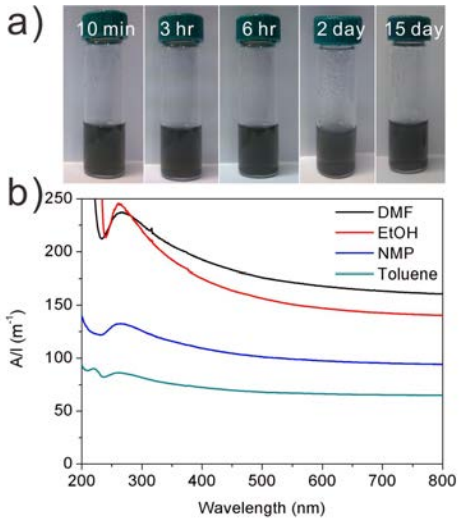

Figure 4.1. a) Digital images of the as-made graphene solution after storing for different time. b) UV-Vis spectra of graphene aqueous solutions prepared by NaCl-assisted exfoliation of graphite in various organic solvents.

The graphene solution was then dropped onto Si substrates and Cu grids for SEM and TEM studies. Typical two-dimensional sheet-like structures were observed by TEM (Figure 4.2a). The hexagonal electron diffraction pattern of the TEM image indicates that the as-made graphene is highly crystalline. By observing the folded edges of the graphene sheets with high resolution TEM, we found that the sample mostly contains single-layer, bilayer, and few-layer structures (Figure 4.2b-d). Importantly, the layer spacings within these structures are ~0.34 nm, which is equal to the layer spacing of graphite. These results indicate that our exfoliation process does not oxidize the product. Indeed, X-ray photoelectron spectroscopy (XPS) confirms that the as-made graphene has a high C 1s peak and an extremely low O 1s peak (0.05%, Figure 4.3a), which is almost identical to that of the raw graphite. Detail analysis of the C 1s peak through narrow scan and peak decomposition is shown in Figure 4.3b. The decomposed C-C peak of graphene located at 284.6 eV is almost identical to that of the graphite sample. Small C-O decomposition peaks are found at 286.6 eV for both graphene and graphite. The C-O to C-C ratios is 0.15 and 0.11 for graphene and graphite, respectively. A small peak at ~154 eV of the XPS survey is attributed to the S atoms of the physisorbed SDBS on graphene surfaces. Since most of the SDBS was washed away in rinsing steps, the amount of SDBS is estimated to be only ~1 wt% by thermo-gravimetric analysis (Figure 4.3c) through calculating

the weight loss at 460 ^{o}C.[299, 300] Previous work by Coleman et al.[86] also showed similar low oxygen content in the XPS measurement on their graphene nanoflakes which were exfoliated in a SDBS aqueous solution. Therefore, we believe that it is reasonable to obtain low oxygen contents for our non-oxidized graphene sheets.

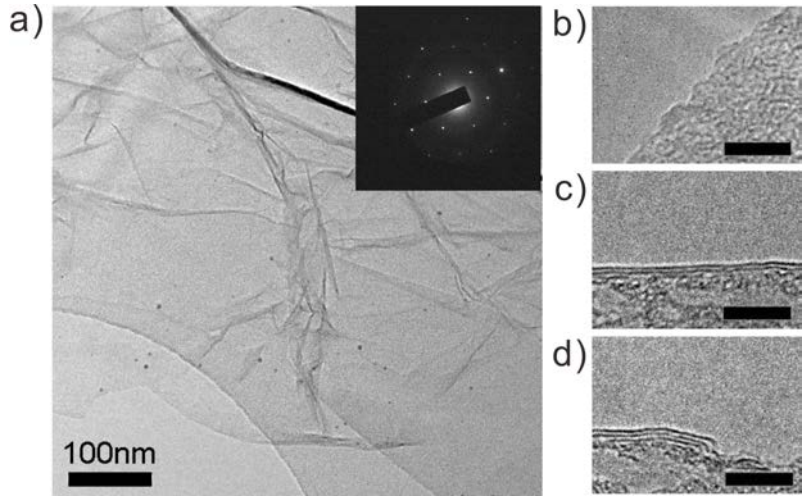

Figure 4.2. a) Typical TEM image of graphene sheets, the inset is its selected area electron diffraction (SAED) pattern; (b-d) High resolution TEM images of single layer b), bilayer c), and trilayer d) graphene sheets, the scale bars are 5 nm.

We also undertook Raman spectroscopy to analyze the quality of as-made graphene. The Raman spectra of graphite and graphene illustrate three signature bands: the D band at ~1330 cm^{-1}, the G band at ~1580 cm^{-1}, and the 2D (or G') band at ~2650 cm^{-1} (Figure 4.3d).[301] Exfoliation of the graphite into graphene is demonstrated from the change in the shape and position of the 2D band. Graphite has an asymmetric 2D band with a peak at around 2687 cm^{-1}. As the material is exfoliated the peak position shifts to lower wavenumber and becomes more symmetric. As shown by the spectra of the original graphite and representative individual exfoliated flakes (Figure 4.3d), there is a significant change in the appearance of the 2D band between the graphite and few-layer, trilayer and bilayer graphene. For example, the 2D peak position for the graphite is 2687 cm^{-1} where it is at 2665 cm^{-1} for the bilayer graphene. Typically, the D band indicates the presence of defects and the intensity ratio of I_D/I_G evaluates the level of defects.[76] The presence of the defects in the graphene arises from the intrinsic

defects in the graphite raw material and the sp^3 hybridized carbon atoms at the edges after exfoliation. The value I_D/I_G for the original graphite is ~0.1 and this appears to increase to around 0.8 for the bilayer material. The observed D band of graphene can be attributed to the presence of basal plane defects and the formation of new flake edges during sonication (Figure 4.4b). The values of I_D/I_G for the graphene in Figure 3d are lower than those for rGO[121] and are similar to the values of non-oxidized graphene samples obtained via direct exfoliation of graphite in solvents.[76, 90], [302] X-ray diffraction (XRD) measurements were carried out (Figure 4.3e). The XRD spectrum of our graphene sheets shows a broad peak centered at ~25°, which is a typical value for few-layer graphene sheets. No NaCl or $CuCl_2$ signal is observed because the salts can be readily removed by water rinsing. These XPS, Raman and XRD characterizations reveal that the quality of our as-made graphene is among the best reported in the literatures using solution methods.

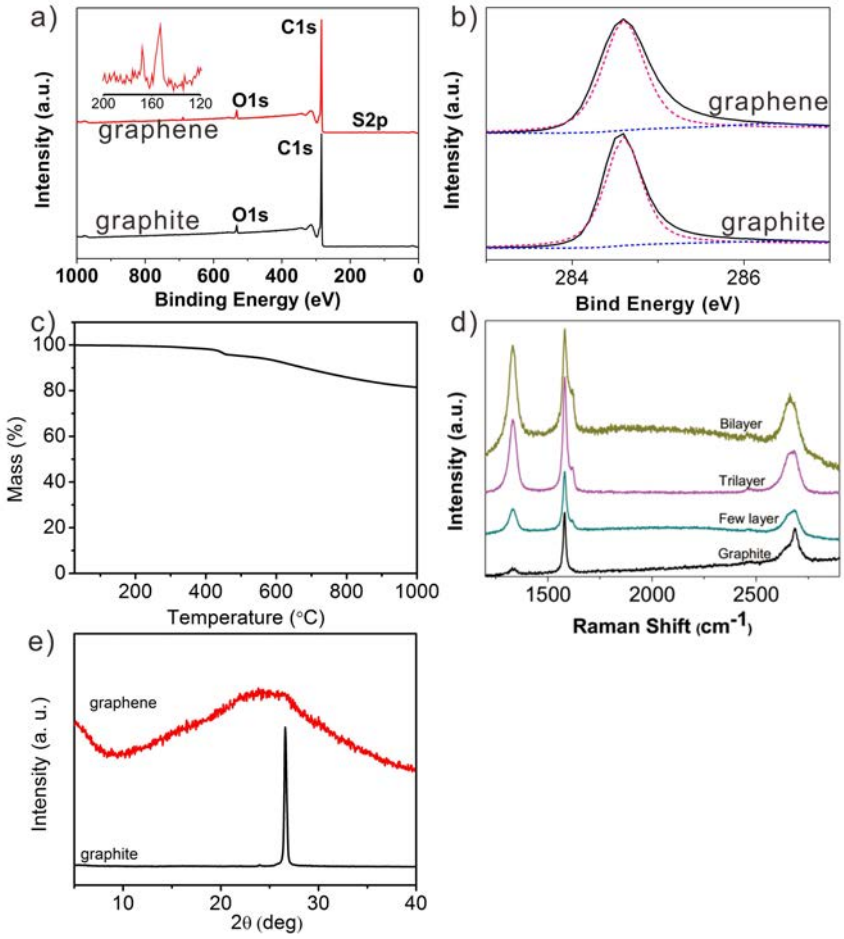

Figure 4.3. a) XPS survey, b) XPS narrow scan, and c) TGA analysis of graphene sheets, heated from room temperature to 1000 °C at 5 °C/min under

nitrogen flow. d) Raman spectra of graphite and representative flakes of the as-made graphene from NaCl-assisted exfoliation of graphite in EtOH, e) XRD spectra of as-made graphene and graphite.

In order to obtain statistical information upon the size and thickness of the as-made graphene sheets, large-area AFM scans of the samples were carried out on SiO_2 substrates (Figure 4.4a). Very importantly, the area of the graphene sheets is typically 5~100 μm^2, and can be as large as 210 μm^2 (Figure 4.4c). The edge length of the graphene sheets is typically 1 to 30 μm. The thickness of the graphene sheets is less than 5 nm for all the measured samples, and 86% of the product is thinner than 3.5 nm (Figure 4.4d). Compared with the size of pristine graphite powders observed with SEM (Figure 4.4e), the exfoliation process does not significantly break graphite into smaller pieces and is therefore an efficient method to synthesize large-size graphene sheets. In the literatures, single-layer graphene sheets with a thickness of 1.5 ± 0.5 nm measured by tapping mode AFM have been widely reported.[1, 303, 304] This thickening phenomenon (a single layer of carbon atom is ~0.34 nm) in the AFM measurement can be majorly explained as a result of the tip-graphene electrostatic force and the presence of the physisorbed water and surfactant molecules on graphene surfaces.[67, 305, 306] Indeed, significant levels of surface contamination have been reported on graphene sheets as observed using TEM.[307] Taking into account the single-layer, bilayer, and few-layer structures observed frequently by TEM and the presence of SDBS on our graphene samples, approximately 100% of the product is few-layer graphene and 86% of it contains 1-5 layers. Even though these samples were annealed in argon atmosphere at 500 ^oC for 1 h, large-size graphene sheets do not disappear as shown in AFM (Figure 4.4f), indicating that they are indeed graphene but not organic residues (SDBS was decomposed at 460 ^oC).

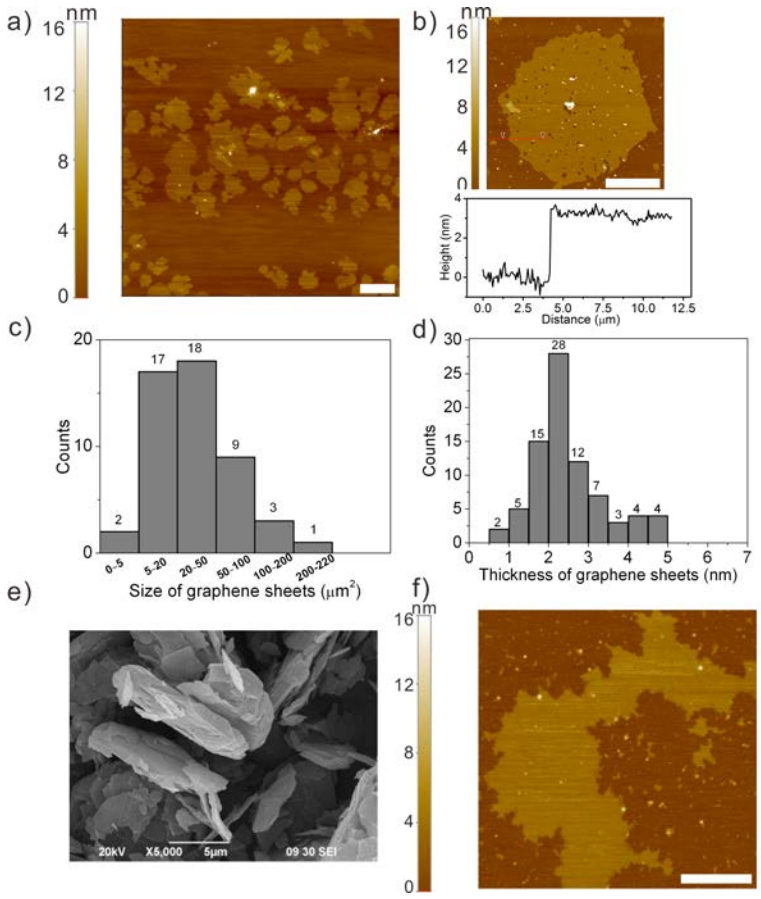

Figure 4.4. AFM topographic images of a) graphene sheets and b) a typical graphene sheet of ~3.5 nm thick with edge size ca. 30 μm, scale bars: 10 μm, c) size distribution and d) thickness distribution of as-made graphene sheets. e) SEM image of pristine graphite. f) AFM image of graphene sheet after annealing at 500 ^{o}C in argon atmosphere for 1 h, scale bar 2 μm.

4.3.2 Exfoliation of Graphite by Other Salts and Organic Solvents

Not limited to the success in the direct exfoliation of NaCl-assisted graphite with EtOH, other organic solvents such as DMF, NMP and toluene (Figure 4.1b and 4.5), and other inorganic salts such as $CuCl_2$ are also suitable for the present exfoliation process. The concentrations and sizes of graphene sheets synthesized by our salt-assisted exfoliation method using different solvents and salts are summarized in Table 4.1. The graphene sheets with thicknesses of 2~5 nm and edge sizes of 2 μm to 20 μm are typically observed by AFM and TEM (Figure 4.5c and 4.5e-h).

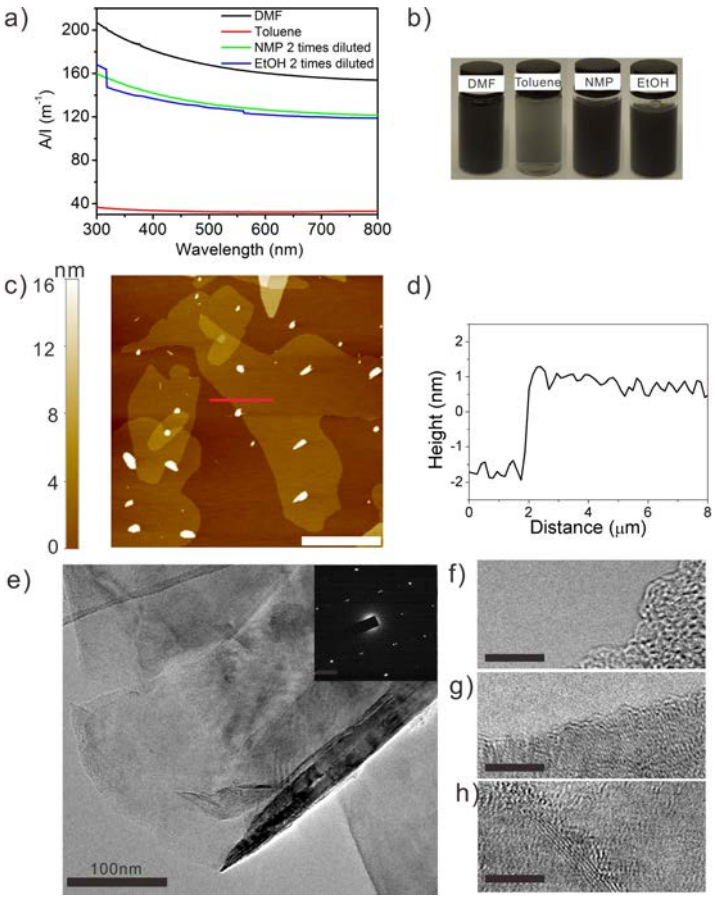

Figure 4.5. a) UV-Vis spectra and b) digital image of the graphene aqueous solution prepared from $CuCl_2$-assisted direct exfoliation of graphite in various organic solvents. c) AFM topographic image of graphene, scale bar: 10 μm. d) Cross-sectional profile analysis of the marked red line in c). e) TEM image of graphene sheets. Inset is the electron diffraction pattern. (f-h) HRTEM images of f) single-layer, g) bi-layer and h) multi-layer graphene. The scale bars are 5 nm.

Again, graphene sheets can still be clearly observed by optical microscope and AFM after annealing in an argon atmosphere at 500 ^{o}C for 1 h (Figure 4.6). Compared with the literatures where graphite was directly exfoliated into graphene sheets through long time ultrasonication in various SDBS aqueous solutions or various organic solvents (without the use of any inorganic salt),[76, 85, 86, 90, 282] our salt-assisted exfoliation method is much more superior not only in the high exfoliation efficiency in terms of low-power and shorter time of sonication, but also producing graphene sheets that are 5~10 folds larger in terms of average size.

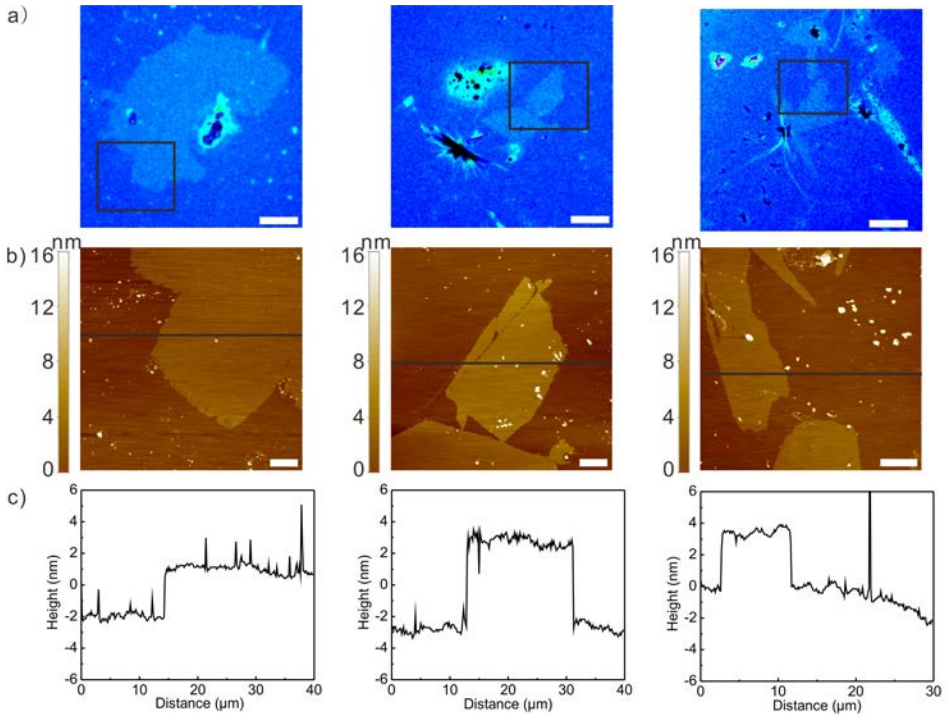

Figure 4.6. a) Optical micrographs, b) AFM topographic images, and c) cross-sectional profiles of the as-made graphene prepared by $CuCl_2$-assisted direct exfoliation of graphite in ethanol after annealing at 500 ^oC in argon atmosphere for 1 h. The scale bars are 20 μm and 5 μm for a) and b), respectively.

4.3.3 Effect of Boiling Time on Exfoliation of Graphite

Importantly, we found that the yield of the synthesis increased as the boiling time increased. As shown in Figure 4.7a, the concentration of graphene solution prepared from NaCl-assisted exfoliation monotonically increases from 0.11 mg mL^{-1} to 1.04 mg mL^{-1} as the boiling time increases from 1 day to 7 days. Similarly, for the graphene solution obtained from $CuCl_2$-assisted exfoliation, the concentration increases from 0.04 mg mL^{-1} to 0.56 mg mL^{-1} as the increase of boiling time from 0.5 day to 10 days. As control experiments, we synthesized graphene sheets following the same experimental procedures, yet without using inorganic salts. We found that the size of graphene sheets made without the use of inorganic salts was typically less than 1 μm^2 (Figure 4.7b). The concentration of the nanosized graphene solution was ~0.05 mg mL^{-1}, no matter how long the boiling time was. These findings indicate that the presence of inorganic salts during boiling significantly increases the exfoliation efficiency (higher concentration, much larger graphene sizes).

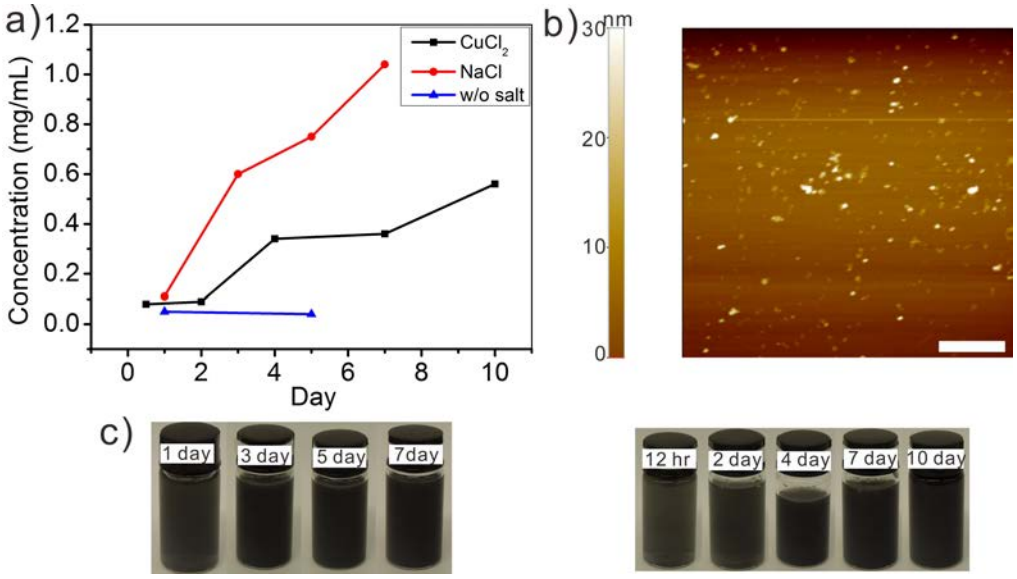

Figure 4.7. a) Concentrations of as-produced graphene aqueous solution dependent on various boiling time. b) AFM image of graphene sheets prepared w/o salts, scale bar: 2 μm. c) The corresponding image of graphene solution in a) prepared by NaCl (left) or $CuCl_2$ (right) assisted exfoliation of graphite in NMP.

4.3.4 Mechanism Study of Salt-assisted Exfoliation Process

In order to have a deep understanding of the mechanism, which leads to the effective exfoliation, we carried out further measurements to the crucial step-the intermediate mixture. In Figure 4.8a, we proposed a likelihood of exfoliation process upon the boiling and water evaporation procedures: salt ions may penetrate into the interlayer of graphite driven by the thermal or dynamic forces generated during the boiling process; salt ions could be crystallized again upon water evaporation, which may broaden the interlayer spacing and attenuate the van der Waals force, resulting in the facile exfoliation. TEM was carried out to measure the morphology of nanosheets. We can observe black particles in Figure 4b and c, which are absorbed on the surface or possibly penetrate into the interlayers. EDX analysis has assigned the black particles to be salts (e.g. $CuCl_2$ in Figure 4d) or salt aggregates together with little amount of SDBS. XRD was performed to identify whether the crystallization occurs or not. The intermediate products boiled for various days were prepared and measured. No obvious new peak can be identified and attributed to the crystallization of salts. This indicates that the crystallization does not necessarily happen. Therefore, we may conclude here that the salt ions play an important role to assist the exfoliation process.

Moreover, the salts selected for the exfoliation process should follow some basic rules: first, the salt should be strong electrolyte, which can be completely dissociated in aqueous solution; second, the diameter of salt ions should be less than 0.3 nm, which is the spacing between the interlayers. Here we chose three types of commonly used salts (NaCl, $CuCl_2$ and $FeCl_3$), the cations of which bears various charges, e.g. +1, +2, and +3. For $FeCl_3$-assisted exfoliation process, no results are reported in this thesis, because the final products precipitate after centrifugation. The may be interpreted by the strong shielding effect Fe^3 that prevents the attachment of surfactants onto graphene surfaces, which are used to stabilize 2D sheets.

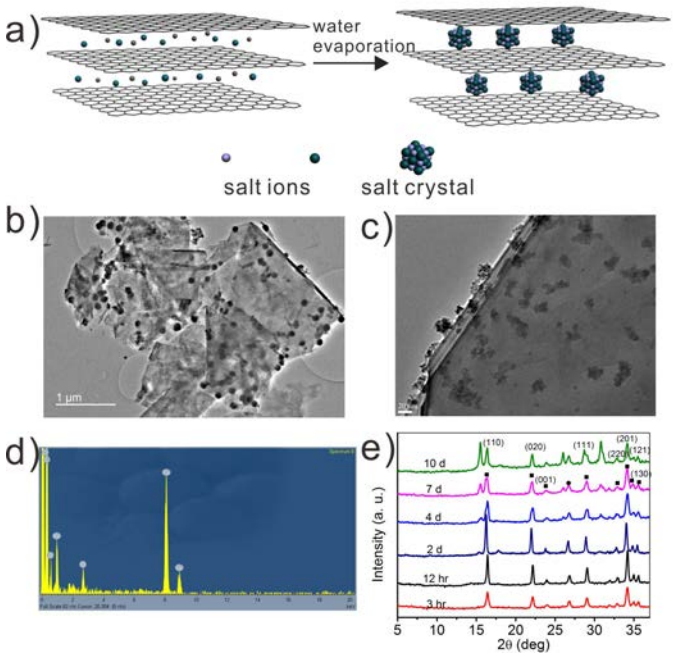

Figure 4.8. a) Proposed exfoliation process upon boiling and water evaporation. b) TEM images of the intermediate mixture using $CuCl_2$. c) HR-TEM image of the intermediate mixture. d) EDX spectrum corresponding to the black particles in b). e) XRD spectra of intermediate product by using $CuCl_2$ after boiling for different time.

4.3.5 Solution-processable Fabrication of Graphene Thin Films

Since the graphene sheets are dispersible in aqueous solution, they are promising materials for making transparent conductive electrodes by solution deposition techniques. As proof-of-concept, we fabricated thin films of the graphene sheets by a vacuum filtration method. In a typical experiment, 1 mL of the graphene aqueous solution was vacuum-filtrated through a cellulose ester membrane.

Subsequently, the graphene side of the membrane was pressed firmly against an isopropanol-cleaned glass substrate. After annealing the assembly in an acetone vapor for 2 h, the filter membrane was removed by dissolving in liquid acetone for 2 h. As such, a graphene thin film is formed on the glass substrate. Notably, the residual SDBS absorbed on graphene sheets may lower the conductivity of the as-prepared graphene film.[291] Therefore, the graphene film on glass was annealed at 500 ^{o}C under argon atmosphere for 1 h because the SDBS decomposed at 460 ^{o}C. By controlling the concentration of the graphene solution, i.e., by controlling the amount of graphene sheets, graphene thin films with different thickness from 24 nm to 250 nm were fabricated. The optical and electrical performances of the as-made graphene thin films were measured by UV-Vis spectroscopy and a four-point probe method, respectively. The transmittance decreases from 85.9% to 32.7% as the film thickness increases from 24 nm to 250 nm (Figure 4.9a). Meanwhile, the sheet resistance decreases dramatically from 2×10^{5} Ω/□ to 1×10^{3} Ω/□ (Figure 4.9b). Importantly, we find that our graphene thin films are much rougher than those reported in the literature, in which small size graphene sheets with 0.5-2 μm edge length were used for film casting. The roughness increases from 18 nm to 67 nm as the film thickens from 24 nm to 250 nm (Figure 4.9c), which is 2~5 folds larger than films with similar thinness in the literature. We believe that such a rough morphology arises from the fact that our graphene sheets are very large in size: during vacuum filtration, these large graphene sheets are difficult to form densely packed thin films compared with small-size graphene sheets. This rough morphology explains why our thin films are more optically transparent compared with those reported in the literature using small-size graphene sheets. For example, 85.9% at 24 nm and 32.7% at 250 nm are achieved. On the other hand, such a rough morphology leads to an increase in sheet resistance for graphene films with medium optical transmittance (40-80%). For example, a 10-fold increase in sheet resistance is found (28.9 kΩ/□with 67.3% transmittance) compared with those reported by Coleman et al. (3 kΩ/□ with ~70% transmittance). We are currently working on tuning the thin film morphology with different filtration procedures and casting methods, e.g., Langmuir-Blodgett coating method.[308] We also believe that this unique morphology of graphene

thin films may have important applications in composites and stretchable conductors.

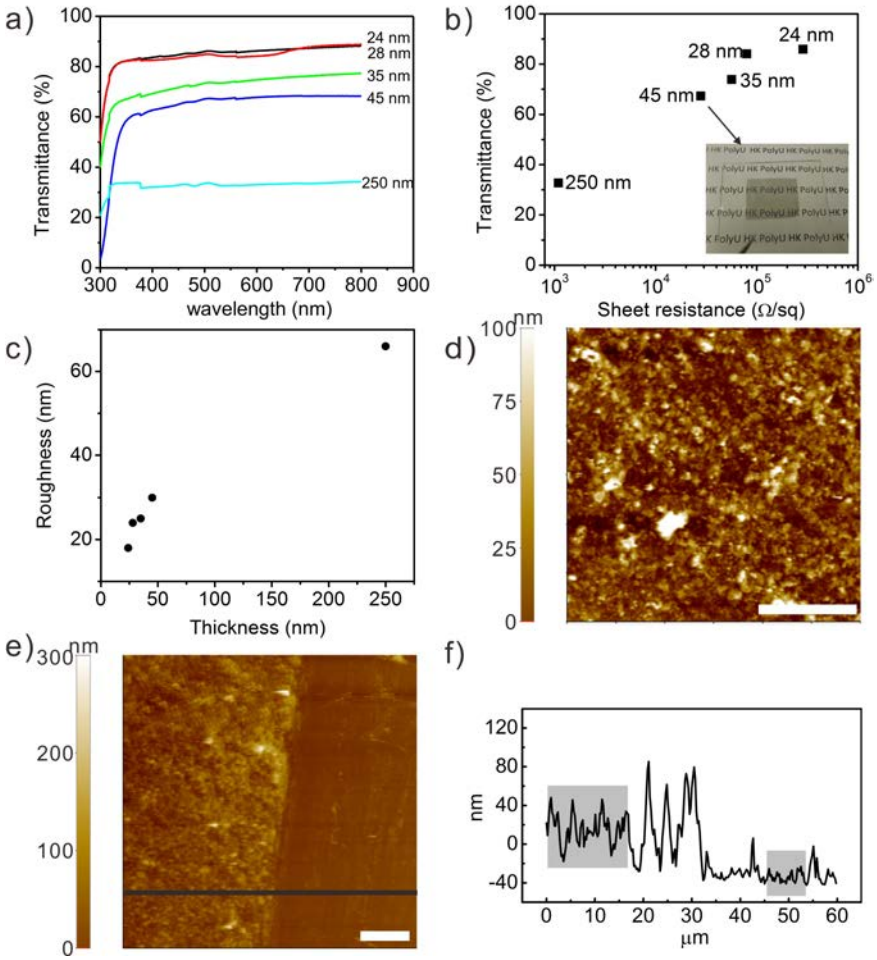

Figure 4.9. a) UV-vis transmittance of graphene thin films of various thicknesses. b) Transmittance of graphene films plotted as a function of sheet resistance, inset: digital image of the graphene thin film with 45 nm thickness on the glass substrate. c) The thickness of graphene films versus their roughness. The graphene was prepared by salt-assisted exfoliation method using NaCl and EtOH. d) AFM topographic image of the 45 nm thick graphene film, roughness (R_q)=30 nm. e) AFM topography image of the scratched edge of the 45 nm graphene film. f) The height profile of the marked line in e). The scale bars are 10 µm.

Table 4.1 Summary of the results of graphene sheets synthesized by the salt-assisted exfoliation method using different salts and organic solvents.

salt	NaCl				$CuCl_2$			
solvent	EtOH	DMF	NMP	Toluene	EtOH	DMF	NMP	Toluene
graphene con. (mg mL^{-1})	0.11	0.12	0.07	0.05	0.17	0.11	0.17	0.02
edge size (μm)	1~30	5~18	1~15	5~16	1-60	2~25	2~22	5~10

4.4 Conclusions

To sum up, we have reported a low-cost, environmental-friendly, and oxidation-free method to directly exfoliate graphite powders into large-size, high-quality, few-layer graphene sheets. The key innovation is that inorganic salts are used to expand graphite for easy exfoliation by low-power ultrasonication. 86% of the as-made graphene sheets are 1-5 layers with lateral sizes as large as 210 μm^2. The graphene sheets are dispersible in water and exhibits very high stability. Raman and XPS studies show that the graphene sheets contain very little oxygen atoms, due to our non-oxidizing synthetic procedures. Transparent and conductive graphene thin films from 24 nm to 250 nm can be fabricated by a vacuum filtration method. We believe that the as-made graphene has great potential for the manufacture of high-performance electronic devices and graphene-reinforced composites.

CHAPTER 5 SOLUTION-PROCESSED GRAPHENE/SILVER NANOWIRE HYBRID ELECTRODES

5.1 Introduction

Graphene thin films prepared by either using exfoliated graphene nanosheets or reduction of GO flakes usually exhibit high sheet resistance, on the order of tens of kΩ sq^{-1}. For CVD-grown graphene, although the sheet resistance can be significantly decreased to ~120 Ω sq^{-1} after stacking several layers, the harsh growth conditions and complicated transfer process make it incompatible with solution process and large-area fabrication. Thus using graphene thin films alone to serve as transparent electrode can hardly defeat the conventionally used ITO electrode. Metal nanowires (NWs), as another promising candidate in electrode application, show superior properties to ITO including lower sheet resistance and higher transparency. However, the drawbacks of NW-derived films such as rough surface, low oxidation resistance and poor adhesion may restrict their wide applications. In order to prepare transparent electrodes with lower sheet resistance and good mechanical property, it seems reasonable to combine the 1D metal nanowires and 2D graphene nanosheets because metal NWs can lower the sheet resistance of graphene thin films and graphene films can provide good adhesion and mechanical protection for metal NWs. Some work has been done mainly based on the combination of CVD-graphene (or GO) and silver (or copper) NWs. Although they showed good performance as transparent electrodes, using CVD graphene is unfavorable for solution process, while GO requires further reduction process.[135, 136, 309, 310]

We herein report a solution-processed way to fabricate graphene-silver NW (G/Ag NW) hybrid electrodes on flexible substrates. Graphene nanosheets are prepared by salt-assisted direct exfoliation method previously developed by our group. After depositing Ag NWs and graphene nanosheets, the hybrid films can be obtained. The hybrid films exhibit good properties in both the sheet resistance and transparency, which is capable to serve as the transparent electrode for photovoltaic device applications, such as OSCs and perovskite solar cells.

5.2 Experimental

5.2.1 Fabrication of Graphene/Silver NW Hybrid Thin Films

Ag NWs with the average length and diameter of 50 μm and ~120 nm were purchased from Seashell Technology. 1 mg mL^{-1} dispersion of Ag NWs was prepared via dilution in isopropanol. The solution was spin-coated onto plasma treated glass (or 125-μm thick PET) substrate. Then graphene films prepared by vacuum filtration of graphene aqueous solution (refer to our previous work)[311] were transferred onto Ag NW films to fabricate hybrid electrodes.

5.2.2 Fabrication of Perovskite Solar Cells

A compact TiO_2 layer was deposited on the hybrid electrode by spin-coating tetrabutyl titanate (TBT) isopropanol solution with a concentration of 3 vol% at 5000 rpm for 30 s.[232, 266] After thermal annealing at 90 ^oC for 1 h in the ambient atmosphere, the perovskite layer was spin-coated atop via a two-step process in the N_2-filled glovebox: PbI_2 dissolved in DMF with a concentration of 460 mg mL^{-1} and MAI dissolved in isopropanol with a concentration of 10 mg mL^{-1} were sequentially spin-coated at 3000 rpm for 15 s and 30 s, respectively. After thermal annealing at 100 ^oC for 30 min, an HTL spiro-OMeTAD was spin-coated at 5000 rpm for 30 s and then placed in the desiccator (humidity <10%) overnight. Finally, Ag electrode was deposited by thermal evaporation.

5.2.3 Characterization

SEM (JEOL Model JSM-6490) was performed to characterize Ag NW, graphene and hybrid films. AFM (XE-100, Park Systems) was used to characterize the topography of thin films. Transmittance spectra of the as-prepared thin films were collected by UV-Vis spectrometer (Perkin-Elmer Lambda 18). The J-V characteristics of as-fabricated perovskite solar cells were measured in the glovebox under the illumination of 100 mW cm^{-2}. The light intensity was calibrated by using a standard silicon solar cell.

5.3 Results and Discussion

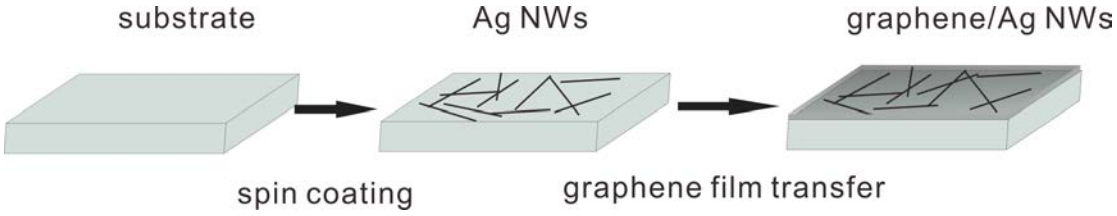

Figure 5.1. Scheme illustration of graphene/Ag NW hybrid films.

Figure 5.1 briefly depicts the fabrication process of graphene/Ag NW hybrid thin films. The Ag NW dispersion was first spin-coated onto glass substrates followed by the transfer of graphene film prepared by vacuum filtration. SEM and AFM were carried out to characterize the morphology of Ag NWs. As shown in Figure 5.2a and b, the average length and diameter are ~50 μm and ~80 nm, respectively. Figure 5.2c shows the SEM image of the graphene thin film, which is consisted of few-layered graphene nanosheets produced by our previously reported method. In Figure 5.2d, the well-percolated Ag NWs network was formed beneath graphene nanosheets. Ag NWs cannot only interconnect with each other but also bridge the voids between graphene nanosheets to increase the conductivity of hybrid films.

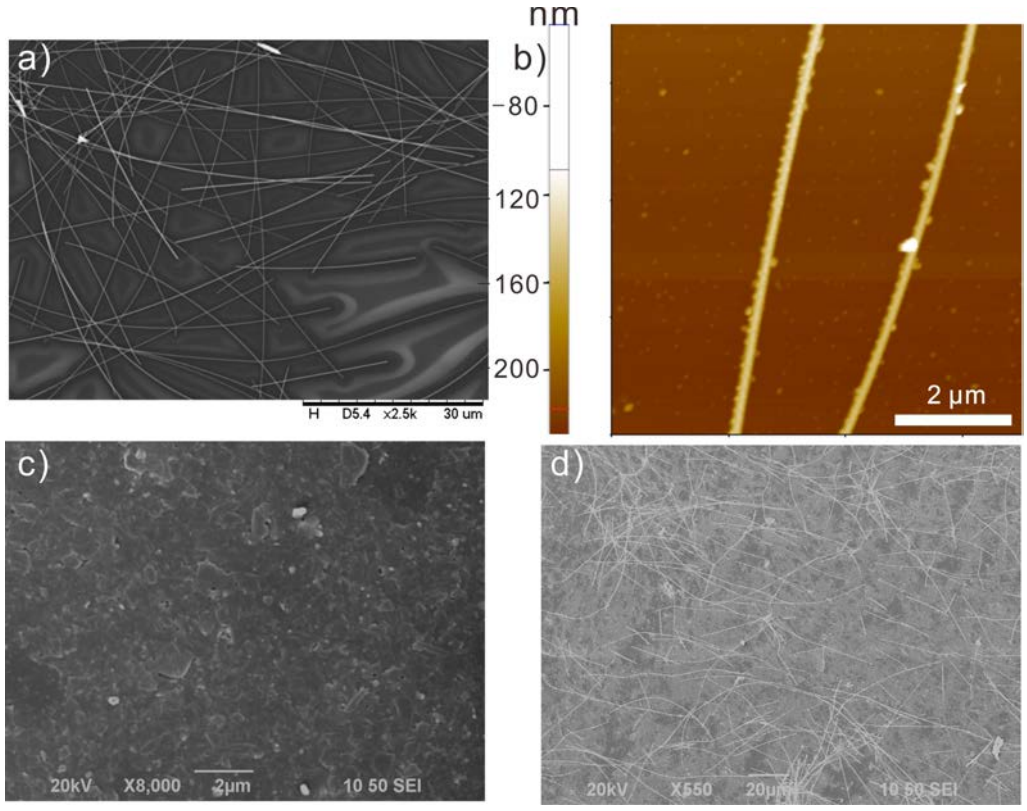

Figure 5.2. a) SEM image of Ag NWs. b) AFM image of Ag NWs. c) SEM image of graphene thin films. d) SEM image of G/Ag NW hybrid thin films.

To serve as the transparent electrode, a crucial issue that we need take into consideration is how to balance the conductivity and transparency of the hybrid films. UV-Vis spectroscopy was performed to measure the transmittance of as-prepared thin films. Ag NW thin films were acquired by varying the concentrations of Ag NW dispersions at a certain spin-coating speed (2000 rpm). The optical transmittance of Ag NW films decreased from 99.1% to 90.7% at 550 nm as the concentration increased from 0.1 mg mL^{-1} to 1.0 mg mL^{-1} (Figure 5.3a). Consequently, the sheet resistance decreased from the magnitude order of tens of kΩ sq^{-1} to ~130 Ω sq^{-1}. Considering that the pure graphene thin films prepared from nanosheets have higher sheet resistance,[311] a higher dosage of Ag NWs is necessary to lower down the sheet resistance of hybrid films. Therefore, 1 mg mL^{-1} was chosen to fabricate G/Ag NW hybrid films. Graphene thin films can be varied by controlling the solution volume and concentration added in the vacuum filtration process. After transfer, the thickness ranges from ~25 nm to ~200 nm. Figure 5.3b shows the transmittance of various hybrid films from 37% to 70%. The sheet resistance of all hybrid films is in the range of 100~150 Ω sq^{-1} (Figure 5.3c), which is similar to that of the pure Ag NW film. This means it is the Ag NWs that dominate the conductivity of hybrid films. Compared to literatures' work in which the hybrid films have a sheet resistance of <50 Ω sq^{-1} and a transmittance of >80%,[134, 136, 312] the performance of our hybrid films is a little poor. But this may be reasonable because the use of CVD graphene indeed improves the transmittance a lot. Here the results of hybrid films at least offer us convenience in solution-based fabrication of single-component or hybrid thin films. Moreover, this hybrid film could also be prepared on the flexible substrate. Figure 5.3d shows the bending test of hybrid films on the PET substrate. After 1000 bending cycles, the hybrid film remains highly conductive with nearly one time increased sheet resistance under the bending radius of 4.8 mm.

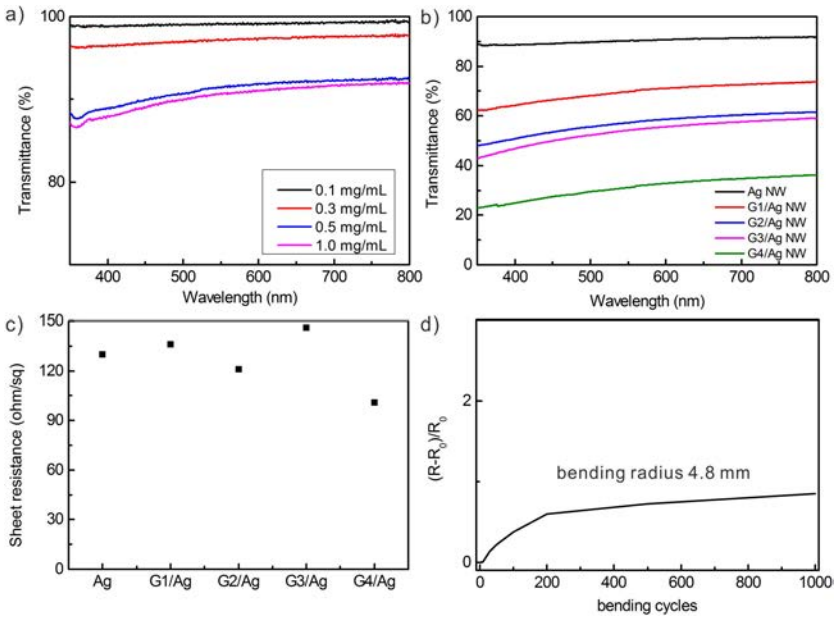

Figure 5.3. The optical transmittance spectra of Ag NW films a) and G/Ag NW hybrid thin films b). c) The sheet resistance of various thin films. d) The bending test of G1/Ag NW film on a PET substrate.

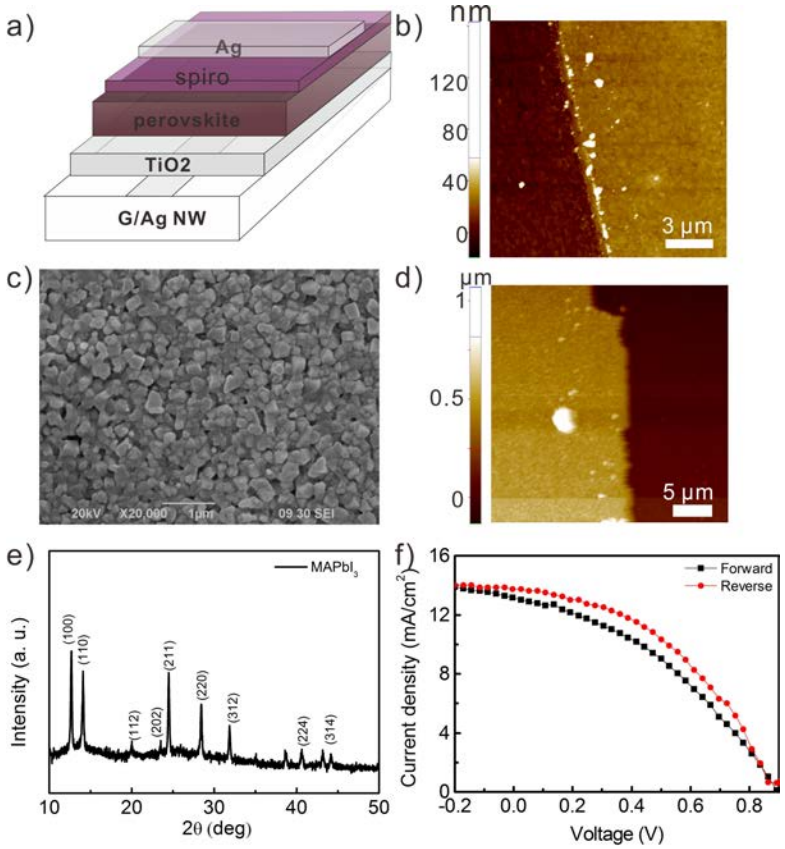

Figure 5.4. a) The schematic structure of perovskite solar cells. b) The AFM image of TiO_2. c) SEM image of perovskite layer. d) AFM image of perovskite

layer. e) XRD spectrum of perovskite layer. f) J-V curves of as-made perovskite solar cells.

To demonstrate the application of G/Ag NW hybrid films, the hybrid films were incorporated into perovskite solar cells to be transparent electrodes. The device structure is illustrated in Figure 5.4a. Figure 5.4b shows an AFM image of the compact TiO_2 layer with a thickness around 30 nm. The perovskite layer was fabricated by a two-step method. After sequentially spin-coating the solution of PbI_2 and MAI, the $MAPbI_3$ layer could gradually formed upon the reaction between PbI_2 and MAI followed by annealing treatment at 100 ^oC in the glovebox. In Figure 5.4c, we can clearly observe that the perovskite layer presents a homogeneous surface with densely packed grains of several hundreds of nanometers. The AFM image reveals the thickness of perovskite layer around ~380 nm. The crystallinity of perovskite layer was measured by XRD. In the XRD pattern, the strong diffraction peak at 14.1^o corresponds to the tetragonal structured perovskite,[313] while the peak located at 12.66^o indicates the presence of PbI_2, probably due to the incomplete conversion or the decomposition during the measurement. Figure 5.4f shows the J-V curves of as-fabricated perovskite solar cells (under 100 mW cm^{-2}, AM 1.5 G illumination). The device parameters are summarized in Table 5.1. The best device has a V_{oc} of 0.892V, a J_{sc} of 13.8 mA cm^{-2}, a FF of 42.9% and a PCE 5.3%. The hysteresis was also observed when the device was scanned in the forward or reverse directions. This can be ascribed to the interface contact between perovskite layer and TiO_2 and the scan rate.[314]

Table 5.1. The photovoltaic parameters of perovskite solar cells are summarized below.

	V_{oc} (V)	J_{sc} (mA cm^{-2})	FF (%)	η (%)
Forward	0.892	13.2	38.3	4.5
Reverse	0.892	13.8	42.9	5.3

For the preliminary results presented above, there are still some issues that we need be concerned. First of all, other than the vacuum filtration and transfer

process, another solution processable technique, e.g. spin-coating should be studied. This can further simplify the fabrication process by sequentially spin-coating Ag NWs and graphene solution. Much thinner graphene films could be obtained through multiple-spincoating process. Another issue is the surface topography of hybrid films, which is of great importance in device fabrication. Note that Ag NW films have relatively rough surface, which can be decreased by the deposition of graphene thin films on the top.[312] However, the graphene film prepared by vacuum filtration also results in a rough surface, because it replicates the rough topography of the filter membrane. Therefore, films prepared by spin coating are expected to ease the surface roughness. As shown Figure 5.2d, the rough surface and exposed Ag NWs may penetrate the perovskite layer, leading to a short-circuit devices. Further optimizing the fabrication of hybrid films including sheet resistance, transmittance and surface morphology can readily improve the performance of perovskite solar cells beyond the PCE of 10%.

5.4 Conclusions

G/Ag NW hybrid thin films have been successfully fabricated by a solution processed approach and they exhibit a sheet resistance of ~130 Ω sq^{-1} and a transmittance of 70%. More importantly, the hybrid films can be integrated into the perovskite solar cells as transparent electrodes and the as-made devices show a PCE of 5.3%. Though the performance is not good enough, much room for further optimization, e.g. using the spin-coating method to prepare graphene thin film to improve the transparency, this work is beneficial for the solution-processed fabrication of hybrid thin films and subsequent devices by integrating the scale-up produced graphene nanosheets.

CHAPTER 6 SALT-ASSITED DIRECT EXFOLIATION OF TMDs AND THEIR APPLICATION IN ORGANIC SOLAR CELLS

In this chapter, salt-assisted direct exfoliation method is extended to prepare other 2D nanomaterials beyond graphene. Among those, TMDs representing a special class contain dozens of compounds. Upon the exfoliation, they exhibit diverse properties, which are of great importance in electronic and photo electronic applications.

6.1 Introduction

TMDs such as MoS_2, $MoSe_2$, WS_2 and WSe_2 have the common chemical formula of MX_2, where the transition metal M is sandwiched between two layers of chalcogen X. Although atoms in-plane are strongly linked by covalent bonds, the adjacent layers out-of-plane are weakly held together by van der Waals force, which allows the exfoliation of bulk TMDs into atomically thin, single- and few-layer two dimensional (2D) materials. Compared with zero-bandgap graphene, these TMD 2D materials possess obvious semiconductor bandgaps,[315] which show remarkable advantages for a wide range of applications including field effect transistors,[316-318] sensors,[316] energy storage devices,[83, 194, 319, 320] and optoelectronics.[196, 197, 321]

To date, available methods for the preparation of single- and few-layer TMD 2D materials can be categorized into two types, i.e., bottom-up growth by chemical vapor deposition (CVD),[43] and top-down exfoliation from bulk TMD crystals by micromechanical cleavage method,[53, 322] chemical[103] and electrochemical[113] Lithium-intercalation and exfoliation, and liquid-phase ultrasonic exfoliation.[80, 81]. Among these methods, mechanical cleavage can only produce samples for some fundamental studies because of its extremely low throughput. As of CVD, it synthesizes 2D sheets with reasonable quality and a typical size ranging from hundreds of nanometers to several micrometers. However, reported literatures are mainly limited to the growth of MoS_2 2D

materials.[42, 43] Lithium intercalation methods can give high yield of monolayer TMD 2D materials, yet fails to keep its structure integrity. The presence of structural deformations results in altered electronic properties from semiconducting to metallic and an additional annealing step is required to restore their semiconducting properties.[116] The use of Li compound also raises a safety issue for scientists to pursue alternative intercalants.

On the other hand, liquid-phase ultrasonication of TMDs in either organic solvents[81] or surfactant-containing[89] aqueous solutions shows several promising prospects to yield few-layer TMD 2D materials. It is environmental-friendly in the sense that no hazardous and oxidative chemicals are needed in the synthesis. It is also convenient to form composites or hybrids by simply mixing the dispersions of desirable materials. However, current state-of-the-art liquid exfoliation requires very long sonication time, and the yield is very low. Indeed, highly desirable is a versatile, environmental-friendly, and low-cost synthetic method that allows producing many kinds of single- and few-layer TMD 2D materials with high yields.

To address the challenge, we report herein a modified liquid-phase ultrasonication method, namely “salt-assisted liquid-phase exfoliation”, which yields single- and few-layer TMD 2D sheets including MoS_2, $MoSe_2$, WS_2, and WSe_2 in a large quantity and high quality by simple ultrasonication of TMD bulk crystals in liquid solvents with the aid of low-cost and non-toxic inorganic salts. This method is in part inspired by our previous work, in which a salt-assisted synthetic concept was developed to exfoliate graphite powders into large-size and high-quality few-layer graphene.[311] In that report, we found that the incorporation of inorganic salts could effectively improve the efficiency and yield of ultrasonic exfoliation. Similarly herein, the time required for exfoliation in our salt-assisted method reduces significantly to only one-fourth, while the yield of TMD 2D materials increases by more than one order of magnitude, compared with abovementioned liquid-phase exfoliation without salts.

In this salt-assisted synthesis, powders of TMD crystals are immersed in an inorganic salt containing aqueous solution, and salt ions are allowed to enter into

the inter-layer spaces of TMD crystals as the solution becomes supersaturate upon water evaporation. This intermediate product is then exfoliated easily into corresponding single- and few-layer 2D sheets by low power ultrasonication in an organic solvent. Importantly, because the process does not involve any high-energy activation or oxidizing reagent, the as-made TMD 2D flakes maintain high quality with little defects. We demonstrate that 65% of the as-made TMD 2D sheets are 1-5 layers and their lateral sizes are hundreds of nanometers to several micrometers. Most of the reagents can be readily separated and recycled for further synthesis. As proof-of-concept application in optoelectronic devices, the as-produced MoS_2 2D materials is solution-casted into thin films in various ways for use as the hole transport layer (HTL) in bulk heterojunction OSCs, which improves the open circuit voltage from 0.34 V to 0.58 V.

6.2 Experimental

6.2.1 Preparation of Single and Few-layered TMD 2D Sheets

All TMD materials were purchased in powder form. Raw TMDs materials are as follows: MoS_2 (Aldrich, <2 μm), $MoSe_2$ (Accuchem), WS_2 (Aladdin, 6 μm), and WSe_2 (Alfa Aesar, 10 μm). The mixture of TMD (MoS_2, $MoSe_2$, WS_2, or WSe_2, 100mg), inorganic salt (NaCl or $CuCl_2$, 2g, Sigma-Aldrich) and SDBS (0.5 g, Sigma-Aldrich) were added into 100 ml deionized water, stirred at 500 rpm for 48 h at 100 ^oC and then the water was evaporated. The resulting residue was added into 40 mL organic solvent (N-methyl-2-pyrrolidone (NMP), or N,N-dimethylformamide (DMF)) and ultrasonicated (sonic bath, Mode PS-40B, 240 W) for ca. 2 h followed by vacuum filtration and washing to remove excess salt and SDBS. The filtered residue was redispersed into DI water by ultrasonication for 10 min followed by centrifugation at 3000 rpm for 5 min. The upper solution was collected as the few-layer TMD solution for further characterizations. Control experiments were also carried out via direct sonication of raw TMDs without salt following the same procedures described above.

6.2.2 Material Characterization

Materials were characterized by using TEM (JEOL JEM-2010), AFM (XE-100 Park System) and Raman spectrometer (514 nm laser, Renishaw microprobe RM 1000). In the Raman test, samples were prepared by diluting the final product into ethanol followed by drop casting onto SiO_2/Si substrates. We used the same samples for the Raman characterization after performing AFM measurement. The Raman spectroscope was calibrated with Si peak located at 520 cm^{-1} as the internal reference. The grating we used is 1800 lines/mm. Absorbance spectra were collected by UV-vis spectrometer (Perkin-Elmer Lambda 18) with quartz cuvettes. X-ray diffraction (XRD) characterization was conducted on X-ray powder diffractomerter (RigakuSmartLab) with monochromatic Cu Kα radiation (λ = 1.5418 Å).

6.2.3 Fabrication and Characterization of OSCs

The exfoliated MoS_2 sheets were deposited onto the surface of pretreated ITO glass to form a thin film via film transfer and drop casting. For film transfer, MoS_2 films were prepared by vacuum filtration and then transferred onto ITO surface followed by subsequent annealing at 500 ^oC for 1 h under an argon atmosphere. In drop casting method, MoS_2 aqueous solution was diluted in methanol. Films were formed after dropping the solution for several times followed by the same annealing process. The active layer consisted of a blend of regioregular P3HT (20 mg mL^{-1}) and PCBM (16 mg mL^{-1}) dissolved in chlorobenzene, was spin-coated on MoS_2 film and then annealed at 145 ^oC for 5 min in nitrogen-filled glovebox. Al electrode (thickness, 100 nm) was deposited on top by thermal evaporation. The effective area is 0.08 cm^2 (4 mm × 2 mm). The J-V characteristics of the OSCs were measured via the Keithley 2400 source meter under illumination of the solar simulator equipped with an AM 1.5 filter, 100 mW cm^{-2} (Newport 91160, 300 W). The light intensity was calibrated with a standard silicon solar cell.

6.3 Results and Discussion

6.3.1 Characterizations of As-made TMD 2D nanomaterials

As schematic illustration of the synthetic process in Figure 3.1, few-layered TMDs were prepared. We quantified the yields of salt-assisted synthesis by measuring the UV-vis absorption of aqueous solutions of as-made TMD 2D sheets. Figure 6.1 and figure 6.2 shows the UV-vis spectra of aqueous solutions of TMD 2D nanomaterials prepared by NaCl- and $CuCl_2$-assisted exfoliation, respectively. *A*/*l* is defined as the optical absorbance per cell length, where *A* is the absorbance of TMDs 2D sheets at given wavelengths and *l* is the length of testing cell. Because the concentrations of TMD 2D sheets are proportional to corresponding *A*/*l*, we can readily compare the yields of these TMD 2D sheets synthesized with various salts and solvents. All TMD 2D sheets disperse steadily in aqueous solutions without obvious precipitation for more than one month. As control experiments, we also synthesized TMD 2D sheets without the use of inorganic salts, which is similar to the procedures reported by Cunningham et. al.[81] Table 1 summarizes the results and the ratio listed represents the differences of the TMDs sheets prepared by our method versus those prepared without salts. It is obvious that the salt-assisted synthesis offers much higher yields, as many as 32 folds compared with the direct sonication method.

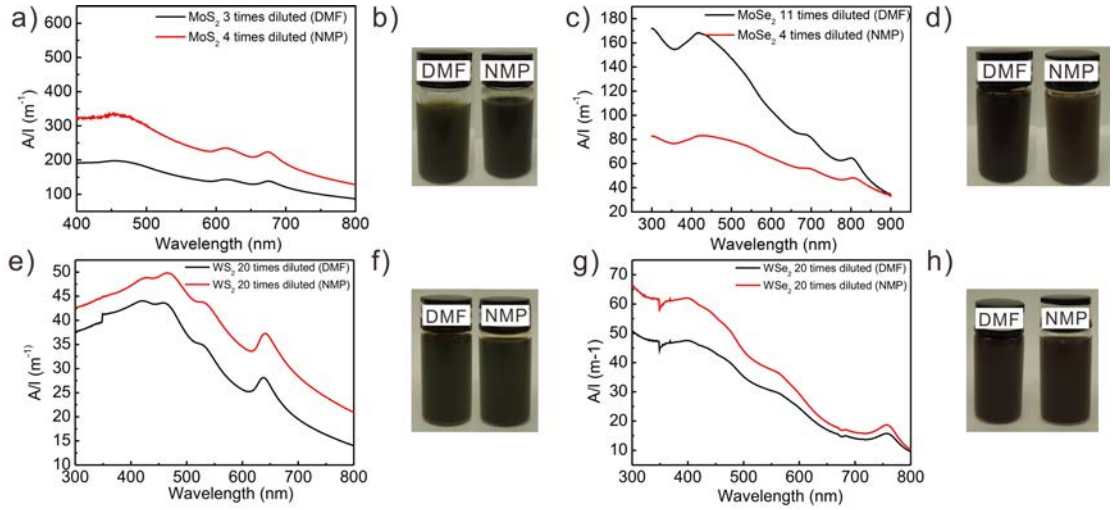

Figure 6.1. UV-vis spectra (a, c, e, and g) and digital images (b, d, f, and h) of aqueous solutions of TMD 2D materials prepared by NaCl-assisted exfoliation in various organic solvents.

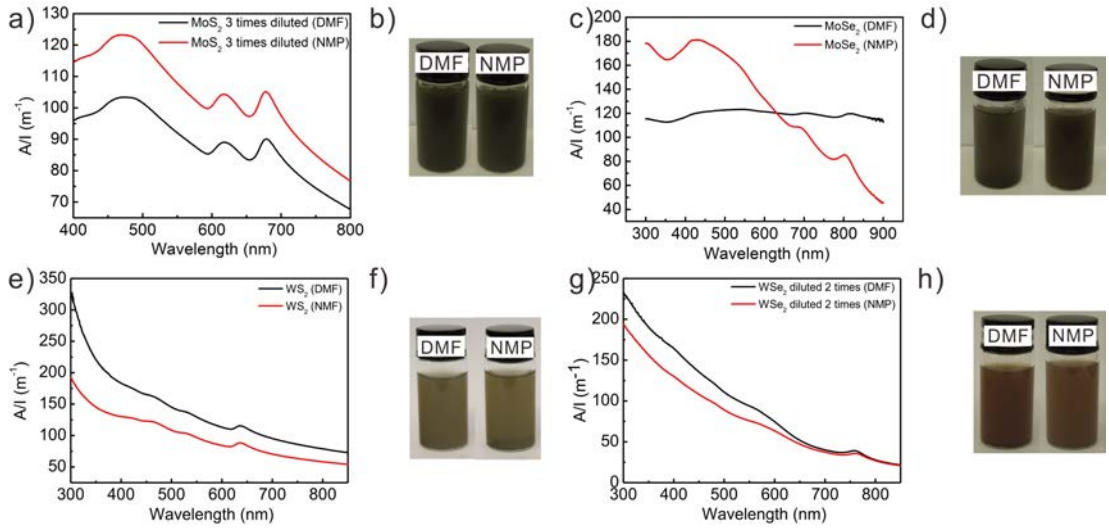

Figure 6.2. UV-vis spectra (a, c, e, and g) and digital images (b, d, f and h) of aqueous solutions of TMD 2D materials prepared by $CuCl_2$-assisted exfoliation in various organic solvents.

In fact, the yield can be further improved with longer boiling (step 2) time. Figure 6.3 shows the time-dependent yields of all 2D TMDs with boiling time ranging from 2 days to 14 days. Take MoS_2 for example. The relative yield increases to 87 folds with 14 day boiling. Increasing the initial concentration of the TMD crystals can also increase the concentration of the final 2D TMDs. For example, when the initial concentration MoS_2 crystal was increased from 2.5 mg mL^{-1} to 20 mg mL^{-1}, and the final concentration of 2D materials increased from ~0.8 mg mL^{-1} to ~6 mg mL^{-1}. In this synthesis, SDBS acts as surfactant to help the dispersion of starting materials and final products. Without adding SDBS, the starting materials precipitated and the synthesis was much less effective. It should be noted that SDBS can attach to 2D materials very stability and is difficult to fully remove. The amount of SDBS in our final 2D TMDs is estimated to be ~1% by TGA analysis.

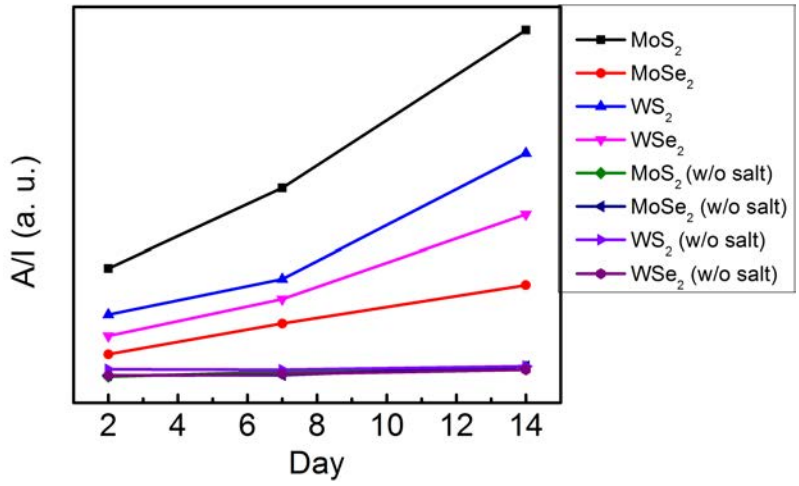

Figure 6.3. Time dependence (boiling time) measurement of the yields of 2D TMDs synthesized with and without (w/o) inorganic salts.

In order to study the exfoliation effectiveness, X-ray diffraction (XRD) was performed on the starting materials and final products. This measurement can qualitatively identify whether TMD crystals are exfoliated into few-layer sheets or not. Take salt-assisted exfoliation of MoS_2 for example. Bulk MoS_2 gives XRD finger print peaks at 14.4^o, 28.9^o, 32.6^o, 33.4^o, 35.8^o and 39.4^o, which are attributed to its (002), (004), (100), (001), (102) and (103) planes (Figure 6.4a). After salt-assisted exfoliation, the final product shows a single peak of (002) plane, while the rest of the peaks weaken significantly, or even disappear. This result is clear evidence showing the formation of few-layer MoS_2 2D sheets, according to the literature report.[195, 323] For the other TMDs exfoliated in the presence of NaCl or $CuCl_2$, similar phenomena are observed: the final TMD 2D flakes exhibit a single peak assigned to their corresponding (002) plane. The XRD results indicate that the high-yield exfoliated flakes are indeed few-layer 2D materials.

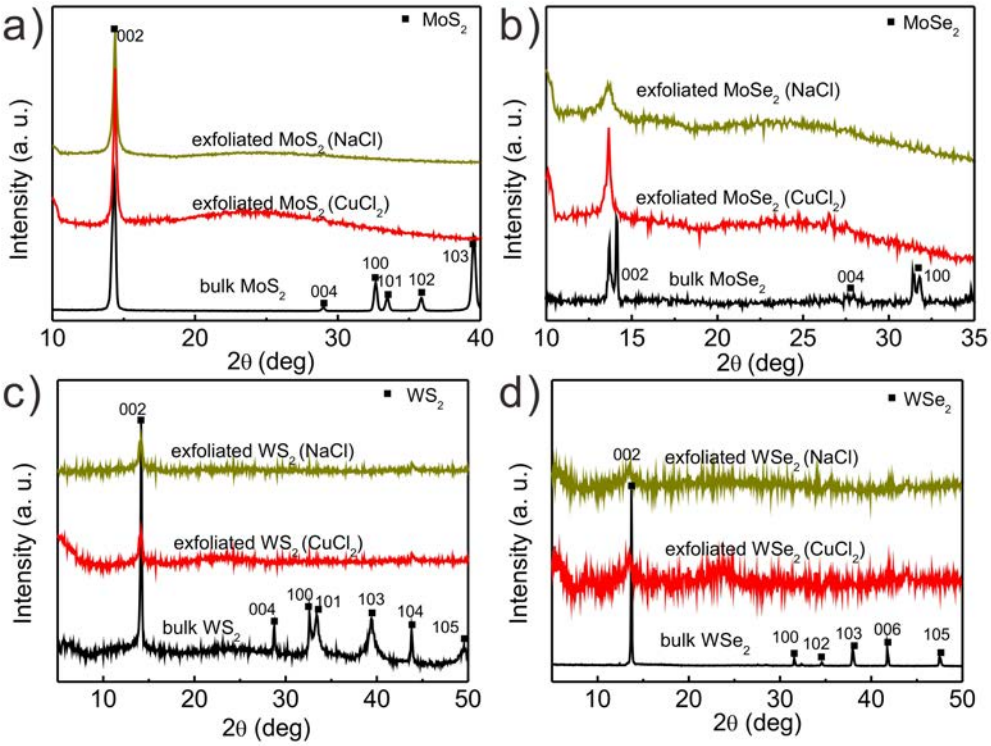

Figure 6.4. XRD spectra of bulk TMDs and their corresponding exfoliated 2D sheets prepared by salt-assisted liquid exfoliation using NaCl and $CuCl_2$.

In addition, Raman spectroscopy was also performed to study our TMD 2D sheets. Two typical Raman active modes, E^1_{2g} and A_{1g}, were generally employed to evaluate thickness of TMDs 2D sheets.[324, 325] The in-plane mode of E^1_{2g} derives from the vibration of two chalcogen atoms in a direction varying from the metal atom, while the out-of-plane mode of A_{1g} corresponds to the vibration of two chalcogen atoms in opposite direction. The location and the wavenumber difference of these two peaks are sensitive to the material thickness when the layer number is less five. For MoS_2 2D sheets, both peaks shift to higher wavelength numbers compared with their bulk crystals. Meanwhile, their difference in Raman shift decreases from 25 cm^{-1} (bulk) to 24 cm^{-1}. This result is consistent with literature report, in which similar MoS_2 powers were exfoliated into 2D sheets.[326] For WS_2, peak E^1_{2g} blue shifts, while peak A_{1g} red shifts, which is also consistent with literature report.[48] For $MoSe_2$, the A_{1g} peak shifts to the lower wavenumber. For WSe_2, the E^1_{2g} peak slightly shifts to higher wavenumber, respectively (Figure 6.5). All the Raman data also confirms that as-made TMD flakes are indeed few-layer 2D materials.

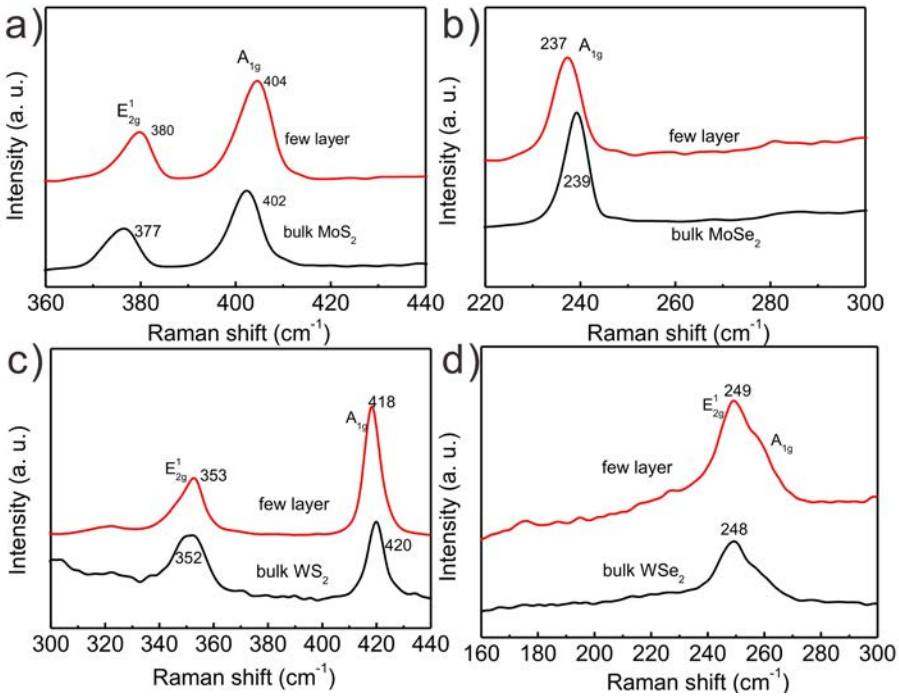

Figure 6.5. Raman spectra of bulk TMDs and their corresponding exfoliated 2D sheets prepared by NaCl-assisted exfoliation in NMP using 514 nm excitation laser, a) MoS_2, b) $MoSe_2$, c) WS_2 and d) WSe_2.

For quantitative analysis, atomic force microscopy (AFM) was further used to quantify the size and thickness distributions of TMD 2D sheets. Approximately forty pieces of samples were imaged and analyzed for each kind of TMD 2D sheets. Figure 6.6 shows typical AFM topographies which we observed: the lateral size ranges from hundreds of nanometers to several micrometers, and the thickness ranges from ~0.75 nm to ~3.5 nm. Note that the reported thickness of single-layer TMD 2D sheets was 0.6~1 nm.[317, 327-329] As such, according to the statistical counts of the thickness of each sample (Figure 6.3), we can conclude that approximately 100% of the products we obtained are few-layer 2D sheets (< 10 layers). For MoS_2, $MoSe_2$ and WS_2, at least 65% of the products are less than 5 layers. For control experiments without adding salt, stacked multilayer nanosheets were found, with lateral sizes of a few hundred nanometers. The white particles occurred in the AFM images should be some nano debris of TMDs sheets absorbed on top of larger flakes or Si substrate. Note that the layer thickness distribution could be further narrowed down by varying the centrifugation speed and time. The optimization of other factors including the

choice of salt and organic solvents, boiling time, sonication time can only impose effect on the yield.

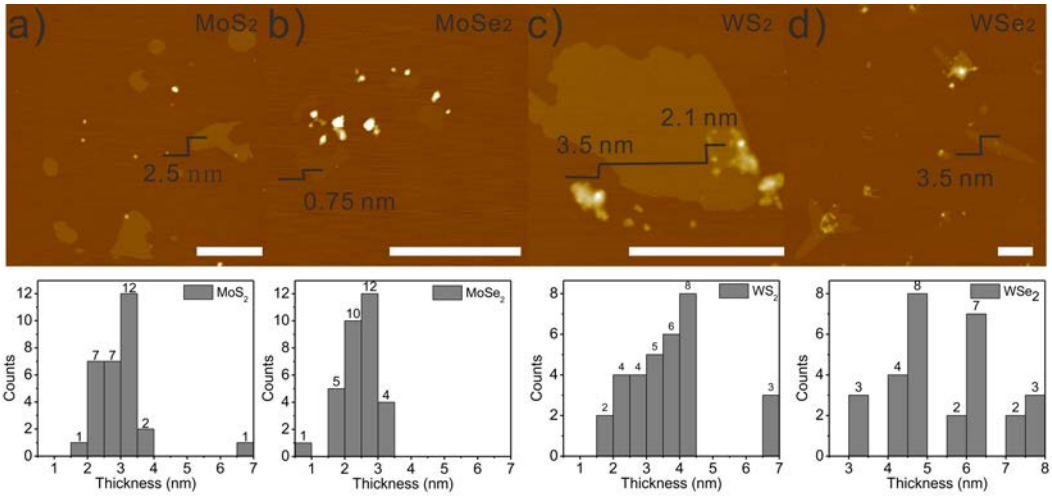

Figure 6.6. Typical AFM topographic images of exfoliated TMD 2D sheets: a) MoS_2, b) $MoSe_2$, c) WS_2 and d) WSe_2 and their corresponding thickness distributions, scale bars: 2 μm.

Importantly, our TEM study reveals the single crystalline features of all as-made TMD 2D sheets (Figure 6.7 and 6.8). Atoms exhibit symmetrical arrangement in a hexagonal manner with d-spacings being 2.7 Å, 2.8Å, 2.7Å, and 2.8Å, which correspond to the (100) planes of MoS_2, $MoSe_2$, WS_2, and WSe_2, respectively.[330] EDX analysis was also performed in the TEM experiments. EDX results show elements of the 2D TMDs. No salts (NaCl or $CuCl_2$) signal was observed, indicating the removal of the salts in the rinsing process (Figure 6.9). It should be noted that the maintenance of the single crystalline feature without attachment of salt is critical when these 2D materials are made for electronic and optical applications.

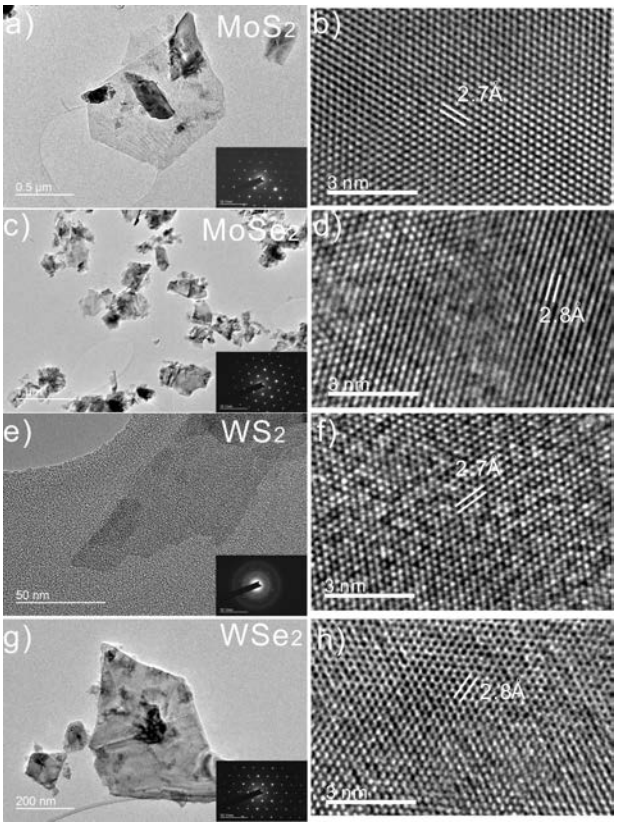

Figure 6.7. TEM images of few-layered TMDs sheets prepared by NaCl-assisted exfoliation: a) MoS_2, b) $MoSe_2$, c) WS_2, and d) WSe_2. Insets are the SAED patterns. b), d), f) and h) are the corresponding HRTEM images.

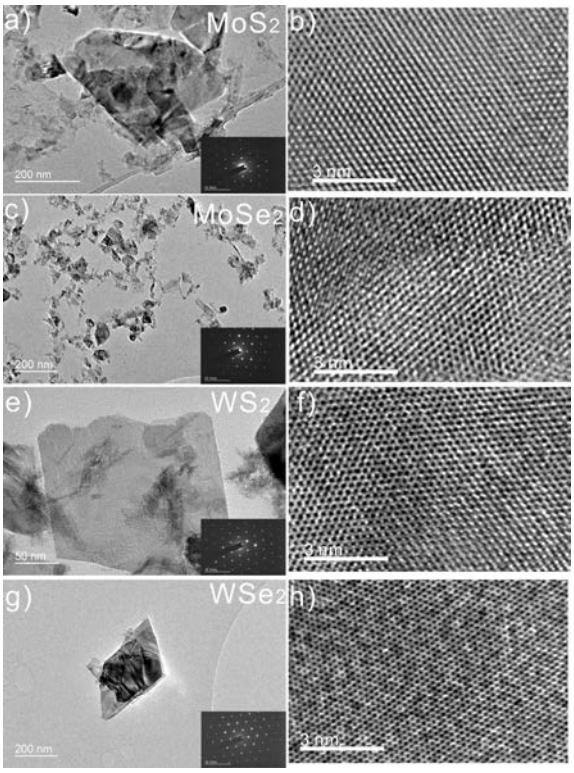

Figure 6.8. TEM images of few-layered TMD 2D sheets prepared by $CuCl_2$-assisted exfoliation: a) MoS_2, b) $MoSe_2$, c) WS_2, and d) WSe_2. Insets are the SAED patterns. b), d), f) and h) are their corresponding HRTEM images.

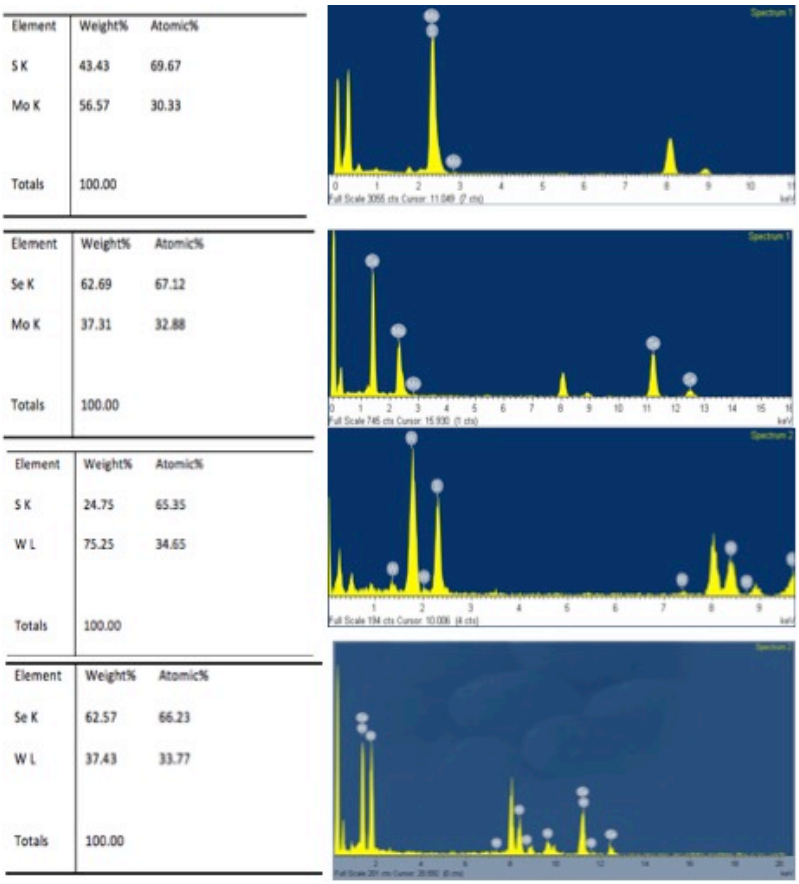

Figure 6.9. EDX analysis (in TEM) of as-produced TMD 2D sheets. Spectra and analysis shown from top to bottom are for MoS_2, $MoSe_2$, WS_2, WSe_2, respectively.

6.3.2 Application in OSCs

To demonstrate that these TMD 2D sheets exfoliated by salt-assisted method can be used in optoelectronic devices, we integrated thin films of exfoliated MoS_2 2D sheets as hole transport layer (HTL) into OSCs. MoS_2 thin films were fabricated by two solution-based methods including (1) film transfer via vacuum filtration, and (2) drop casting. P3HT:$PC_{61}BM$ was used as a model active layer, and PEDOT:PSS was used as reference HTL for comparison. The OSCs device architecture is ITO/HTL/P3HT: $PC_{61}BM$ (300 nm)/Al (Figure 6.10a). Under dark condition, all devices with MoS_2 HTL show lower reverse saturation current and a higher rectification ratio up to 10^2 compared with that with PEDOT:PSS HTL,

indicating that MoS_2 thin film functions effectively as the hole transport and electron blocking layer (Figure 6.10c). The most representative photovoltaic characteristics of the OSCs (under AM 1.5 illumination) including short-circuit current density (J_{sc}), open-circuit voltage (V_{oc}), fill factor (FF), and PCE are summarized in Table 2.

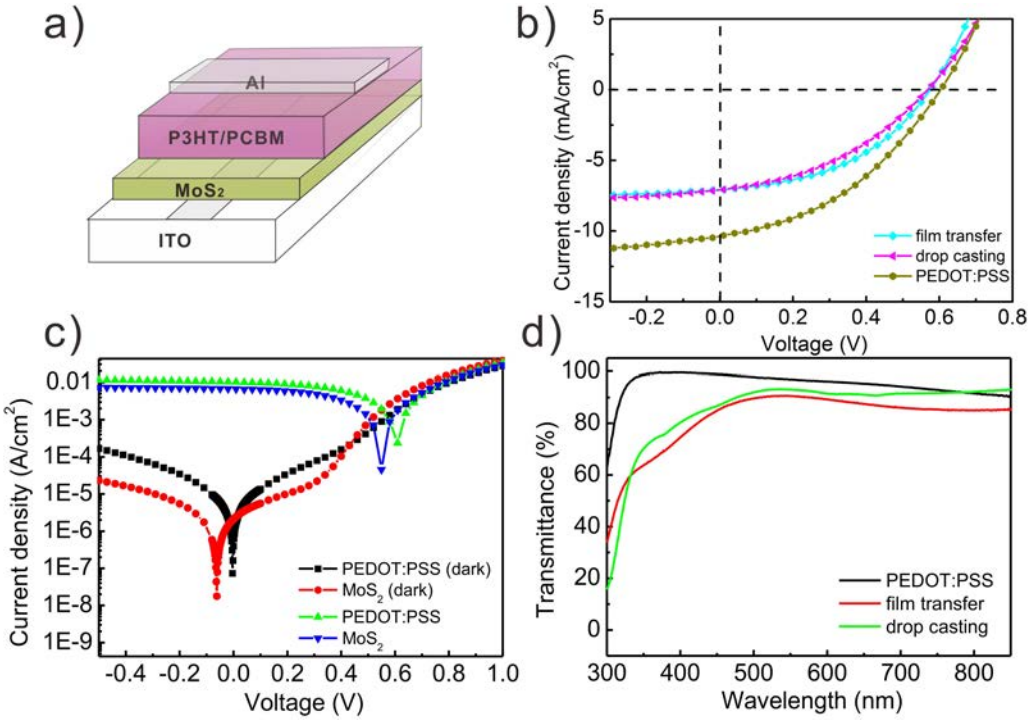

Figure 6.10. a) Structure of OSCs using HTL made of few-layer MoS_2 2D sheets. b) J-V curves of as-made OSCs under solar simulator. MoS_2 HTLs were prepared by film transfer and drop casting methods. c) Typical J-V characteristics of OSCs with MoS_2 HTL prepared by drop casting and PEDOT:PSS under illumination and dark condition. d) The transmittance of different HTLs on ITO glasses.

For the film transfer method, MoS_2 thin films were prepared by vacuum filtration of their aqueous suspension through a cellulose ester filter with nano-sized pores, and then transferred onto the ITO glass. Therefore, the thickness of MoS_2 could be manipulated by adding different volume of the suspension. After a thickness-performance optimization, the best PCE is 1.81%, with a V_{oc} of 0.58 V, a J_{sc} of 7.1 mA/cm^2, and a FF of 0.440. In the optimized device, the roughness and thickness of the MoS_2 HTL are ~55 nm and ~86 nm, respectively. The high V_{oc} indicates that MoS_2 2D sheets synthesized with salt-assisted method can be used

for effective HTL in OSCs. This high roughness is attributed to the rough surface morphology of the filter paper. The transmittance of the MoS_2 HTL characterized by UV-vis spectrometer is 90.6% at 550 nm, about 6% less than that of PEDOT:PSS (Figure 6.10d).

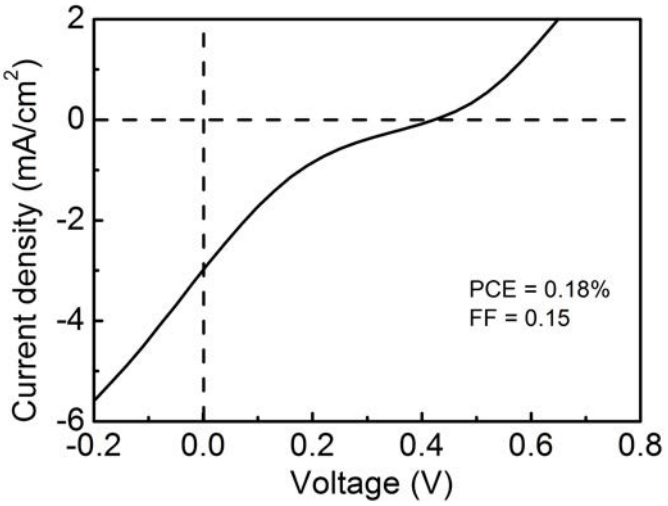

Figure 6.11. The J-V curve of OSCs fabricated by single time drop casting.

For the drop casting method, we found that very poor PCE (only 0.18%) was obtained when single drop casting was used to form MoS_2 HTL (Figure 6.11). This is because single drop casting results in poor surface coverage of MoS_2 on ITO, which leads to low V_{oc} and FF.[194] As such, multiple cycles of drop casting are needed to obtain a dense MoS_2 HTL with high coverage on ITO. Typically, we found that four cycles are needed to obtain a dense film, with a roughness of ~38 nm, a thickness of 55 nm, and ~93.1% transmittance at 550 nm (Figure 6.10d and 6.12). With this dense layer, the PCE is improved to 1.59% (Figure 6.10b), with a V_{oc} of 0.58 V, a J_{sc} of 7.1 mA/cm^2, and a FF of 0.389. These device performances are comparable to those works using MoS_2 HTL synthesized with other methods,[194, 196, 321] showing that MoS_2 2D sheets synthesized by our salt-assisted method are suitable to fabricate HTLs for OSCs.

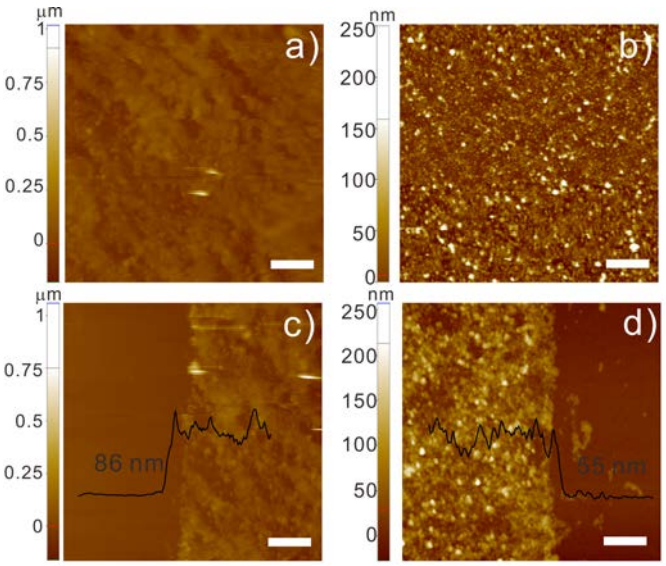

Figure 6.12. AFM topographic images of MoS_2 thin films prepared by a, c) film transfer, and b, d) drop casting of few-layer MoS_2 2D sheets. Scale bars: 5 µm.

Table 6.1. Summary of the optical absorbance of aqueous solutions of TMD 2D sheets synthesized by salt-assisted liquid exfoliation method.

TMDs	solvent	salt	A/l (m^{-1})	control (w/o salt) A/I (m^{-1})	yield ratio
MoS_2 (670 nm)	DMF	NaCl	409.8	59.6	6.9
		$CuCl_2$	263.1		4.4
	NMP	NaCl	886.6	27.7	32.0
		$CuCl_2$	307.7		11.1
$MoSe_2$ (808 nm)	DMF	NaCl	698.2	42.2	16.5
		$CuCl_2$	119.3		2.8
	NMP	NaCl	192.3	50.5	3.8
		$CuCl_2$	84.4		1.7
WS_2 (633 nm)	DMF	NaCl	637.4	53.8	11.8
		$CuCl_2$	115.1		2.1

WSe_2 (768 nm)	NMP	NaCl	512.8	57.1	9.0
		$CuCl_2$	88.0		1.5
	DMF	NaCl	292.8	32.1	9.1
		$CuCl_2$	74.7		2.3
	NMP	NaCl	342.0	15.9	21.5
		$CuCl_2$	69.6		4.4

Table 6.2. Photovoltaic characteristics of OSCs without HTL and with different HTLs. Average PCE is calculated out of 5 devices.

HTL	J_{sc} (mA/cm^2)	V_{oc} (V)	FF (%)	PCE (%)	Avg. PCE (%)
MoS_2 (film transfer)	7.1	0.58	44.0	1.81	1.57
MoS_2 (drop casting)	7.1	0.58	38.9	1.59	1.54
PEDOT:PSS	10.3	0.61	39.7	2.50	2.34
w/o HTL	0.37	0.34	13.5	0.02	0.016

6.4 Conclusions

In conclusion, we have reported a salt-assisted liquid exfoliation method, which can dramatically improve the yield of synthesizing single and few-layer TMD 2D materials during ultrasonication process by more than one order of magnitude when compared with the state-of-the-art. Importantly, these TMD 2D sheets remained their single crystalline features, which are critical for optoelectronic applications. As proof-of-concept, solution casted thin films of MoS_2 2D sheets were integrated into OSCs to serve as the HTL, which shows a remarkable improvement of the V_{oc} from 0.34 V to 0.58 V. Because the synthesis does not require any hazardous chemicals, electrochemical setup, or special reaction chamber, the salt-assisted strategy is very promising to scale up for mass production in the future. In addition, this method is applicable to produce other

2D nanomaterials. Solution-processed manners provide convenience for material synthesis and device fabrication.

CHAPTER 7 STUDY OF POLYMER BRUSHES FUNCTIONALIZED GRAPHENE TRANSISTORS

7.1 Introduction

In the past decade, graphene has attracted worldwide attention owing to its unique structure and excellent properties in mechanics, electronics and so on. Concrete evidence has proved that it is a promising candidate for biosensing and bioelectronic applications, such as the detection of DNA molecules[331-333] and protein adsorption[334]. To achieve such kind of applications, especially on CVD grown graphene that has good electrical property, we have to provide specific chemical functionality to receive the foreign species. Various strategies have been developed for the modification of pristine graphene surface, including non-covalent and covalent ways.[158, 335-340] For the covalent way, it will inevitably cause some destructive effect to the graphene structure and degrade its electrical performance.[341] While the noncovalent approaches often involve the π-π stacking by using aromatic molecules. The modification by using polymer brushes that can be conducted in a noncovalent way is a better choice, because it can provide multiple and selective functional sites for the immobilization of biomolecules. Polymer brushes assisted modification provides a facile way for the design of biosensors; meanwhile it doesn't exert the negative effect on the graphene structure and consequent device performance. Depending on the applications, such as sensing specific biomolecules, we can tailor-make a suitable kind of polymer brush by selecting the proper monomer. Although the modification of graphene by polymer brushes has been frequently reported and even used as a platform or scaffold to construct biosensors,[157, 158, 342] there are few researches to fundamentally investigate the electrical properties of polymer brushes functionalized graphene.

Thus in this contribution, we fabricate polymer brushes functionalized graphene FET devices by using CVD grown monolayer graphene and various polymer brushes. The electrical properties of graphene FET devices with and without the modification of polymer brushes are compared in terms of the variation of charge

carrier mobility and Dirac point shift. As a proof-of-concept application in biosensing, DNA molecules are immobilized on the functional polymer brushes and the consequent electrical performance is studied as well.

7.2 Experimental

7.2.1 CVD Growth of Graphene on Copper Foil

Single layered graphene was synthesized on a 25-μm thick copper foil (Alfa Aesar, 99.8% metal basis) by the CVD process. The typical procedure is as follows: a piece of Cu foil was loaded into the furnace tube and then heated to 1050 ^{o}C in the presence of H_2 protection (10 sccm); after annealing for 20 min to remove the possible residual organic substances and oxides, CH_4 (15 sccm) was introduced as the carbon feedstock to initiate the reaction for 15 min; then the CH_4 was turned off, in the meanwhile the heater was moved aside and the furnace was shut down to cool down the temperature.

7.2.2 Fabrication of Graphene FET

The pre-patterned gold electrodes were prepared by conventional photolithography (Karl Suss/MA 6 Aligner) on 300 nm SiO_2/Si substrate followed by e-beam metal deposition (10 nm Cr/50 nm Au) to serve as the drain and source electrodes. After lift-off of the photoresist, CVD-grown monolayer graphene was wet transferred onto SiO_2/Si substrate by etching away Cu foil in 0.3M ammonium persulfate solution. After removal of the PMMA protective layer, graphene was annealed at 300 ^{o}C in inert atmosphere for 1 h. Then photolithography was employed to define the specific channel length (10 μm) and width (10, 5, 3 and 2 μm) of graphene FET by using positive photoresist (AZ 5214E). After developing, the substrate was treated by O_2 plasma for 10 min followed by the removal of photoresist in acetone.

7.2.3 Fabrication of Polymer Brushes Functionalized Graphene FET

As-prepared graphene FET with or without patterned channel width were used to prepare polymer brushes functionalized graphene FET. The substrate was immersed into the macro-initiator (poly[2-(2-bromoisobutyryloxy) ethyl

methacrylate-co-4-(1-pyrenyl) butyl methacrylate]) solution (2 mg mL^{-1} in DMF) for 24 h in the dark at room temperature to form an assembled layer on graphene surface. Subsequently, it was rinsed by DMF and acetone to remove the physically absorbed initiator and dried by N_2. SI-ATRP was performed in tubes. The recipes of polymerization for various monomers are as follows: methyl methacrylate (MMA) 6.0 mL, copper bromide (CuBr) 0.14 g, 2, 2'-bypyridyl (bipy) 0.3 g, water/methanol (30 mL, 1/4 V/V), 15~45 min, room temperature; glycidyl methacrylate (GMA) 6.0 mL, CuBr 0.063 g, bipy 0.17 g, water/methanol (30 mL, 1/4 V/V), 10~40 min, room temperature; poly(ethylene glycol) methyl ether methacrylate (OEGMA) 4 mL, CuBr 0.07 g, bipy 0.156 g, water/methanol (30 mL, 1/4 V/V), 0.5~2 h, room temperature. All the chemicals mentioned above were purchased from Sigma-Aldrich.

The Br-containing macro-initiator (R-Br) would decompose to give a free radical R• in the presence of bipy and CuBr, which can be expressed as follows:

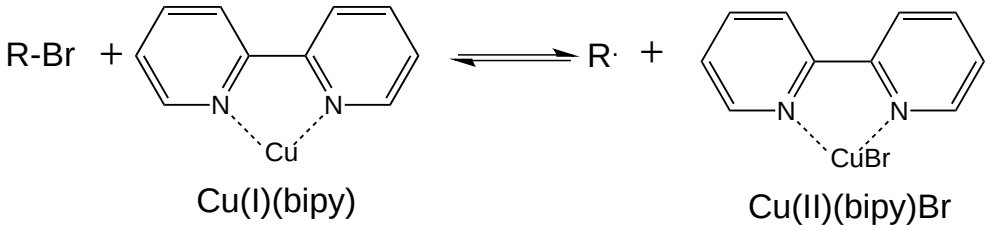

Initiation of a free radical chain takes place by addition of a free radical (R•) to a vinyl monomer (M). The propagation occurs via the addition of a new free radical (RM•) to another monomers, resulting the final polymers (P_n). Both processes can be formulated:

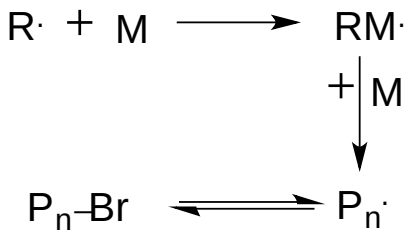

7.2.4 Immobilization of Biomolecules

The presence of epoxy group on PGMA polymer brush can react with amino-modified single-stranded DNA (ssDNA) via ring-opening reaction. PGMA@G on SiO_2/Si was used to immobilize an oligonucleotide. A 20-mer, 5'-amine-

modified oligonucleotide labeled with TFT in the 3' position was dissolved in 1× phosphate-buffered saline (PBS) (pH = 8) to prepare 300 nM solutions. PGMA@G was dropcast by the solution and placed overnight in a sealed beaker filled with saturated NaCl solution at room temperature. The unreacted oligonucleotides were washed away by PBS and DI water, respectively. Subsequently, the unreacted epoxy groups were blocked with ethanolamine and the immobilized ssDNA was hybridized with a TAMRA-labeled complementary oligonucleotide.

7.2.5 Material and Electrical Characterizations

Attenuated total reflectance-Fourier transform infrared spectroscopy (ATR-FTIR spectra, Varian 670-IR) was performed to measure the synthesized polymer brushes. The transmittance of polymer brushes@G films was performed by UV-Vis-NIR (Varian Cary 5000). The thickness and morphology was recorded by atomic force microscopy (AFM, Dimension icon with scan asyst, Bruker) in tapping mode under ambient condition with silicon tip (resonant frequency 320 kHz, spring constant 42 N/m). Raman spectra analysis was collected from Micro-Raman (WITec instruments Corp, Germany) with 532 nm laser. The Raman peak of Si at 520 cm^{-1} was used to calibrate the spectrometer. Optical images were acquired by using Optical microscopy (Scope A1, ZEISS, Germany). All the electrical performance of back-gate graphene FET and polymer brushes-functionalized graphene FET were carried out on a keithley 4200 semiconductor characterization system under vacuum conditions. Before measurement, each device was annealed at 100 ^{o}C for 1 h to remove water or solvents.

7.3 Results and Discussion

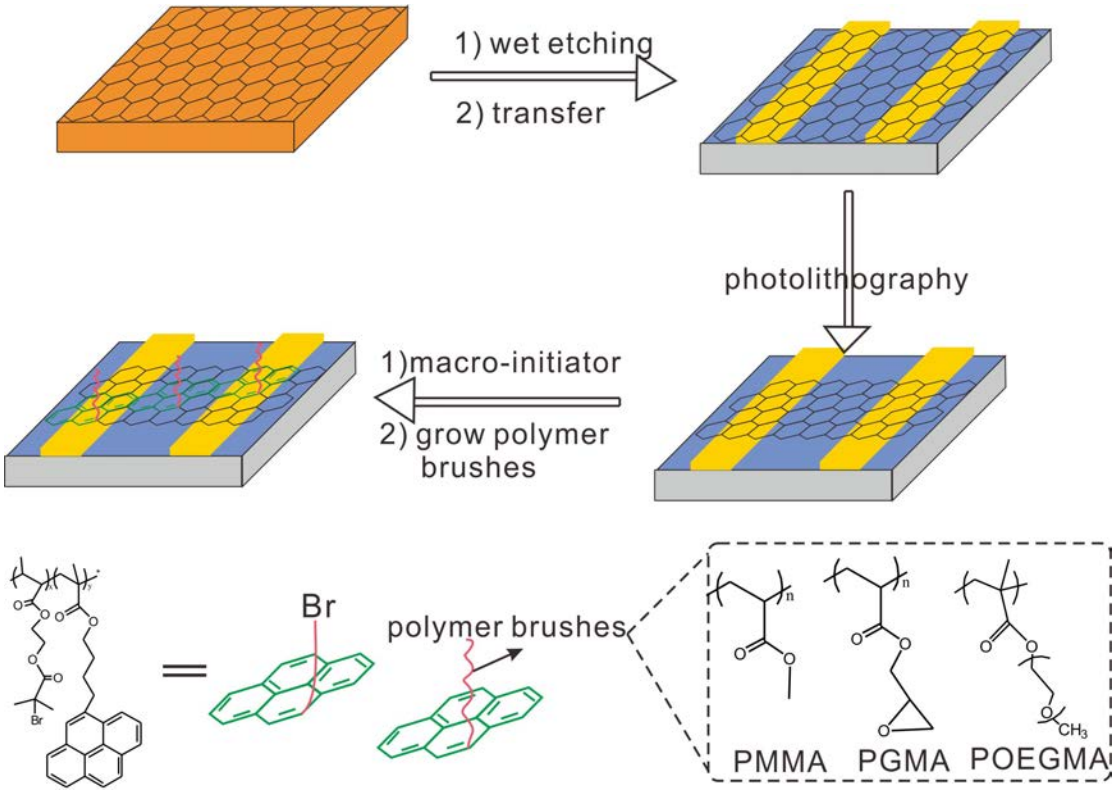

Figure 7.1. Schematic illustration of polymer brushes functionalized graphene FET.

Figure 7.1 schematically illustrates the fabrication process of graphene FET with functionalized polymer brushes. The process mainly contains three steps: CVD growth of monolayer graphene, wet transfer and patterning by photolithography, and growth of polymer brushes. Various polymer brushes such as PMMA, PGMA and POEGMA were decorated onto graphene surface via SI-ATRP.

7.3.1 Pristine Graphene-based FET

Figure 7.2a shows the optical image of patterned graphene film with a specific length and width of ~9.2 μm and ~3.8 μm. AFM was performed to characterize the topography and thickness of as-synthesized graphene. In Figure 7.2c, the line profile shows the thickness around 0.82 nm, which is consistent with the reported value of the monolayer graphene. Raman spectrum shows the characteristic peaks of graphene including D, G and 2D peaks, which are located at 1343, 1588 and 2683 cm^{-1}, respectively. The presence of D band with quite a low intensity indicates that there are little defects in graphene. Furthermore, the intensity of 2D

peak versus G peak (I_{2D}/I_G) around 2.12 and the sharp symmetric 2D peak also demonstrate that as-synthesized CVD graphene is single-layered and high quality (Figure 7.2d). The electrical performance of pristine graphene-based back-gate FET devices was characterized, as shown in Figure 7.2e and f. The ambipolar transfer characteristic of pristine graphene FET can be observed in Figure 2e. It exhibits a broad transition at the Dirac point (the minimum conductance) (~28 V) as the gate voltage scans from negative to positive and an ON/OFF ratio of ~3. The Dirac point represents the neutralization of positive and negative carriers, i.e. holes and electrons. In principle, graphene as an ambipolar material should have no free carriers at zero gate voltage. Therefore, the Dirac point of pristine graphene is expected to be around zero. However, due to the defects and contaminants induced in wet transfer, the as-made pristine graphene FET shows a positive shift, a p-type behavior. In Figure 2f, the output characteristics plotted between I_d versus V_{ds} are presented. The linear behavior indicates a good ohmic contact between the source/drain electrode and graphene sheet. As the gate voltage increased from -20 V to 20 V, the current I_{ds} flowed through p-type graphene decreased, therefore the resistance gradually increased.

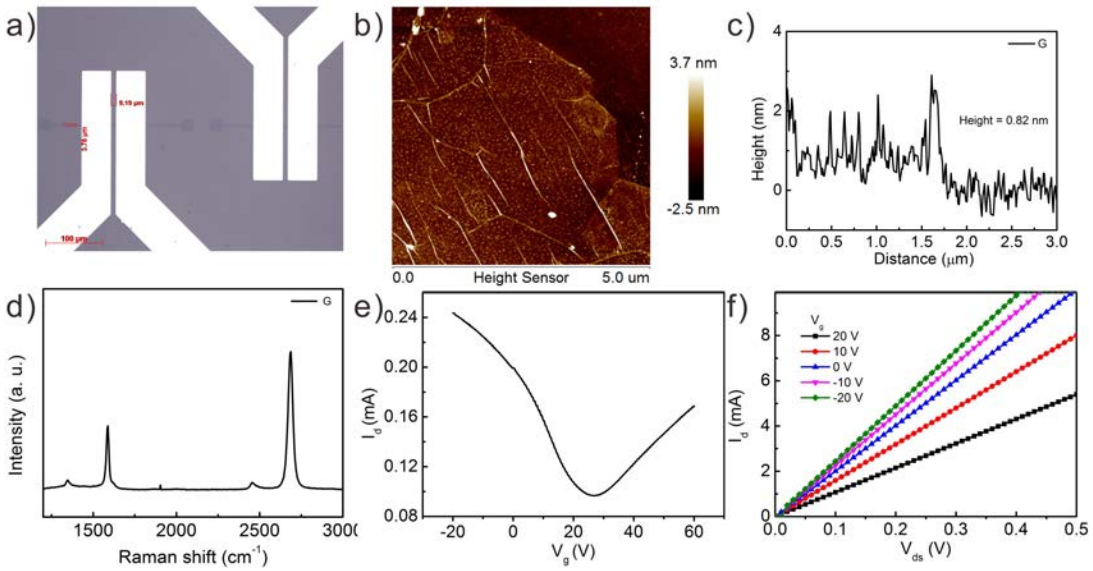

Figure 7.2. a) Optical image of patterned graphene with channel length ~9.2 μm and channel width ~3.8 μm. B) AFM image of monolayer graphene with a thickness of 0.82 nm c). d) Raman spectrum of graphene sheet. E) Transfer characteristics of graphene FET under 0.01 V bias voltage V_{ds}. F) Output characteristics with various gate voltages from 20 V to -20 V.

7.3.2 Polymer Brushes Functionalized Graphene

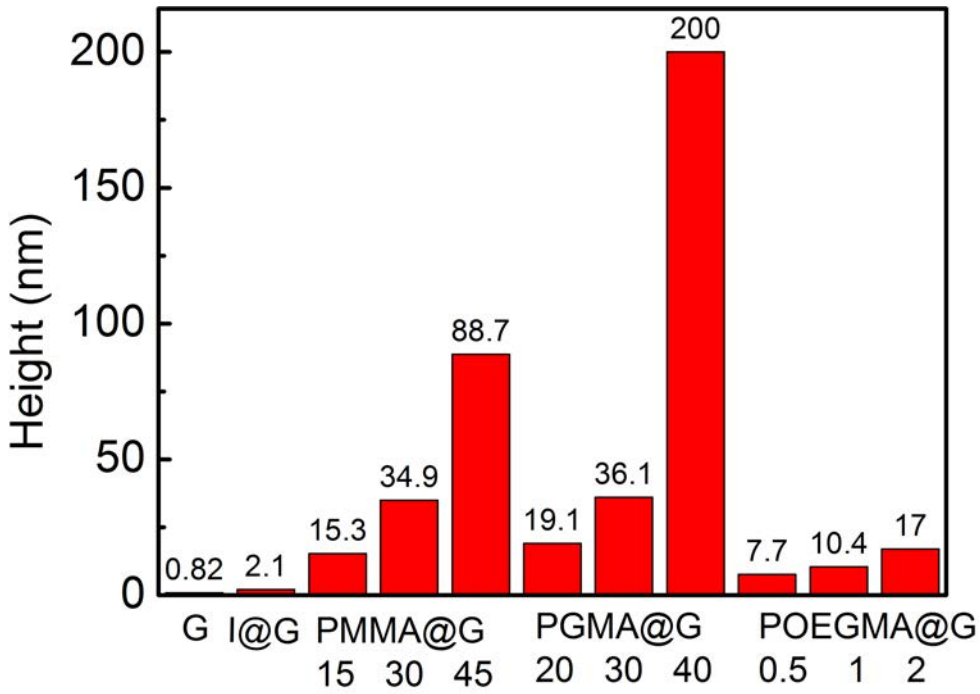

Figure 7.3. The height histogram of various graphene films including pristine graphene (G), initiator@G (i@G) and polymer brushes@G characterized by AFM.

AFM was employed to study the thicknesses of functionalized graphene films including I@G and various polymer brushes@G. Figure 7.3 shows the height distribution of various graphene films. The thickness of initiator-assembled graphene is ~2.1 nm. Note that the thickness of polymer brushes can be controlled in SI-ATRP reaction by monitoring the polymerization kinetics. Here we simply varied the polymerization time to control the thickness of polymer brushes. The thickness of all three types of polymer brushes shows a monotonic increase with prolonging the polymerization time. For PMMA brush, the thickness increased from 15.3 nm to 88.7 nm as the time increased from 15 min to 45 min. The thickness of PGMA brush ranged from 19.1 to ~200 nm corresponding to the reaction time from 20 min to 40 min. For POEGMA brush, the thickness didn't change much (7.7~17 nm) as the time increased from 0.5 h to 2 h.

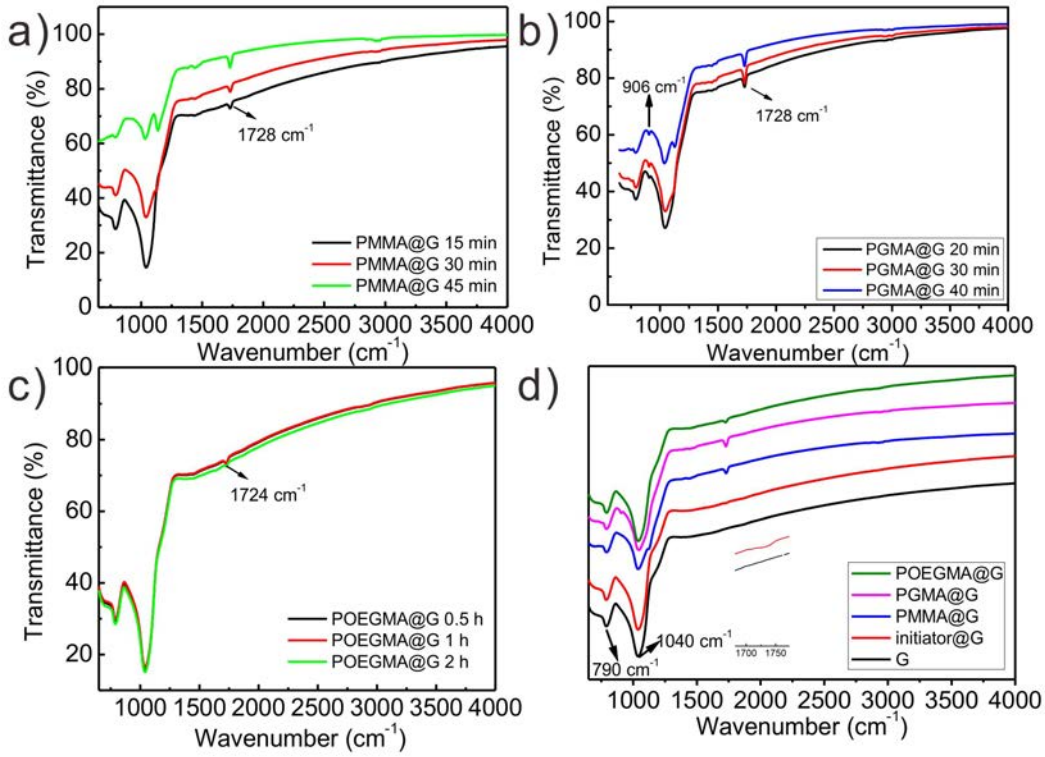

Figure 7.4. ATR-FITR spectra of three types of polymer brushes@G with various growth time: a) PMMA@G, b) PGMA@G, c) POEGMA@G. d) Inset is the enlarged spectra of graphene and initiator@G.

In addition, ATR-FTIR was carried out to identify the successful functionalization of graphene surface with macro-initiator and polymer brushes. The peaks located at ~790 cm^{-1} and 1040 cm^{-1} can be attributed to the out-of-plane C-H bending and in-plane C-H bending variations of aromatic ring, respectively. The feature peaks of C=O stretching at 1728 cm^{-1} (Figure 7.4a) and 1724 cm^{-1} (Figure 7.4c) are the evidence of successful grafting of PMMA and POEGMA brushes. For the PGMA brush, apart from the C=O stretching peak at 1728 cm^{-1}, another C-O stretching peak at 904 cm^{-1} can also prove the presence of PGMA brushes (Figure 7.4b). The inset spectra in Figure 7.5d shows a characteristic C=O stretching peak located at 1735 cm^{-1}, confirming the successful attachment of macro-initiator on graphene (initiator@G). For a specific polymer brush, prolonging the reaction time can help grow a thicker film. Take PMMA brush as an example. Thicker polymer brush may result in strong peak intensity in FTIR spectra. Therefore the characteristic peaks show a little variation as a function of reaction time.

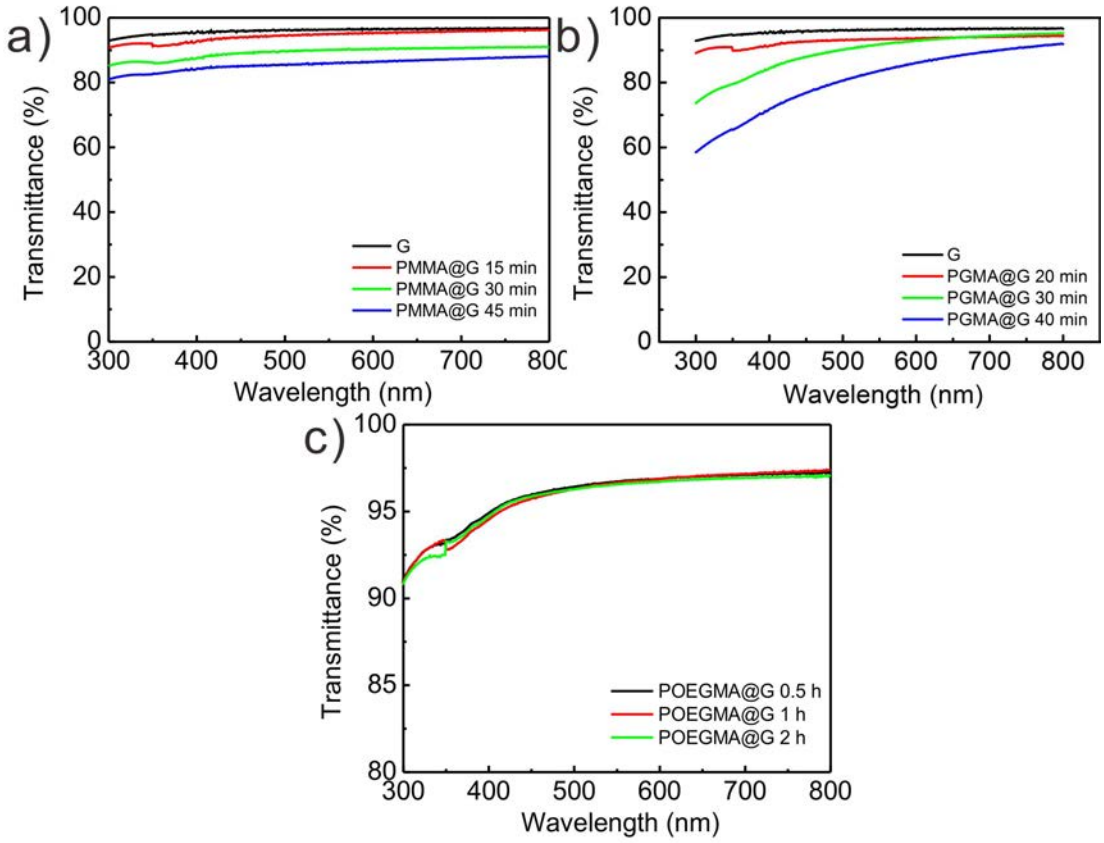

Figure 7.5. UV-Vis spectra of polymer brushes functionalized graphene, in which polymer brushes are grown for different time.

The graphene films after polymer brushes functionalization still maintain high transparency (Figure 7.5). For PMMA@G, the transmittance at 550 nm decreases from 94.9% to 85.9% as the brushes thickness increase from 15.3 nm to 88.7 nm. For PGMA@G, after 40 min polymerization, the transmittance is around 80% with a thickness of ~200 nm. For POEGMA@G, they have a high transmittance around 96%. This high value may derive from the very thin film obtained and non-uniform coverage of POEGMA brushes.

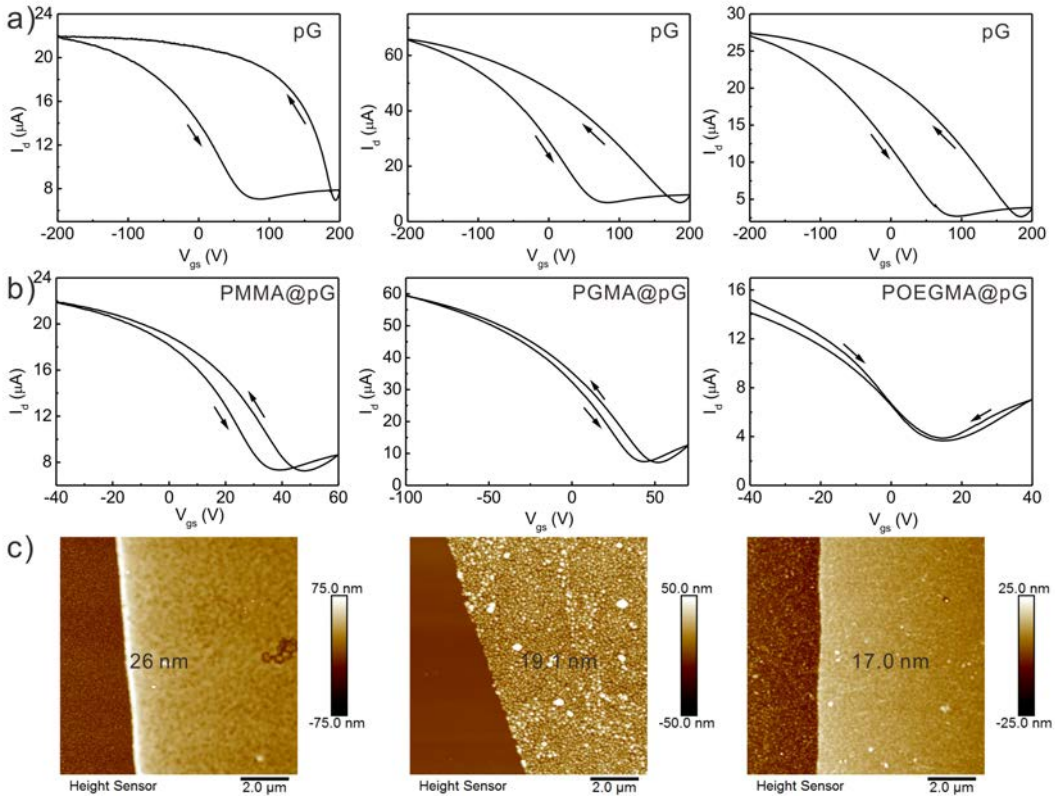

Figure 7.6. a) Transfer characteristics of patterned graphene (pG) FET under the bias of V_{ds} (0.05 V). b) The corresponding transfer characteristics of polymer brushes functionalized graphene FET: PMMA@pG, PGMA@pG and POEGMA@pG. c) The corresponding AFM topographic images of polymer brushes@pG with a thickness of 26nm, 19.1 nm and 17.0 nm for PMMA@pG, PGMA@pG and POEGMA@pG, respectively.

For each type of polymer brushes, various thicknesses were grown onto the graphene surface, and here we take the thickness around ~20 nm for an example to study the electrical performance of polymer brushes@pG, as shown in Figure 7.6. For the pG, we can observe that the Dirac point has a large positive shift, which is mainly caused by the residues left in the photolithography. This can be avoided or minimized by controlling the photolithographic conditions or using proper organic solvents to conduct post-treatment process. For PMMA@pG FET, its Dirac point shifts to the negative direction compared to that of the same device before the polymer growth. As is the case for PGMA@pG and POEGMA@pG. Based on the phenomena observed above, we can assume that the presence of polymer brushes can donate electrons to graphene film which

makes the majority carriers (hole) become less and leads to the n-type doping effect. This result is consistent with the literature reported.[342] All the FET devices in Figure 7.6a and b show an obvious hysteresis as the gate voltage scans forward and reverse. Such a phenomenon can be attributed to the trapping and de-trapping of charge carriers absorbed by water molecules or trapped on dielectric substrate.[343]

Moreover, charge carriers' mobility is another important parameter to evaluate the performance of graphene FET devices. The mobility can be estimated using the equation:

$$\mu = \frac{L}{WC_iV_{ds}} \times \frac{dI_{ds}}{dV_{gs}}$$

where L is the channel length, W is the channel width, C_i is the unit-area capacitance of bottom gate oxide ($C_i = \varepsilon_0\varepsilon_r/d$; $\varepsilon_0 = 8.854 \times 10^{-12}$ F/m, $\varepsilon_r(SiO_2) = 3.9$, $d(SiO_2) = 300$ nm). Table 1 shows the hole and electron mobility and Dirac point of as-fabricated FET devices based on the pristine patterned graphene and various polymer brushes decorated graphene. Interestingly, compared with the pristine graphene, the electron mobility of polymer brushes decorated graphene increased.

Table 7.1. Summary of mobility and Dirac point of as-fabricated FET devices.

FET devices	Hole ($cm^2V^{-1}s^{-1}$)	Electron ($cm^2V^{-1}s^{-1}$)	Dirac point (V)
pG	813	207	~80
PMMA@pG	961.2 (425.5)	173.3 (86)	39
PGMA@pG	1888.1 (950.3)	579.8 (117)	43
POEGMA@pG	1163 (454.9)	523.2 (53.3)	15

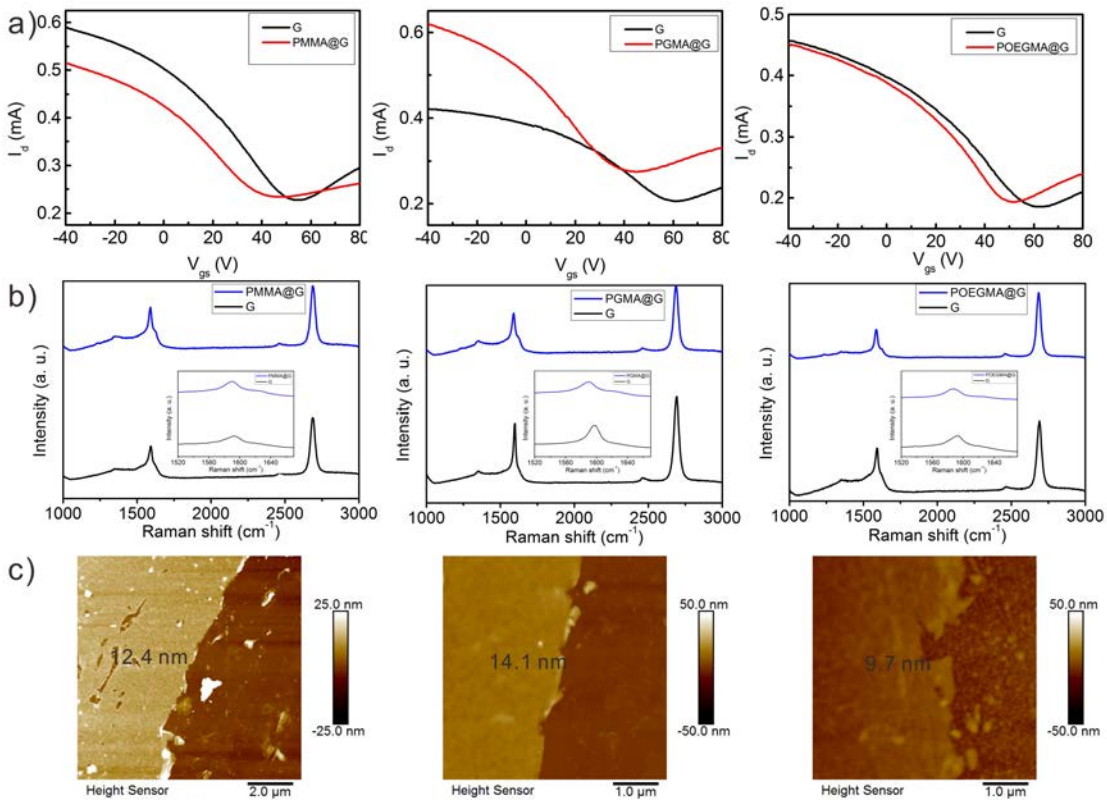

Figure 7.7. a) Transfer characteristics of FET devices based on graphene (G, without pattern) and polymer brushes@G under the bias of V_{ds} (0.01V). b) Raman spectra of graphene and polymer brushes@G. Insets are the Raman spectra with magnified G peaks. c) The corresponding AFM topographic images of polymer brushes@G.

As a matter of fact, it is the Dirac point that plays an important role in the determination of the function of polymer brushes. The absence of photolithographic patterning would impose a negative effect on the calculation of charge carrier mobility but a negligible effect on the Dirac point shift. Therefore, our fabrication process of FET devices can be simplified by directly growing the polymer brushes on the surface of wet transferred graphene film. Figure 7.7a shows a negative shift of Dirac point after the growth of polymer brushes, which is consistent with the result of polymer brushes@pG. This further confirms the n-type doping effect of polymer brushes. Micro-Raman was also performed to the graphene films at different stages. Figure 7.7b shows the Raman spectra of graphene before and after growth of polymer brushes. The small D peak indicates that there are no additional defects induced in the ATRP process. And the red shift of G peak after the functionalization of polymer brushes may be also

closely related to the n-doping effect. AFM image shows the topography and thickness of polymer brushes@G: PMMA@G 12.4 nm, PGMA@G 14.1 nm and POEGMA@G 9.7 nm.

7.3.3 Immobilization of Biomolecules

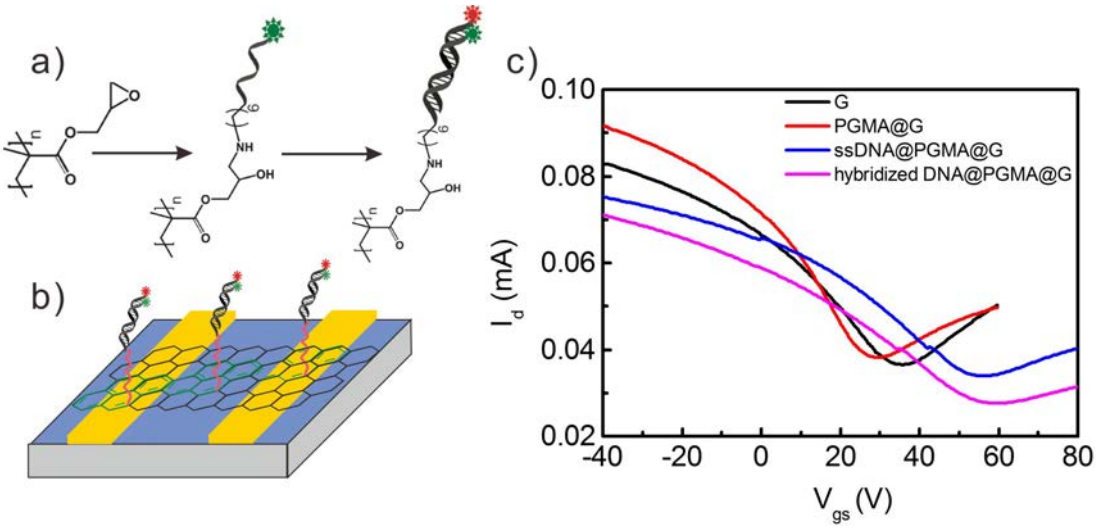

Figure 7.8. a) Illustration of molecular reaction for DNA binding and hybridization. b) Immobilization of DNA molecules on PGMA@G FET device. c) The transfer characteristics of polymer functionalized graphene FET and biomolecules-immobilized graphene FET under a bias V_{ds} of 0.01 V.

For a proof-of-concept application, the polymer brushes functionalized graphene may serve as a platform to immobilize biomolecules, such as DNA molecules. Figure 7.8a and b show the immobilization process of DNA molecules. The presence of epoxy group in PGMA can react with amino-modified ssDNA via ring-opening reaction. Subsequently ssDNA can hybridized with its complementary strand. After reaction, the devices were annealed at 100 ^{o}C under vacuum condition for 2 h. Figure 7.8c shows the electrical performance. Same as the aforementioned, the presence of PGMA induces an n-type doping effect with a negative shift of the Dirac point in contrast with the pristine graphene. After the immobilization of ssDNA, we can clearly observe an obvious positive shift of Dirac point, which indicates the p-type doping behavior. The subsequent hybridization of DNA moves the Dirac point a little to the positive direction. This result is a little contradictory to the literature, which claims that DNA has an

n-doping effect.[331] It may be reasonable because in our case the DNA is not directly deposited onto the graphene surface but with an intermediate polymer brush layer. The detailed electronic reaction between polymer brushes and DNA molecules in not clear yet.

7.4 Conclusions

The electrical performances of monolayer graphene-based FET devices with the functionalization of various polymer brushes have been carefully studied. Compared to the pristine graphene-based devices, the presence of polymer brushes including PMMA, PGMA and POEGMA shifts the Dirac point to the negative direction, exhibiting an n-type doping effect. Moreover, the electron mobility of polymer brushes@G is increased in contrast with pristine graphene while the hole mobility is decreased. Importantly, the polymer brushes modified graphene can serve as a scaffold to immobilize and sense biomolecules. It seems that a p-type doping effect is induced after immobilization of DNA molecules. This research exhibit facile synthetic processes in the functionalization of graphene with various polymer brushes and the immobilization of biomolecules meanwhile the resultant devices shows apparent variations in the electrical performance, whereas the precise mechanism of their interaction and theoretical model are still under research with our great efforts, and this obscurity restricts the enhancement and optimization of the targeted immobilization and sensing effect in terms of selectivity and sensitivity.

CHAPTER 8 CONCLUSIONS AND SUGGESTIONS FOR FUTURE WORK

8.1 Conclusions

In this thesis, our developed synthetic method, namely "salt-assisted direct exfoliation method" is systematically studied to produce 2D nanomaterials including graphene and various TMD nanosheets. Typical characterization techniques are performed to investigate the morphology, thickness and quality of as-exfoliated nanosheets. These 2D nanomaterials are solution cast into thin films or hybrid films and subsequently integrated into photovoltaic devices. Moreover, CVD graphene has been synthesized so that we can use it to study the electrical performance of polymer brushes functionalized graphene.

In chapter 4, the salt-assisted direct exfoliation method was first proposed to prepare single- and few-layered graphene nanosheets. We assume that the presence of inorganic salts can attenuate the van der Waals force, which is responsible for bounding the layers together, probably by penetrating salt ions into the interlayers and this could facilitate the subsequent ultrasonic exfoliation. Though we attempted to interpret this process, no concrete proof can be provided. However, the results turned out to be good. 86% of as-produced graphene sheets are few layers. TEM and Raman measurement confirmed the good quality of graphene sheets with crystalline structure and little defects in the basal plane. They can be steadily dispersed in water, which is convenient to prepare thin films by solution-processed approaches.

In chapter 5, the conductivity of graphene thin films prepared by using as-produced graphene solutions was dramatically improved by combination with 1D Ag NWs. The graphene/Ag NW hybrid film shows a sheet resistance of ~130 Ω sq^{-1} and a transmittance of 70%. It can be potentially used as transparent electrodes. After the integration into perovskite solar cells as cathode, the device showed a PCE around 5.3%.

In chapter 6, this salt-assisted exfoliation method was extended to prepare other 2D nanomaterials. Single- and few-layered TMD 2D nanosheets were obtained. Similarly, the statistical analysis from AFM indicated that 65% TMD nanosheets were 1~5 layers. As-produced MoS_2 nanosheets were integrated into OSCs as HTL. MoS_2 thin films were fabricated via solution-processed methods including vacuum filtration method and drop casting. The V_{oc} of OSCs was remarkably improved from 0.34 V to 0.58 V.

In chapter 7, monolayer graphene was synthesized by CVD method. The electrical performance of graphene-based transistors with/without the functionalization by polymer brushes were carefully studied. The pristine graphene showed ambipolar characteristic with Dirac point ~28 V, p-type doped. The polymer brushes@G shows an n-type doping behavior because the Dirac point shifts to the negative direction compared to the pristine graphene devices. The electrical performance after the immobilization of biomolecules (e.g. DNA) was also investigated, exhibiting p-type doping effect, which is uncertain at this stage.

8.2 Suggestions for Future Work

This research project has focused on the synthetic methods to produce 2D nanomaterials, e.g. graphene and TMD nanosheets and explore some applications, particularly in the photovoltaic aspects. Although we have developed a liquid-based direct exfoliation method to produce 2D nanosheets and achieved some results, there are still some concerns that need to be addressed in the future work.

1. For the salt-assisted exfoliation we proposed, although it is demonstrated to be an effective way to produce 2D nanomaterials compared to the direct ultrasonic exfoliation in liquids, we failed to figure out the mechanism. Some experiments have been done, but the results are not solid enough to help us draw a conclusion. The intermediate process is worthy for further investigation.

2. The combination of 2D graphene nanosheets with 1D metal NWs are promising to serve as the flexible transparent electrodes. Because metal NWs can improve the conductivity while graphene nanosheets can provide better mechanical property. The flexible photovoltaic devices could be studied later.

3. Polymer brushes functionalized graphene can be a scaffold or platform to construct biosensors because it offers multi-functionality to immobilize biomolecules. For the biosensors, the selectivity and sensitivity are the crucial factors to consider.

Reference

[1] K. S. Novoselov, A. K. Geim, S. V. Morozov, D. Jiang, Y. Zhang, S. V. Dubonos, I. V. Grigorieva, A. A. Firsov, Science 2004, 306, 666.

[2] A. K. Geim, K. S. Novoselov, Nat Mater 2007, 6, 183.

[3] V. Nicolosi, M. Chhowalla, M. G. Kanatzidis, M. S. Strano, J. N. Coleman, Science 2013, 340, 1420.

[4] C. C. Coleman, H. Goldwhite, W. Tikkanen, Chem Mater 1998, 10, 2794.

[5] R. Z. Ma, T. Sasaki, Adv Mater 2010, 22, 5082.

[6] M. Naguib, M. Kurtoglu, V. Presser, J. Lu, J. J. Niu, M. Heon, L. Hultman, Y. Gogotsi, M. W. Barsoum, Adv Mater 2011, 23, 4248.

[7] H. Zhang, ACS Nano 2015, 10.1021/acsnano.5b05040.

[8] A. A. Balandin, S. Ghosh, W. Z. Bao, I. Calizo, D. Teweldebrhan, F. Miao, C. N. Lau, Nano Lett 2008, 8, 902.

[9] C. Lee, X. Wei, J. W. Kysar, J. Hone, Science 2008, 321, 385.

[10] R. R. Nair, P. Blake, A. N. Grigorenko, K. S. Novoselov, T. J. Booth, T. Stauber, N. M. R. Peres, A. K. Geim, Science 2008, 320, 1308.

[11] A. K. Geim, K. S. Novoselov, Nat Mater 2007, 6, 183.

[12] X. Huang, Z. Y. Yin, S. X. Wu, X. Y. Qi, Q. Y. He, Q. C. Zhang, Q. Y. Yan, F. Boey, H. Zhang, Small 2011, 7, 1876.

[13] Y. W. Zhu, S. Murali, W. W. Cai, X. S. Li, J. W. Suk, J. R. Potts, R. S. Ruoff, Adv Mater 2010, 22, 5226.

[14] K. S. Novoselov, V. I. Fal'ko, L. Colombo, P. R. Gellert, M. G. Schwab, K. Kim, Nature 2012, 490, 192.

[15] L. Britnell, R. V. Gorbachev, R. Jalil, B. D. Belle, F. Schedin, A. Mishchenko, T. Georgiou, M. I. Katsnelson, L. Eaves, S. V. Morozov, N. M. R. Peres, J. Leist, A. K. Geim, K. S. Novoselov, L. A. Ponomarenko, Science 2012, 335, 947.

[16] Y. Q. Wu, K. A. Jenkins, A. Valdes-Garcia, D. B. Farmer, Y. Zhu, A. A. Bol, C. Dimitrakopoulos, W. J. Zhu, F. N. Xia, P. Avouris, Y. M. Lin, Nano Lett 2012, 12, 3062.

[17] X. L. Li, X. R. Wang, L. Zhang, S. W. Lee, H. J. Dai, Science 2008, 319, 1229.

[18] M. Y. Han, B. Ozyilmaz, Y. B. Zhang, P. Kim, Phys Rev Lett 2007, 98.

[19] R. Balog, B. Jorgensen, L. Nilsson, M. Andersen, E. Rienks, M. Bianchi, M. Fanetti, E. Laegsgaard, A. Baraldi, S. Lizzit, Z. Sljivancanin, F. Besenbacher, B. Hammer, T. G. Pedersen, P. Hofmann, L. Hornekaer, Nat Mater 2010, 9, 315.

[20] J. H. Li, L. Y. Niu, Z. J. Zheng, F. Yan, Adv Mater 2014, 26, 5239.

[21] B. Sensale-Rodriguez, T. Fang, R. S. Yan, M. M. Kelly, D. Jena, L. Liu, H. L. Xing, Appl Phys Lett 2011, 99.

[22] B. Radisavljevic, A. Radenovic, J. Brivio, V. Giacometti, A. Kis, Nat Nanotechnol 2011, 6, 147.

[23] Y. Ding, Y. L. Wang, J. Ni, L. Shi, S. Q. Shi, W. H. Tang, Physica B 2011, 406, 2254.

[24] J. A. Wilson, A. D. Yoffe, Adv. Phys. 1969, 18, 193.

[25] M. Chhowalla, H. S. Shin, G. Eda, L. J. Li, K. P. Loh, H. Zhang, Nat Chem 2013, 5, 263.

[26] K. V. Emtsev, A. Bostwick, K. Horn, J. Jobst, G. L. Kellogg, L. Ley, J. L. McChesney, T. Ohta, S. A. Reshanov, J. Rohrl, E. Rotenberg, A. K. Schmid, D. Waldmann, H. B. Weber, T. Seyller, Nat Mater 2009, 8, 203.

[27] C. Berger, Z. M. Song, X. B. Li, X. S. Wu, N. Brown, C. Naud, D. Mayou, T. B. Li, J. Hass, A. N. Marchenkov, E. H. Conrad, P. N. First, W. A. de Heer, Science 2006, 312, 1191.

[28] V. Y. Aristov, G. Urbanik, K. Kummer, D. V. Vyalikh, O. V. Molodtsova, A. B. Preobrajenski, A. A. Zakharov, C. Hess, T. Hanke, B. Buchner, I. Vobornik, J. Fujii, G. Panaccione, Y. A. Ossipyan, M. Knupfer, Nano Lett 2010, 10, 992.

[29] J. D. Caldwell, T. J. Anderson, J. C. Culbertson, G. G. Jernigan, K. D. Hobart, F. J. Kub, M. J. Tadjer, J. L. Tedesco, J. K. Hite, M. A. Mastro, R. L. Myers-Ward, C. R. Eddy, P. M. Campbell, D. K. Gaskill, ACS Nano 2010, 4, 1108.

[30] S. Unarunotai, Y. Murata, C. E. Chialvo, H. S. Kim, S. MacLaren, N. Mason, I. Petrov, J. A. Rogers, Appl Phys Lett 2009, 95.

[31] Y. J. Zhan, Z. Liu, S. Najmaei, P. M. Ajayan, J. Lou, Small 2012, 8, 966.

[32] R. Van Noorden, Nature 2012, 483, S32.

[33] W. W. Liu, J. N. Wang, Chem Commun 2011, 47, 6888.

[34] Z. Z. Sun, Z. Yan, J. Yao, E. Beitler, Y. Zhu, J. M. Tour, Nature 2010, 468, 549.

[35] A. Guermoune, T. Chari, F. Popescu, S. S. Sabri, J. Guillemette, H. S. Skulason, T. Szkopek, M. Siaj, Carbon 2011, 49, 4204.

[36] X. Li, C. W. Magnuson, A. Venugopal, R. M. Tromp, J. B. Hannon, E. M. Vogel, L. Colombo, R. S. Ruoff, J Am Chem Soc 2011, 133, 2816.

[37] Y. Gamo, A. Nagashima, M. Wakabayashi, M. Terai, C. Oshima, Surf Sci 1997, 374, 61.

[38] H. Ueta, M. Saida, C. Nakai, Y. Yamada, M. Sasaki, S. Yamamoto, Surf Sci 2004, 560, 183.

[39] S. Marchini, S. Gunther, J. Wintterlin, Phys Rev B 2007, 76, 075429.

[40] J. Coraux, A. T. N'Diaye, C. Busse, T. Michely, Nano Lett 2008, 8, 565.

[41] S. Bae, H. Kim, Y. Lee, X. F. Xu, J. S. Park, Y. Zheng, J. Balakrishnan, T. Lei, H. R. Kim, Y. I. Song, Y. J. Kim, K. S. Kim, B. Ozyilmaz, J. H. Ahn, B. H. Hong, S. Iijima, Nat Nanotechnol 2010, 5, 574.

[42] K. K. Liu, W. J. Zhang, Y. H. Lee, Y. C. Lin, M. T. Chang, C. Su, C. S. Chang, H. Li, Y. M. Shi, H. Zhang, C. S. Lai, L. J. Li, Nano Lett 2012, 12, 1538.

[43] Y. H. Lee, X. Q. Zhang, W. J. Zhang, M. T. Chang, C. T Lin, Kai Di Chang, Ya Chu Yu, Jacob Tse Wei Wang, Chia Seng Chang, Lain Jong Li, T. W. Lin, Adv. Mater. 2012, 24, 2320.

[44] S. Balendhran, J. Z. Ou, M. Bhaskaran, S. Sriram, S. Ippolito, Z. Vasic, E. Kats, S. Bhargava, S. Zhuiykov, K. Kalantar-zadeh, Nanoscale 2012, 4, 461.

[45] Y. C. Lin, W. J. Zhang, J. K. Huang, K. K. Liu, Y. H. Lee, C. T. Liang, C. W. Chu, L. J. Li, Nanoscale 2012, 4, 6637.

[46] X. L. Wang, Y. J. Gong, G. Shi, W. L. Chow, K. Keyshar, G. L. Ye, R. Vajtai, J. Lou, Z. Liu, E. Ringe, B. K. Tay, P. M. Ajayan, ACS Nano 2014, 8, 5125.

[47] M. Okada, T. Sawazaki, K. Watanabe, T. Taniguch, H. Hibino, H. Shinohara, R. Kitaura, ACS Nano 2014, 8, 8273.

[48] Y. Zhang, Y. F. Zhang, Q. Q. Ji, J. Ju, H. T. Yuan, J. P. Shi, T. Gao, D. L. Ma, M. X. Liu, Y. B. Chen, X. J. Song, H. Y. Hwang, Y. Cui, Z. F. Liu, ACS Nano 2013, 7, 8963.

[49] J. K. Huang, J. Pu, C. L. Hsu, M. H. Chiu, Z. Y. Juang, Y. H. Chang, W. H. Chang, Y. Iwasa, T. Takenobu, L. J. Li, ACS Nano 2014, 8, 923.

[50] B. L. Liu, M. Fathi, L. Chen, A. Abbas, Y. Q. Ma, C. W. Zhou, ACS Nano 2015, 9, 6119.

[51] X. K. Lu, M. F. Yu, H. Huang, R. S. Ruoff, Nanotechnology 1999, 10, 269.

[52] Y. B. Zhang, J. P. Small, W. V. Pontius, P. Kim, Appl Phys Lett 2005, 86, 073104.

[53] K. S. Novoselov, D. Jiang, F. Schedin, T. J. Booth, V. V. Khotkevich, S. V. Morozov, A. K. Geim, P Natl Acad Sci USA 2005, 102, 10451.

[54] C. Lee, H. Yan, L. E. Brus, T. F. Heinz, J. Hone, S. Ryu, ACS Nano 2010, 4, 2695.

[55] K. F. Mak, C. Lee, J. Hone, J. Shan, T. F. Heinz, Phys Rev Lett 2010, 105.

[56] M. M. Benameur, B. Radisavljevic, J. S. Heron, S. Sahoo, H. Berger, A. Kis, Nanotechnology 2011, 22.

[57] H. Li, G. Lu, Z. Y. Yin, Q. Y. He, H. Li, Q. Zhang, H. Zhang, Small 2012, 8, 682.

[58] L. Staudenmaier, Berichte der deutschen chemischen Gesellschaft 1898, 31, 1481.

[59] WILLIAMS. HUMMERS, JR., RICHARDE.OFFEMA, Journal of American Chemical Society 1958, 1339.

[60] S. Stankovich, R. D. Piner, X. Q. Chen, N. Q. Wu, S. T. Nguyen, R. S. Ruoff, J Mater Chem 2006, 16, 155.

[61] I. Jung, M. Pelton, R. Piner, D. A. Dikin, S. Stankovich, S. Watcharotone, M. Hausner, R. S. Ruoff, Nano Lett 2007, 7, 3569.

[62] Y. X. Liu, X. C. Dong, P. Chen, Chem Soc Rev 2012, 41, 2283.

[63] L. M. Dai, Accounts Chem Res 2013, 46, 31.

[64] Yanwu Zhu, Meryl D. Stoller, Weiwei Cai, Aruna Velamakanni, Richard D. Piner, David Chen, R. S. Ruoff, ACS Nano 2010, 4, 1227.

[65] S. Stankovich, D. A. Dikin, R. D. Piner, K. A. Kohlhaas, A. Kleinhammes, Y. Jia, Y. Wu, S. T. Nguyen, R. S. Ruoff, Carbon 2007, 45, 1558.

[66] H. J. Shin, K. K. Kim, A. Benayad, S. M. Yoon, H. K. Park, I. S. Jung, M. H. Jin, H. K. Jeong, J. M. Kim, J. Y. Choi, Y. H. Lee, Adv Funct Mater 2009, 19, 1987.

[67] H. X. Chang, G. F. Wang, A. Yang, X. M. Tao, X. Q. Liu, Y. D. Shen, Z. J. Zheng, Adv Funct Mater 2010, 20, 2893.

[68] Y. L. Zhang, L. Guo, H. Xia, Q. D. Chen, J. Feng, H. B. Sun, Adv Opt Mater 2014, 2, 10.

[69] H. A. Becerril, J. Mao, Z. Liu, R. M. Stoltenberg, Z. Bao, Y. Chen, ACS Nano 2008, 2, 463.

[70] T. J. Mason, J. Phillip, Applied sonochemistry 2002.

[71] J. N. Israelachvili, Academic press 2011, revised 3rd edition.

[72] P. Blake, P. D. Brimicombe, R. R. Nair, T. J. Booth, D. Jiang, F. Schedin, L. A. Ponomarenko, S. V. Morozov, H. F. Gleeson, E. W. Hill, A. K. Geim, K. S. Novoselov, Nano Lett 2008, 8, 1704.

[73] Y. Hernandez, V. Nicolosi, M. Lotya, F. M. Blighe, Z. Y. Sun, S. De, I. T. McGovern, B. Holland, M. Byrne, Y. K. Gun'ko, J. J. Boland, P. Niraj, G. Duesberg, S. Krishnamurthy, R. Goodhue, J. Hutchison, V. Scardaci, A. C. Ferrari, J. N. Coleman, Nat Nanotechnol 2008, 3, 563.

[74] C. E. Hamilton, J. R. Lomeda, Z. Z. Sun, J. M. Tour, A. R. Barron, Nano Lett 2009, 9, 3460.

[75] A. B. Bourlinos, V. Georgakilas, R. Zboril, T. A. Steriotis, A. K. Stubos, Small 2009, 5, 1841.

[76] U. Khan, A. O'Neill, M. Lotya, S. De, J. N. Coleman, Small 2010, 6, 864.

[77] E. Y. Choi, W. S. Choi, Y. B. Lee, Y. Y. Noh, Nanotechnology 2011, 22.

[78] A. O'neill, U. Khan, P. N. Nirmalraj, J. Boland, J. N. Coleman, J Phys Chem C 2011, 115, 5422.

[79] W. Qian, R. Hao, Y. L. Hou, Y. Tian, C. M. Shen, H. J. Gao, X. L. Liang, Nano Res 2009, 2, 706.

[80] J. N. Coleman, M. Lotya, A. O'Neill, S. D. Bergin, P. J. King, U. Khan, K. Young, A. Gaucher, S. De, R. J. Smith, I. V. Shvets, S. K. Arora, G. Stanton, H. Y. Kim, K. Lee, G. Kim, G. S. Duesberg, T. Hallam, J. J. Boland, J. J. Wang, J. F. Donegan, J. C. Grunlan, G. Moriarty, A. Shmeliov, R. J. Nicholls, J. M. Perkins, E. M. Grieveson, K. Theuwissen, D. W. McComb, P. D. Nellist, V. Nicolosi, Science 2011, 331, 568.

[81] G. Cunningham, M. Lotya, C. S. Cucinotta, S. Sanvito, S. D. Bergin, R. Menzel, M. S. P. Shaffer, J. N. Coleman, ACS Nano 2012, 6, 3468.

[82] A. O'neill, U. Khan, J. N. Coleman, Chem Mater 2012, 24, 2414.

[83] J. M. Yun, Y. J. Noh, C. H. Lee, S. I. Na, S. Lee, S. M. Jo, H. I. Joh, D. Y. Kim, Small 2014, 10.1002/smll.201303648.

[84] L. Dong, S. Lin, L. Yang, J. J. Zhang, C. Yang, D. Yang, H. B. Lu, Chem Commun 2014, 50, 15936.

[85] M. Lotya, Y. Hernandez, P. J. King, R. J. Smith, V. Nicolosi, L. S. Karlsson, F. M. Blighe, S. De, Z. M. Wang, I. T. McGovern, G. S. Duesberg, J. N. Coleman, J Am Chem Soc 2009, 131, 3611.

[86] M. Lotya, P. J. King, U. Khan, S. De, J. N. Coleman, ACS Nano 2010, 4, 3155.

[87] T. Hasan, F. Torrisi, Z. Sun, D. Popa, V. Nicolosi, G. Privitera, F. Bonaccorso, A. C. Ferrari, Phys Status Solidi B 2010, 247, 2953.

[88] S. Vadukumpully, J. Paul, S. Valiyaveettil, Carbon 2009, 47, 3288.

[89] R. J. Smith, P. J. King, M. Lotya, C. Wirtz, U. Khan, S. De, A. O'Neill, G. S. Duesberg, J. C. Grunlan, G. Moriarty, J. Chen, J. Z. Wang, A. I. Minett, V. Nicolosi, J. N. Coleman, Adv Mater 2011, 23, 3944.

[90] L. Guardia, M. J. Fernandez-Merino, J. I. Paredes, P. Solis-Fernandez, S. Villar-Rodil, A. Martinez-Alonso, J. M. D. Tascon, Carbon 2011, 49, 1653.

[91] R. J. Smith, M. Lotya, J. N. Coleman, New J Phys 2010, 12.

[92] F. Liu, J. Y. Choi, T. S. Seo, Chem Commun 2010, 46, 2844.

[93] Z. Y. Yin, S. Y. Sun, T. Salim, S. X. Wu, X. A. Huang, Q. Y. He, Y. M. Lam, H. Zhang, ACS Nano 2010, 4, 5263.

[94] D. W. Lee, T. Kim, M. Lee, Chem Commun 2011, 47, 8259.

[95] D. Parviz, S. Das, H. S. T. Ahmed, F. Irin, S. Bhattacharia, M. J. Green, ACS Nano 2012, 6, 8857.

[96] A. Schlierf, H. F. Yang, E. Gebremedhn, E. Treossi, L. Ortolani, L. P. Chen, A. Minoia, V. Morandi, P. Samori, C. Casiraghi, D. Beljonne, V. Palermo, Nanoscale 2013, 5, 4205.

[97] H. Yang, Y. Hernandez, A. Schlierf, A. Felten, A. Eckmann, S. Johal, P. Louette, J. J. Pireaux, X. Feng, K. Muellen, V. Palermo, C. Casiraghi, Carbon 2013, 53, 357.

[98] J. H. Jang, D. Rangappa, Y. U. Kwon, I. Honma, J Mater Chem 2011, 21, 3462.

[99] X. C. Dong, Y. M. Shi, Y. Zhao, D. M. Chen, J. Ye, Y. G. Yao, F. Gao, Z. H. Ni, T. Yu, Z. X. Shen, Y. X. Huang, P. Chen, L. J. Li, Phys Rev Lett 2009, 102.

[100] X. Zhou, T. Wu, K. Ding, B. Hu, M. Hou, B. Han, Chem Commun (Camb) 2010, 46, 386.

[101] X. Q. Wang, P. F. Fulvio, G. A. Baker, G. M. Veith, R. R. Unocic, S. M. Mahurin, M. F. Chi, S. Dai, Chem Commun 2010, 46, 4487.

[102] D. Nuvoli, L. Valentini, V. Alzari, S. Scognamillo, S. B. Bon, M. Piccinini, J. Illescas, A. Mariani, J Mater Chem 2011, 21, 3428.

[103] P. Joensen, R. F. Frindt, S. R. Morrison, Mater Res Bull 1986, 21, 457.

[104] R. Bissessur, M. G. Kanatzidis, J. L. Schindler, C. R. Kannewurf, J Chem Soc Chem Comm 1993, 1582.

[105] R. A. Gordon, D. Yang, E. D. Crozier, D. T. Jiang, R. F. Frindt, Phys Rev B 2002, 65.

[106] C. Y. Su, A. Y. Lu, Y. P. Xu, F. R. Chen, A. N. Khlobystov, L. J. Li, ACS Nano 2011, 5, 2332.

[107] K. Parvez, R. J. Li, S. R. Puniredd, Y. Hernandez, F. Hinkel, S. H. Wang, X. L. Feng, K. Mullen, ACS Nano 2013, 7, 3598.

[108] K. Parvez, Z. S. Wu, R. J. Li, X. J. Liu, R. Graf, X. L. Feng, K. Mullen, J Am Chem Soc 2014, 136, 6083.

[109] N. Liu, P. Kim, J. H. Kim, J. H. Ye, S. Kim, C. J. Lee, ACS Nano 2014, 8, 6902.

[110] G. X. Wang, B. Wang, J. Park, Y. Wang, B. Sun, J. Yao, Carbon 2009, 47, 3242.

[111] N. Liu, F. Luo, H. X. Wu, Y. H. Liu, C. Zhang, J. Chen, Adv Funct Mater 2008, 18, 1518.

[112] J. Lu, J. X. Yang, J. Z. Wang, A. L. Lim, S. Wang, K. P. Loh, ACS Nano 2009, 3, 2367.

[113] Z. Y. Zeng, Z. Y. Yin, X. Huang, H. Li, Q. Y. He, G. Lu, F. Boey, H. Zhang, Angew Chem Int Edit 2011, 50, 11093.

[114] Z. Y. Zeng, T. Sun, J. X. Zhu, X. Huang, Z. Y. Yin, G. Lu, Z. X. Fan, Q. Y. Yan, H. H. Hng, H. Zhang, Angew Chem Int Edit 2012, 51, 9052.

[115] X. Rocquefelte, F. Boucher, P. Gressier, G. Ouvrard, P. Blaha, K. Schwarz, Phys Rev B 2000, 62, 2397.

[116] Q. H. Wang, K. Kalantar-Zadeh, A. Kis, J. N. Coleman, M. S. Strano, Nat Nanotechnol 2012, 7, 699.

[117] Aruna Zhamu, Jinjun Shin, Jiusheng Guo, B. Z. Jang, US patent 2012, Appl. No.: 11/787,442.

[118] L. R. Bunnell, , Kennewick, Wash, US patent 1993, App1.No.: 791,864.

[119] D. W. Murphy, G. W. Hull, J Chem Phys 1975, 62, 973.

[120] K. R. Paton, E. Varrla, C. Backes, R. J. Smith, U. Khan, A. O'Neill, C. Boland, M. Lotya, O. M. Istrate, P. King, T. Higgins, S. Barwich, P. May, P. Puczkarski, I. Ahmed, M. Moebius, H. Pettersson, E. Long, J. Coelho, S. E. O'Brien, E. K. McGuire, B. M. Sanchez, G. S. Duesberg, N. McEvoy, T. J. Pennycook, C. Downing, A. Crossley, V. Nicolosi, J. N. Coleman, Nat Mater 2014, 13, 624.

[121] S. Park, J. H. An, I. W. Jung, R. D. Piner, S. J. An, X. S. Li, A. Velamakanni, R. S. Ruoff, Nano Lett 2009, 9, 1593.

[122] S. Park, J. H. An, R. D. Piner, I. Jung, D. X. Yang, A. Velamakanni, S. T. Nguyen, R. S. Ruoff, Chem Mater 2008, 20, 6592.

[123] J. Choi, K. J. Kim, B. Kim, H. Lee, S. Kim, J Phys Chem C 2009, 113, 9433.

[124] Y. Zhu, A. L. Higginbotham, J. M. Tour, Chem Mater 2009, 21, 5284.

[125] A. J. Patil, J. L. Vickery, T. B. Scott, S. Mann, Adv Mater 2009, 21, 3159.

[126] J. B. Liu, S. H. Fu, B. Yuan, Y. L. Li, Z. X. Deng, J Am Chem Soc 2010, 132, 7279.

[127] X. Huang, X. Z. Zhou, S. X. Wu, Y. Y. Wei, X. Y. Qi, J. Zhang, F. Boey, H. Zhang, Small 2010, 6, 513.

[128] K. Jasuja, V. Berry, ACS Nano 2009, 3, 2358.

[129] R. Muszynski, B. Seger, P. V. Kamat, J Phys Chem C 2008, 112, 5263.

[130] C. Xu, X. Wang, J. W. Zhu, J Phys Chem C 2008, 112, 19841.

[131] N. Li, Z. Y. Wang, K. K. Zhao, Z. J. Shi, S. K. Xu, Z. N. Gu, J Nanosci Nanotechno 2010, 10, 6748.

[132] H. L. Wang, H. S. Casalongue, Y. Y. Liang, H. J. Dai, J Am Chem Soc 2010, 132, 7472.

[133] H. M. A. Hassan, V. Abdelsayed, A. E. R. S. Khder, K. M. AbouZeid, J. Terner, M. S. El-Shall, S. I. Al-Resayes, A. A. El-Azhary, J Mater Chem 2009, 19, 3832.

[134] I. N. Kholmanov, C. W. Magnuson, A. E. Aliev, H. F. Li, B. Zhang, J. W. Suk, L. L. Zhang, E. Peng, S. H. Mousavi, A. B. Khanikaev, R. Piner, G. Shvets, R. S. Ruoff, Nano Lett 2012, 12, 5679.

[135] J. Liang, H. Bi, D. Y. Wan, F. Q. Huang, Adv Funct Mater 2012, 22, 1267.

[136] Jian Chen, Hui Bi, Shengrui Sun, Yufeng Tang, Wei Zhao, Tianquan Lin, Dongyun Wan, Fuqiang Huang, Xiaodong Zhou, Xiaoming Xie, M. Jiang, ACS Appl Mater Interfaces 2013, 5, 1408.

[137] S. J. Guo, D. Wen, Y. M. Zhai, S. J. Dong, E. K. Wang, ACS Nano 2010, 4, 3959.

[138] S. J. Guo, S. J. Dong, E. K. Wang, ACS Nano 2010, 4, 547.

[139] G. Goncalves, P. A. A. P. Marques, C. M. Granadeiro, H. I. S. Nogueira, M. K. Singh, J. Gracio, Chem Mater 2009, 21, 4796.

[140] Y. K. Kim, H. K. Na, Y. W. Lee, H. Jang, S. W. Han, D. H. Min, Chem Commun 2010, 46, 3185.

[141] X. Z. Zhou, X. Huang, X. Y. Qi, S. X. Wu, C. Xue, F. Y. C. Boey, Q. Y. Yan, P. Chen, H. Zhang, J Phys Chem C 2009, 113, 10842.

[142] H. Q. Zhou, C. Y. Qiu, F. Yu, H. C. Yang, M. J. Chen, L. J. Hu, L. F. Sun, J Phys Chem C 2011, 115, 11348.

[143] O. Akhavan, M. Abdolahad, A. Esfandiar, M. Mohatashamifar, J Phys Chem C 2010, 114, 12955.

[144] G. Williams, B. Seger, P. V. Kamat, ACS Nano 2008, 2, 1487.

[145] Y. H. Zhang, Z. R. Tang, X. Z. Fu, Y. J. Xu, ACS Nano 2010, 4, 7303.

[146] J. A. Lin, M. Penchev, G. P. Wang, R. K. Paul, J. B. Zhong, X. Y. Jing, M. Ozkan, C. S. Ozkan, Small 2010, 6, 2448.

[147] X. J. Liu, L. K. Pan, T. Lv, T. Lu, G. Zhu, Z. Sun, C. Q. Sun, Catal Sci Technol 2011, 1, 1189.

[148] P. Kumar, L. S. Panchakarla, S. V. Bhat, U. Maitra, K. S. Subrahmanyam, C. N. R. Rao, Nanotechnology 2010, 21, 385701.

[149] S. J. Ding, D. Y. Luan, F. Y. C. Boey, J. S. Chen, X. W. Lou, Chem Commun 2011, 47, 7155.

[150] L. S. Zhang, L. Y. Jiang, H. J. Yan, W. D. Wang, W. Wang, W. G. Song, Y. G. Guo, L. J. Wan, J Mater Chem 2010, 20, 5462.

[151] J. Yan, Z. J. Fan, T. Wei, W. Z. Qian, M. L. Zhang, F. Wei, Carbon 2010, 48, 3825.

[152] S. Chen, J. W. Zhu, X. D. Wu, Q. F. Han, X. Wang, ACS Nano 2010, 4, 2822.

[153] Z. S. Wu, W. C. Ren, L. Wen, L. B. Gao, J. P. Zhao, Z. P. Chen, G. M. Zhou, F. Li, H. M. Cheng, ACS Nano 2010, 4, 3187.

[154] H. Kim, D. H. Seo, S. W. Kim, J. Kim, K. Kang, Carbon 2011, 49, 326.

[155] Y. T. Kim, J. H. Han, B. H. Hong, Y. U. Kwon, Adv Mater 2010, 22, 515.

[156] X. R. Zhang, S. G. Li, X. Jin, S. S. Zhang, Chem Commun 2011, 47, 4929.

[157] M. Steenackers, A. M. Gigler, N. Zhang, F. Deubel, M. Seifert, L. H. Hess, C. H. Y. X. Lim, K. P. Loh, J. A. Garrido, R. Jordan, M. Stutzmann, I. D. Sharp, J Am Chem Soc 2011, 133, 10490.

[158] M. Seifert, A. H. R. Koch, F. Deubel, T. Simmet, L. H. Hess, M. Stutzmann, R. Jordan, J. A. Garrido, I. D. Sharp, Chem Mater 2013, 25, 466.

[159] Y. X. Xu, W. J. Hong, H. Bai, C. Li, G. Q. Shi, Carbon 2009, 47, 3538.

[160] Q. Wu, Y. X. Xu, Z. Y. Yao, A. R. Liu, G. Q. Shi, ACS Nano 2010, 4, 1963.

[161] A. Dasari, Z. Z. Yu, Y. W. Mai, Polymer 2009, 50, 4112.

[162] R. Verdejo, F. Barroso-Bujans, M. A. Rodriguez-Perez, J. A. de Saja, M. A. Lopez-Manchado, J Mater Chem 2008, 18, 2221.

[163] J. Yan, T. Wei, B. Shao, Z. J. Fan, W. Z. Qian, M. L. Zhang, F. Wei, Carbon 2010, 48, 487.

[164] S. Wang, B. M. Goh, K. K. Manga, Q. L. Bao, P. Yang, K. P. Loh, ACS Nano 2010, 4, 6180.

[165] T. H. Han, W. J. Lee, D. H. Lee, J. E. Kim, E. Y. Choi, S. O. Kim, Adv Mater 2010, 22, 2060.

[166] M. Jahan, Q. L. Bao, J. X. Yang, K. P. Loh, J Am Chem Soc 2010, 132, 14487.

[167] C. H. Lu, H. H. Yang, C. L. Zhu, X. Chen, G. N. Chen, Angew Chem Int Edit 2009, 48, 4785.

[168] Y. Wang, Z. H. Li, D. H. Hu, C. T. Lin, J. H. Li, Y. H. Lin, J Am Chem Soc 2010, 132, 9274.

[169] V. C. Tung, L. M. Chen, M. J. Allen, J. K. Wassei, K. Nelson, R. B. Kaner, Y. Yang, Nano Lett 2009, 9, 1949.

[170] E. Yoo, J. Kim, E. Hosono, H. Zhou, T. Kudo, I. Honma, Nano Lett 2008, 8, 2277.

[171] Z. J. Fan, J. Yan, L. J. Zhi, Q. Zhang, T. Wei, J. Feng, M. L. Zhang, W. Z. Qian, F. Wei, Adv Mater 2010, 22, 3723.

[172] Y. Cao, S. Liu, Q. Shen, K. Yan, P. J. Li, J. Xu, D. P. Yu, M. L. Steigerwald, C. Nuckolls, Z. F. Liu, X. F. Guo, Adv Funct Mater 2009, 19, 2743.

[173] S. P. Pang, H. N. Tsao, X. L. Feng, K. Mullen, Adv Mater 2009, 21, 3488.

[174] D. B. Farmer, H. Y. Chiu, Y. M. Lin, K. A. Jenkins, F. N. Xia, P. Avouris, Nano Lett 2009, 9, 4474.

[175] F. N. Xia, D. B. Farmer, Y. M. Lin, P. Avouris, Nano Lett 2010, 10, 715.

[176] Y. Q. Wu, Y. M. Lin, A. A. Bol, K. A. Jenkins, F. N. Xia, D. B. Farmer, Y. Zhu, P. Avouris, Nature 2011, 472, 74.

[177] F. Schwierz, Nat Nanotechnol 2010, 5, 487.

[178] T. Kobayashi, N. Kimura, J. B. Chi, S. Hirata, D. Hobara, Small 2010, 6, 1210.

[179] J. Yan, T. Wei, B. Shao, F. Q. Ma, Z. J. Fan, M. L. Zhang, C. Zheng, Y. C. Shang, W. Z. Qian, F. Wei, Carbon 2010, 48, 1731.

[180] S. R. C. Vivekchand, C. S. Rout, K. S. Subrahmanyam, A. Govindaraj, C. N. R. Rao, J Chem Sci 2008, 120, 9.

[181] J. Q. Liu, Z. Y. Yin, X. H. Cao, F. Zhao, A. P. Lin, L. H. Xie, Q. L. Fan, F. Boey, H. Zhang, W. Huang, ACS Nano 2010, 4, 3987.

[182] S. Myung, J. Park, H. Lee, K. S. Kim, S. Hong, Adv Mater 2010, 22, 2045.

[183] X. D. Zhuang, Y. Chen, G. Liu, P. P. Li, C. X. Zhu, E. T. Kang, K. G. Neoh, B. Zhang, J. H. Zhu, Y. X. Li, Adv Mater 2010, 22, 1731.

[184] T. W. Kim, Y. Gao, O. Acton, H. L. Yip, H. Ma, H. Z. Chen, A. K. Y. Jen, Appl Phys Lett 2010, 97, 023310.

[185] J. Q. Liu, Z. Q. Lin, T. J. Liu, Z. Y. Yin, X. Z. Zhou, S. F. Chen, L. H. Xie, F. Boey, H. Zhang, W. Huang, Small 2010, 6, 1536.

[186] X. Huang, Z. Y. Zeng, H. Zhang, Chem Soc Rev 2013, 42, 1934.

[187] X. M. Geng, W. Wu, N. Li, W. W. Sun, J. Armstrong, A. Al-hilo, M. Brozak, J. B. Cui, T. P. Chen, Adv Funct Mater 2014, 24, 6123.

[188] W. J. Zhou, K. Zhou, D. M. Hou, X. J. Liu, G. Q. Li, Y. H. Sang, H. Liu, L. G. Li, S. W. Chen, Acs Appl Mater Inter 2014, 6, 21534.

[189] Q. Y. He, S. X. Wu, Z. Y. Yin, H. Zhang, Chem. Sci. 2012, 3, 1764.

[190] L. Huang, Y. Huang, J. J. Liang, X. J. Wan, Y. S. Chen, Nano Res 2011, 4, 675.

[191] Y. Zhang, B. Zheng, C. F. Zhu, X. Zhang, C. L. Tan, H. Li, B. Chen, J. Yang, J. Z. Chen, Y. Huang, L. H. Wang, H. Zhang, Adv Mater 2015, 27, 935.

[192] J. B. Wu, H. A. Becerril, Z. N. Bao, Z. F. Liu, Y. S. Chen, P. Peumans, Appl Phys Lett 2008, 92, 263302.

[193] X. Wang, L. J. Zhi, K. Mullen, Nano Lett 2008, 8, 323.

[194] X. Gu, W. Cui, H. Li, Z. W. Wu, Z. Y. Zeng, S. T. Lee, H. Zhang, B. Q. Sun, Adv Energy Mater 2013, 3, 1262.

[195] B. Lei, G. R. Li, X. P. Gao, J Mater Chem A 2014, 2, 3919.

[196] J. M. Yun, Y. J. Noh, J. S. Yeo, Y. J. Go, S. I. Na, H. G. Jeong, J. Kim, S. Lee, S. S. Kim, H. Y. Koo, T. W. Kim, D. Y. Kim, J Mater Chem C 2013, 1, 3777.

[197] X. Gu, W. Cui, T. Song, C. H. Liu, X. Z. Shi, S. D. Wang, B. Q. Sun, Chemsuschem 2014, 7, 416.

[198] Z. Y. Yin, J. X. Zhu, Q. Y. He, X. H. Cao, C. L. Tan, H. Y. Chen, Q. Y. Yan, H. Zhang, Adv Energy Mater 2014, 4.

[199] L. Y. Niu, K. Li, H. Y. Zhen, Y. S. Chui, W. J. Zhang, F. Yan, Z. J. Zheng, Small 2014, 10, 4651.

[200] Y. Wang, S. W. Tong, X. F. Xu, B. Ozyilmaz, K. P. Loh, Adv Mater 2011, 23, 1514.

[201] J. Liu, G. H. Kim, Y. H. Xue, J. Y. Kim, J. B. Baek, M. Durstock, L. M. Dai, Adv Mater 2014, 26, 786.

[202] X. Yang, W. F. Fu, W. Q. Liu, J. H. Hong, Y. Cai, C. H. Jin, M. S. Xu, H. B. Wang, D. R. Yang, H. Z. Chen, J Mater Chem A 2014, 2, 7727.

[203] W. Q. Liu, X. Yang, Y. Y. Zhang, M. S. Xu, H. Z. Chen, Rsc Adv 2014, 4, 32744.

[204] Zhike Liu, Shu Ping Lau, F. Yan, Chem. Soc. Rev. 2015, 44, 5638.

[205] Z. C. Wu, Z. H. Chen, X. Du, J. M. Logan, J. Sippel, M. Nikolou, K. Kamaras, J. R. Reynolds, D. B. Tanner, A. F. Hebard, A. G. Rinzler, Science 2004, 305, 1273.

[206] A. D. Pasquier, H. E. Unalan, A. Kanwal, S. Miller, M. Chhowalla, Appl Phys Lett 2005, 87.

[207] H. Z. Geng, K. K. Kim, K. P. So, Y. S. Lee, Y. Chang, Y. H. Lee, J Am Chem Soc 2007, 129, 7758.

[208] M. G. Kang, M. S. Kim, J. S. Kim, L. J. Guo, Adv Mater 2008, 20, 4408.

[209] S. H. Ahn, L. J. Guo, Nano Lett 2010, 10, 4228.

[210] S. De, T. M. Higgins, P. E. Lyons, E. M. Doherty, P. N. Nirmalraj, W. J. Blau, J. J. Boland, J. N. Coleman, ACS Nano 2009, 3, 1767.

[211] J. Y. Lee, S. T. Connor, Y. Cui, P. Peumans, Nano Lett 2008, 8, 689.

[212] S. I. Na, S. S. Kim, J. Jo, D. Y. Kim, Adv Mater 2008, 20, 4061.

[213] S. Kirchmeyer, K. Reuter, J Mater Chem 2005, 15, 2077.

[214] Y. Zhu, Z. Z. Sun, Z. Yan, Z. Jin, J. M. Tour, ACS Nano 2011, 5, 6472.

[215] C. W. Jeong, P. Nair, M. Khan, M. Lundstrom, M. A. Alam, Nano Lett 2011, 11, 5020.

[216] J. van de Lagemaat, T. M. Barnes, G. Rumbles, S. E. Shaheen, T. J. Coutts, C. Weeks, I. Levitsky, J. Peltola, P. Glatkowski, Appl Phys Lett 2006, 88.

[217] M. Song, D. S. You, K. Lim, S. Park, S. Jung, C. S. Kim, D. H. Kim, D. G. Kim, J. K. Kim, J. Park, Y. C. Kang, J. Heo, S. H. Jin, J. H. Park, J. W. Kang, Adv Funct Mater 2013, 23, 4177.

[218] W. F. Zhang, B. F. Zhao, Z. C. He, X. M. Zhao, H. T. Wang, S. F. Yang, H. B. Wu, Y. Cao, Energ Environ Sci 2013, 6, 1956.

[219] A. Kasry, M. A. Kuroda, G. J. Martyna, G. S. Tulevski, A. A. Bol, ACS Nano 2010, 4, 3839.

[220] S. F. Pei, J. P. Zhao, J. H. Du, W. C. Ren, H. M. Cheng, Carbon 2010, 48, 4466.

[221] Y. J. Yu, Y. Zhao, S. Ryu, L. E. Brus, K. S. Kim, P. Kim, Nano Lett 2009, 9, 3430.

[222] G. Giovannetti, P. A. Khomyakov, G. Brocks, V. M. Karpan, J. van den Brink, P. J. Kelly, Phys Rev Lett 2008, 101.

[223] Y. Wang, X. H. Chen, Y. L. Zhong, F. R. Zhu, K. P. Loh, Appl Phys Lett 2009, 95.

[224] H. Park, J. A. Rowehl, K. K. Kim, V. Bulovic, J. Kong, Nanotechnology 2010, 21.

[225] H. Park, R. M. Howden, M. C. Barr, V. Bulovic, K. Gleason, J. Kong, ACS Nano 2012, 6, 6370.

[226] H. Park, S. Chang, M. Smith, S. Gradecak, J. Kong, Sci Rep-Uk 2013, 3.

[227] H. Park, Y. M. Shi, J. Kong, Nanoscale 2013, 5, 8934.

[228] H. Park, J. Kong, Adv Energy Mater 2014, 4.

[229] S. Lee, J. S. Yeo, Y. Ji, C. Cho, D. Y. Kim, S. I. Na, B. H. Lee, T. Lee, Nanotechnology 2012, 23.

[230] Z. K. Liu, J. H. Li, F. Yan, Adv Mater 2013, 25, 4296.

[231] Z. K. Liu, J. H. Li, Z. H. Sun, G. A. Tai, S. P. Lau, F. Yan, ACS Nano 2012, 6, 810.

[232] P. You, Z. K. Liu, Q. D. Tai, S. H. Liu, F. Yan, Adv Mater 2015, 27, 3632.

[233] Q. Su, S. P. Pang, V. Alijani, C. Li, X. L. Feng, K. Mullen, Adv Mater 2009, 21, 3191.

[234] Z. Jin, J. Yao, C. Kittrell, J. M. Tour, ACS Nano 2011, 5, 4112.

[235] B. D. Guo, Q. A. Liu, E. D. Chen, H. W. Zhu, L. A. Fang, J. R. Gong, Nano Lett 2010, 10, 4975.

[236] K. C. Kwon, K. S. Choi, B. J. Kim, J. L. Lee, S. Y. Kim, J Phys Chem C 2012, 116, 26586.

[237] J. H. Huang, J. H. Fang, C. C. Liu, C. W. Chu, ACS Nano 2011, 5, 6262.

[238] Y. H. Zhou, C. Fuentes-Hernandez, J. Shim, J. Meyer, A. J. Giordano, H. Li, P. Winget, T. Papadopoulos, H. Cheun, J. Kim, M. Fenoll, A. Dindar, W. Haske, E. Najafabadi, T. M. Khan, H. Sojoudi, S. Barlow, S. Graham, J. L. Bredas, S. R. Marder, A. Kahn, B. Kippelen, Science 2012, 336, 327.

[239] G. Jo, S. I. Na, S. H. Oh, S. Lee, T. S. Kim, G. Wang, M. Choe, W. Park, J. Yoon, D. Y. Kim, Y. H. Kahng, T. Lee, Appl Phys Lett 2010, 97.

[240] D. Zhang, F. X. Xie, P. Lin, W. C. H. Choy, ACS Nano 2013, 7, 1740.

[241] X. J. Wan, G. K. Long, L. Huang, Y. S. Chen, Adv Mater 2011, 23, 5342.

[242] Z. C. He, C. M. Zhong, S. J. Su, M. Xu, H. B. Wu, Y. Cao, Nat Photonics 2012, 6, 591.

[243] M. D. Irwin, B. Buchholz, A. W. Hains, R. P. H. Chang, T. J. Marks, P Natl Acad Sci USA 2008, 105, 2783.

[244] V. Shrotriya, G. Li, Y. Yao, C. W. Chu, Y. Yang, Appl Phys Lett 2006, 88.

[245] J. M. Yun, J. S. Yeo, J. Kim, H. G. Jeong, D. Y. Kim, Y. J. Noh, S. S. Kim, B. C. Ku, S. I. Na, Adv Mater 2011, 23, 4923.

[246] S. S. Li, K. H. Tu, C. C. Lin, C. W. Chen, M. Chhowalla, ACS Nano 2010, 4, 3169.

[247] M. M. Li, W. Ni, B. Kan, X. J. Wan, L. Zhang, Q. Zhang, G. K. Long, Y. Zuo, Y. S. Chen, Phys Chem Chem Phys 2013, 15, 18973.

[248] C. T. G. Smith, R. W. Rhodes, M. J. Beliatis, K. D. G. I. Jayawardena, L. J. Rozanski, C. A. Mills, S. R. P. Silva, Appl Phys Lett 2014, 105.

[249] I. P. Murray, S. J. Lou, L. J. Cote, S. Loser, C. J. Kadleck, T. Xu, J. M. Szarko, B. S. Rolczynski, J. E. Johns, J. X. Huang, L. P. Yu, L. X. Chen, T. J. Marks, M. C. Hersam, J Phys Chem Lett 2011, 2, 3006.

[250] J. S. Yeo, J. M. Yun, Y. S. Jung, D. Y. Kim, Y. J. Noh, S. S. Kim, S. I. Na, J Mater Chem A 2014, 2, 292.

[251] J. Kim, V. C. Tung, J. X. Huang, Adv Energy Mater 2011, 1, 1052.

[252] J. C. Yu, J. I. Jang, B. R. Lee, G. W. Lee, J. T. Han, M. H. Song, Acs Appl Mater Inter 2014, 6, 2067.

[253] Y. H. Chao, J. S. Wu, C. E. Wu, J. F. Jheng, C. L. Wang, C. S. Hsu, Adv Energy Mater 2013, 3, 1279.

[254] K. D. G. I. Jayawardena, R. Rhodes, K. K. Gandhi, M. R. R. Prabhath, G. D. M. R. Dabera, M. J. Beliatis, L. J. Rozanski, S. J. Henley, S. R. P. Silva, J Mater Chem A 2013, 1, 9922.

[255] J. Liu, Y. H. Xue, Y. X. Gao, D. S. Yu, M. Durstock, L. M. Dai, Adv Mater 2012, 24, 2228.

[256] M. J. Beliatis, K. K. Gandhi, L. J. Rozanski, R. Rhodes, L. McCafferty, M. R. Alenezi, A. S. Alshammari, C. A. Mills, K. D. G. I. Jayawardena, S. J. Henley, S. R. P. Silva, Adv Mater 2014, 26, 2078.

[257] Q. V. Le, T. P. Nguyen, S. Y. Kim, Phys Status Solidi-R 2014, 8, 390.

[258] Q. V. Le, T. P. Nguyen, K. S. Choi, Y. H. Cho, Y. J. Hong, S. Y. Kim, Phys Chem Chem Phys 2014, 16, 25468.

[259] Z. F. Liu, Q. Liu, Y. Huang, Y. F. Ma, S. G. Yin, X. Y. Zhang, W. Sun, Y. S. Chen, Adv Mater 2008, 20, 3924.

[260] Y. Li, Y. Hu, Y. Zhao, G. Q. Shi, L. E. Deng, Y. B. Hou, L. T. Qu, Adv Mater 2011, 23, 776.

[261] D. S. Yu, Y. Yang, M. Durstock, J. B. Baek, L. M. Dai, ACS Nano 2010, 4, 5633.

[262] D. S. Yu, K. Park, M. Durstock, L. M. Dai, J Phys Chem Lett 2011, 2, 1113.

[263] T. Mahmoudi, W. Y. Rho, H. Y. Yang, S. R. P. Silva, Y. B. Hahn, Chem Commun 2014, 50, 8705.

[264] X. S. Li, W. W. Cai, J. H. An, S. Kim, J. Nah, D. X. Yang, R. Piner, A. Velamakanni, I. Jung, E. Tutuc, S. K. Banerjee, L. Colombo, R. S. Ruoff, Science 2009, 324, 1312.

[265] Y. Zhang, L. Y. Zhang, C. W. Zhou, Accounts Chem Res 2013, 46, 2329.

[266] C. Liu, K. Wang, P. C. Du, C. Yi, T. Y. Meng, X. Gong, Adv Energy Mater 2015, 5.

[267] Q. Y. He, S. X. Wu, S. Gao, X. H. Cao, Z. Y. Yin, H. Li, P. Chen, H. Zhang, ACS Nano 2011, 5, 5038.

[268] S. De, J. N. Coleman, ACS Nano 2010, 4, 2713.

[269] F. Bonaccorso, Z. Sun, T. Hasan, A. C. Ferrari, Nat Photonics 2010, 4, 611.

[270] M. J. Allen, V. C. Tung, R. B. Kaner, Chem Rev 2010, 110, 132.

[271] X. H. Cao, Y. M. Shi, W. H. Shi, G. Lu, X. Huang, Q. Y. Yan, Q. C. Zhang, H. Zhang, Small 2011, 7, 3163.

[272] X. Huang, X. Y. Qi, F. Boey, H. Zhang, Chem Soc Rev 2012, 41, 666.

[273] J. L. Xia, F. Chen, J. H. Li, N. J. Tao, Nat Nanotechnol 2009, 4, 505.

[274] W. J. Yu, S. H. Chae, S. Y. Lee, D. L. Duong, Y. H. Lee, Adv Mater 2011, 23, 1889.

[275] B. Li, X. H. Cao, H. G. Ong, J. W. Cheah, X. Z. Zhou, Z. Y. Yin, H. Li, J. L. Wang, F. Boey, W. Huang, H. Zhang, Adv Mater 2010, 22, 3058.

[276] S. Stankovich, D. A. Dikin, G. H. B. Dommett, K. M. Kohlhaas, E. J. Zimney, E. A. Stach, R. D. Piner, S. T. Nguyen, R. S. Ruoff, Nature 2006, 442, 282.

[277] H. X. Chang, Z. H. Sun, Q. H. Yuan, F. Ding, X. M. Tao, F. Yan, Z. J. Zheng, Adv Mater 2010, 22, 4872.

[278] X. Huang, Z. Zeng, Z. Fan, J. Liu, H. Zhang, Adv Mater 2012.

[279] X. Y. Qi, C. L. Tan, J. Wei, H. Zhang, Nanoscale 2013, 5, 1440.

[280] C. L. Tan, X. Huang, H. Zhang, Mater Today 2013, 16, 29.

[281] S. X. Wu, Q. Y. He, C. L. Tan, Y. D. Wang, H. Zhang, Small 2013, 9, 1160.

[282] G. P. Keeley, A. O'Neill, N. McEvoy, N. Peltekis, J. N. Coleman, G. S. Duesberg, J Mater Chem 2010, 20, 7864.

[283] D. Li, M. B. Muller, S. Gilje, R. B. Kaner, G. G. Wallace, Nat Nanotechnol 2008, 3, 101.

[284] J. Coraux, A. T. N'Diaye, M. Engler, C. Busse, D. Wall, N. Buckanie, F. J. M. Z. Heringdorf, R. van Gastel, B. Poelsema, T. Michely, New J Phys 2009, 11, 023006.

[285] A. Reina, X. T. Jia, J. Ho, D. Nezich, H. B. Son, V. Bulovic, M. S. Dresselhaus, J. Kong, Nano Lett 2009, 9, 30.

[286] X. L. Li, G. Y. Zhang, X. D. Bai, X. M. Sun, X. R. Wang, E. Wang, H. J. Dai, Nat Nanotechnol 2008, 3, 538.

[287] G. Eda, G. Fanchini, M. Chhowalla, Nat Nanotechnol 2008, 3, 270.

[288] G. Eda, Y. Y. Lin, S. Miller, C. W. Chen, W. F. Su, M. Chhowalla, Appl Phys Lett 2008, 92, 233305.

[289] J. Z. Wang, K. K. Manga, Q. L. Bao, K. P. Loh, J Am Chem Soc 2011, 133, 8888.

[290] H. X. Chang, J. S. Cheng, X. Q. Liu, J. F. Gao, M. J. Li, J. H. Li, X. M. Tao, F. Ding, Z. J. Zheng, Chem-Eur J 2011, 17, 8896.

[291] S. De, P. J. King, M. Lotya, A. O'Neill, E. M. Doherty, Y. Hernandez, G. S. Duesberg, J. N. Coleman, Small 2010, 6, 458.

[292] M. Inagaki, Y. A. Kim, M. Endo, J Mater Chem 2011, 21, 3280.

[293] M. V. Savoskin, V. N. Mochalin, A. P. Yaroshenko, N. I. Lazareva, T. E. Konstantinova, I. V. Barsukov, L. G. Prokofiev, Carbon 2007, 45, 2797.

[294] J. H. Lee, D. W. Shin, V. G. Makotchenko, A. S. Nazarov, V. E. Fedorov, J. H. Yoo, S. M. Yu, J. Y. Choi, J. M. Kim, J. B. Yoo, Small 2010, 6, 58.

[295] J. Kwon, S. H. Lee, K. H. Park, D. H. Seo, J. Lee, B. S. Kong, K. Kang, S. Jeon, Small 2011, 7, 864.

[296] L. Gong, I. A. Kinloch, R. J. Young, I. Riaz, R. Jalil, K. S. Novoselov, Adv Mater 2010, 22, 2694.

[297] R. J. Young, L. Gong, I. A. Kinloch, I. Riaz, R. Jalil, K. S. Novoselov, ACS Nano 2011, 5, 3079.

[298] H. Y. Sun, Z. Xu, C. Gao, Adv Mater 2013, 25, 2554.

[299] J. Lin, H. W. Gao, J Mater Chem 2009, 19, 3598.

[300] D. D. Shao, Z. Q. Jiang, X. K. Wang, Plasma Process Polym 2010, 7, 552.

[301] L. M. Malard, M. A. Pimenta, G. Dresselhaus, M. S. Dresselhaus, Phys Rep 2009, 473, 51.

[302] S. M. Notley, Langmuir 2012, 28, 14110.

[303] J. Geng, B. S. Kong, S. B. Yang, H. T. Jung, Chem Commun 2010, 46, 5091.

[304] A. A. Green, M. C. Hersam, Nano Lett 2009, 9, 4031.

[305] P. Nemes-Incze, Z. Osvath, K. Kamaras, L. P. Biro, Carbon 2008, 46, 1435.

[306] A. N. Sidorov, M. M. Yazdanpanah, R. Jalilian, P. J. Ouseph, R. W. Cohn, G. U. Sumanasekera, Nanotechnology 2007, 18.

[307] M. H. Gass, U. Bangert, A. L. Bleloch, P. Wang, R. R. Nair, A. K. Geim, Nat Nanotechnol 2008, 3, 676.

[308] L. J. Cote, F. Kim, J. X. Huang, J Am Chem Soc 2009, 131, 1043.

[309] I. N. Kholmanov, C. W. Magnuson, A. E. Aliev, H. Li, B. Zhang, J. W. Suk, L. L. Zhang, E. Peng, S. H. Mousavi, A. B. Khanikaev, R. Piner, G. Shvets, R. S. Ruoff, Nano Lett 2012, 12, 5679.

[310] Iskandar N. Kholmanov, Sergio H. Domingues, Harry Chou, Xiaohan Wang, Cheng Tan, Jin-Young Kim, Huifeng Li, Richard Piner, Aldo J. G. Zarbin, R. S. Ruof, ACS Nano 2012, 7, 1811.

[311] L. Y. Niu, M. J. Li, X. M. Tao, Z. Xie, X. C. Zhou, A. P. A. Raju, R. J. Young, Z. J. Zheng, Nanoscale 2013, 5, 7202.

[312] Y. Liu, Q. H. Chang, L. Huang, J Mater Chem C 2013, 1, 2970.

[313] M. L. Jiang, J. M. Wu, F. Lan, Q. Tao, D. Gao, G. Y. Li, J Mater Chem A 2015, 3, 963.

[314] H. J. Snaith, A. Abate, J. M. Ball, G. E. Eperon, T. Leijtens, N. K. Noel, S. D. Stranks, J. T. W. Wang, K. Wojciechowski, W. Zhang, J Phys Chem Lett 2014, 5, 1511.

[315] Q. H. Wang, K. K. Zadeh, A. Kis, J. N. Coleman, M. S. Strano, Nat. Nanotechnol. 2012, 7, 699.

[316] Q. Y. He, Z. Y. Zeng, Z. Y. Yin, H. Li, S. X. Wu, X. Huang, H. Zhang, Small 2012, 8, 2994.

[317] H. Li, Z. Y. Yin, Q. Y. He, H. Li, X. Huang, G. Lu, D. W. H. Fam, A. I. Y. Tok, Q. Zhang, H. Zhang, Small 2012, 8, 63.

[318] W. Choi, M. Y. Cho, A. Konar, J. H. Lee, G. B. Cha, S. C. Hong, S. Kim, J. Kim, D. Jena, J. Joo, S. Kim, Adv Mater 2012, 24, 5832.

[319] J. Z. Wang, L. Lu, M. Lotya, J. N. Coleman, S. L. Chou, H. K. Liu, A. I. Minett, J. Chen, Adv Energy Mater 2013, 3, 798.

[320] L. J. Cao, S. B. Yang, W. Gao, Z. Liu, Y. J. Gong, L. L. Ma, G. Shi, S. D. Lei, Y. H. Zhang, S. T. Zhang, R. Vajtai, P. M. Ajayan, Small 2013, 9, 2905.

[321] M. Shanmugam, T. Bansal, C. A. Durcan, B. Yu, Appl Phys Lett 2012, 100, 153901.

[322] H. Li, G. Lu, Y. L. Wang, Z. Y. Yin, C. X. Cong, Q. Y. He, L. Wang , F. Ding, T. Yu, H. Zhang, Small 2013, 9, 1974.

[323] J. Xiao, D. W. Choi, L. Cosimbescu, P. Koech, J. Liu, J. P. Lemmon, Chem Mater 2010, 22, 4522.

[324] W. Liu, J. H. Kang, D. Sarkar, Y. Khatami, D. Jena, K. Banerjee, Nano Lett 2013, 13, 1983.

[325] S. Tongay, J. Zhou, C. Ataca, K. Lo, T. S. Matthews, J. B. Li, J. C. Grossman, J. Q. Wu, Nano Lett 2012, 12, 5576.

[326] H. S. S. R. Matte, A. Gomathi, A. K. Manna, D. J. Late, R. Datta, S. K. Pati, C. N. R. Rao, Angew Chem Int Edit 2010, 49, 4059.

[327] K. Xu, Z. X. Wang, X. L. Du, M. Safdar, C. Jiang, J. He, Nanotechnology 2013, 24, 465705.

[328] J. S. Ross, S. F. Wu, H. Y. Yu, N. J. Ghimire, A. M. Jones, G. Aivazian, J. Q. Yan, D. G. Mandrus, D. Xiao, W. Yao, X. D. Xu, Nat Commun 2013, 4, 1474.

[329] D. Voiry, H. Yamaguchi, J. W. Li, R. Silva, D. C. B. Alves, T. Fujita, M. W. Chen, T. Asefa, V. B. Shenoy, G. Eda, M. Chhowalla, Nat Mater 2013, 12, 850.

[330] X. Huang, Z. Y. Zeng, S. Y. Bao, M. F. Wang, X. Y. Qi, Z. X. Fan, H. Zhang, Nat Commun 2013, 4, 1444.

[331] X. C. Dong, Y. M. Shi, W. Huang, P. Chen, L. J. Li, Adv Mater 2010, 22, 1649.

[332] Z. Y. Yin, Q. Y. He, X. Huang, J. Zhang, S. X. Wu, P. Chen, G. Lu, P. Chen, Q. C. Zhang, Q. Y. Yan, H. Zhang, Nanoscale 2012, 4, 293.

[333] R. Stine, J. T. Robinson, P. E. Sheehan, C. R. Tamanaha, Adv Mater 2010, 22, 5297.

[334] S. Mao, G. H. Lu, K. H. Yu, Z. Bo, J. H. Chen, Adv Mater 2010, 22, 3521.

[335] J. T. Robinson, J. S. Burgess, C. E. Junkermeier, S. C. Badescu, T. L. Reinecke, F. K. Perkins, M. K. Zalalutdniov, J. W. Baldwin, J. C. Culbertson, P. E. Sheehan, E. S. Snow, Nano Lett 2010, 10, 3001.

[336] J. R. Lomeda, C. D. Doyle, D. V. Kosynkin, W. F. Hwang, J. M. Tour, J Am Chem Soc 2008, 130, 16201.

[337] E. Y. Choi, T. H. Han, J. H. Hong, J. E. Kim, S. H. Lee, H. W. Kim, S. O. Kim, J Mater Chem 2010, 20, 1907.

[338] J. Q. Liu, L. Tao, W. R. Yang, D. Li, C. Boyer, R. Wuhrer, F. Braet, T. P. Davis, Langmuir 2010, 26, 10068.

[339] H. F. Yang, F. H. Li, C. S. Shan, D. X. Han, Q. X. Zhang, L. Niu, A. Ivaska, J Mater Chem 2009, 19, 4632.

[340] J. Zhang, J. P. Lei, R. Pan, Y. D. Xue, H. X. Ju, Biosens Bioelectron 2010, 26, 371.

[341] S. Niyogi, E. Bekyarova, M. E. Itkis, H. Zhang, K. Shepperd, J. Hicks, M. Sprinkle, C. Berger, C. N. Lau, W. A. Deheer, E. H. Conrad, R. C. Haddon, Nano Lett 2010, 10, 4061.

[342] L. H. Hess, A. Lyuleeva, B. M. Blaschke, M. Sachsenhauser, M. Seifert, J. A. Garrido, F. Deubel, Acs Appl Mater Inter 2014, 6, 9705.

[343] A. Kathalingam, V. Senthilkumar, J. K. Rhee, J Mater Sci-Mater El 2014, 25, 1303.